FLOW OVER A ROUGH SURFACE

Thesis by

Harry Warren Townes

In Partial Fulfillment of the Requirements

For the Degree of

Doctor of Philosophy

California Institute of Technology

Pasadena, California

1965

(Submitted March 12, 1965)

ACKNOWLEDGEMENTS

The author wishes to express his utmost appreciation for the advice and encouragement of Professor R. H. Sabersky, under whose guidance this work was carried out. In addition this opportunity is taken to gratefully acknowledge the support of the National Science Foundation under whose auspices this investigation was made. Many thanks are also due to Mr. T. C. Reihman, to Mr. E. F. Daly, to Mr. R. J. Williams, and to Mr. C. T. Eastvedt for their assistance in the experimental work.

ABSTRACT

An experimental investigation was conducted on the flow over a rough surface. The roughness consisted of sets of square cavities ranging in size from 1/8 to 1 in. The flow over this series of roughnesses was observed for a range of ϵ^* values from 11 to 260. The quantity ϵ^* may be regarded as a Reynolds number for the roughness and it is the essential parameter governing the flow over the roughness elements. It is defined as $\epsilon^* = \epsilon u_\tau / \nu$ where ϵ is the cavity depth, u_τ is the shear velocity, and ν the kinematic viscosity of the fluid. The desired approaching flow was obtained in an open surface water channel at free stream velocities of from 0.1 to 0.75 ft/sec. The velocity profile showed the characteristics of a turbulent boundary layer. The velocity measurements necessary to determine the profile were obtained by means of a hot film anemometer.

Visualization of the flow in the cavities lead to the classification of five characteristic flow types or modes. The observations could be described consistently in terms of these modes and as a function of ϵ^*. At values of ϵ^* below 100 different mode forms appeared periodically and large disturbances of the fluid within the cavity were noted. This type of flow had not been observed previously. At values of ϵ^* beyond about 200 a rather stable vortex formed in the cavities, as had been reported by previous experimenters. Some possible effects of the flow behavior on heat transfer are discussed.

Photographic materials on pp. 106-150 are essential and will not clearly reproduce on Xerox copies. Photographic copies should be ordered.

TABLE OF CONTENTS

LIST OF TABLES

Table | Page

LIST OF FIGURES

I. INTRODUCTION

There has been for some time a considerable amount of interest in the influence of surface roughness on heat transfer. The interest arises principally from the fact that the introduction of intentionally roughened surfaces has been shown to improve the heat transfer, usually, however, with a correspondingly larger increase in frictional losses. In a recent investigation concerned with the improvement of heat transfer by means of wall roughness by Dipprey [9, 10],[1] empirical relationships have been proposed which indicate that under certain circumstances the heat transfer effectiveness of a rough surface may exceed that of a smooth surface. The effectiveness in this case is defined as the ratio of the heat transfer to the friction coefficient. The results obtained are of interest for the design of heat exchange surfaces, especially when size, weight and pumping power must be kept to a minimum. Moreover, the results present a further challenge to the understanding of the flow and the heat transfer characteristics of rough surfaces. As a first step in gaining a better understanding of the heat transfer mechanism in the presence of a rough surface it appeared necessary to examine in more detail the flow in the immediate vicinity of a wall roughness element.

---

[1] Numbers in brackets refer to references.

In previously conducted research concerned with the heat transfer characteristics of rough surfaces several hypotheses have been advanced as to the nature of the flow about a wall roughness element. Dipprey [9], for example, proposed a so-called "cavity vortex hypothesis." In this model which is limited to the "fully rough"[2] flow regime, the flow in the space between roughness elements is imagined to be occupied by a vortex with its axis parallel to the wall and perpendicular to the flow direction. The major resistance to heat transfer is believed to occur in the transfer from the wall to the fluid in the cavity. The exchange of fluid between the cavity and the outside flow is assumed to take place freely. Chapman [2] proposed a similar model in which the cavity was considered as a closed region, with no exchange of fluid with the external flow. His model was based on a separated laminar boundary layer and on the separation shear layer remaining stable across the cavity span. A third and different model has been proposed by Owen and Thompson [37]. They considered the space between roughness elements to be swept by longitudinal vortex elements. In reviewing the presently available work on heat transfer from rough surfaces, there appeared to be a definite need for more information about the flow near a rough surface. The emphasis of the present investigation was therefore placed on gaining an understanding

---

[2] See Section II for definition.

of the character of flow near a roughness element in order to provide a basis for future models. As the flow was likely to be very complicated, direct visualization of the pattern appeared to offer the most promising approach. This method was hoped to provide basic, even if less quantitative, information about the processes taking place.

II. REVIEW OF LITERATURE

Heat transfer surfaces as they are used in engineering applications are often rough. The roughness may be caused by several factors in addition to the intentional roughening of surfaces used to improve heat transfer rates. Although a rough surface improves heat transfer, the friction loss is usually increased to a greater extent, thus reducing the effectiveness.

Many investigations on the heat transfer and friction drop have been conducted for roughnesses of various kinds. As a background to the present investigation, a review of some of the pertinent references dealing with the behavior of various rough surfaces is presented.

Historically the first comprehensive investigations of a rough surface was the study of frictional behavior by Nikuradse [35], published in 1933. Nikuradse constructed a rough surface by the attachment of sand grains to the inner wall of a pipe. The sand grains were nearly uniform in size and thus gave a close-packed, three dimensional rough surface. Water was the working medium. This experimental method provided the data with which Nikuradse developed relationships for the frictional behavior of rough pipes as a function of Re and ϵ^*. Of special interest to the present investigation is the parameter ϵ^*, which is defined as

$$\epsilon^* \equiv \frac{\epsilon u_\tau}{\nu} , \qquad (1)$$

where ϵ is sand grain size, $u_\tau = \sqrt{\tau_o / \rho}$ is the shear velocity and ν is the kinematic viscosity. Nikuradse found that the parameter ϵ^* governed the friction coefficient behavior. The quantity ϵ^* is a "wall parameter," formed from parameters associated with the wall region. The present investigation is also concerned with flow conditions in the vicinity of the wall and therefore one should expect ϵ^* to be one of the principal parameters.

Nikuradse observed three characteristic regions of behavior of the friction coefficient for the sand grain type roughnesses, and used ϵ^* in order to describe these regions quantitatively. For ϵ^* values ≤ 3.55 Nikuradse found that the friction coefficient of a rough surface was the same as that of a smooth surface. This region is termed the "hydraulically smooth" case. For values of ϵ^* between 3.55 and 67.5 the friction coefficient deviates from that of a smooth surface, passes through a minimum and then increases toward a constant value. The region of $3.55 \leq \epsilon^* \leq 67.5$ is termed the "roughness transition" region. For values of $\epsilon^* \geq 67.5$ the friction coefficient remains constant independent of the Reynolds number; this is termed the "fully rough" condition. These three regions are shown in Figures 1 and 2 which are plots at Nikuradse's data. In Nikuradse's work the parameter ϵ^* was based on the sand grain diameter ϵ. For different roughness types for which ϵ is an arbitrarily selected characteristic size the exact numerical value of ϵ^* at the boundaries of the above flow regions may well be different. The ϵ^* parameter may also be rewritten to indicate the relative size of the roughness elements compared to the laminar sublayer thickness. If y_{1s} is the laminar sublayer thickness of a turbulent boundary layer defined by

$$y_{1s} \equiv \frac{5\nu}{u_\tau} \tag{2}$$

then

$$\epsilon^* = \frac{5\epsilon}{y_{1s}} \; . \tag{3}$$

Frequent use of the parameter ϵ^* will be made in following sections when describing the behavior of the flow about roughness elements.

A rough tube experiment of a scale and geometry very different from the system of Nikuradse, was that of Folsom [12]. Folsom used an experimental arrangement consisting of an annulus with series of disks of various diameters and spacings. The effect of these disks was to create an annular flow passage with thin fins on the inner cylinder. In some instances the outer edge of the disks were close to the outer pipe wall. In addition to pressure drop measurements, Folsom also made some visual observations of the flow in the space between the annular fins. It is interesting to note the similarity between the observations of Folsom and Wieghardt [47]. Wieghardt has reported some visual observations of flow in a single rectangular cavity on a flat plate with flow perpendicular to the cavity axis. Despite the different geometries, Folsom and Wieghardt observe quite similar flow conditions, in which the "square" cavity is occupied by a single, fairly steady vortex. Wieghardt also reported some observations for ε/w values (ε = depth, w = width of cavity) other than 1. In the narrow cavities ($\varepsilon/w = 2:1$) of Wieghardt the space is occupied by two counter rotating vortices, the lower or deeper vortex being very weak. Wieghardt noted for the flow within a cavity that "a dependence on the thickness of the (turbulent) boundary layer (of the approaching flow) is hardly noticeable." The range of ε/δ (δ = thickness of turbulent boundary layer) explored by Wieghardt was from 10 to 1. Thus the total approaching turbulent boundary layer thickness was from one to one tenth the cavity depth. This would correspond to ε^* values ranging from approximately 1,000 to 10,000. In the present series of investigations the turbulent boundary layer thickness is such that ε^* values vary from 11 to 250. Although it was not observed by Wieghardt one may more likely expect to see an effect of the thickness of the boundary layer on the cavity flow for the present investigations. Of further interest was the observation by Folsom of a "pulsating flow" within the cavities causing a fluctuation in the pressure drop across the test section. This occurred when the spacing of the disks formed a ε/w value of approximately 0.3. Pulsations have also been noted by several other investigators for cavity flows in certain ranges of cavity depth to width.

Roshko [41] studied the wall pressure distribution in a rectangular cavity of fixed width and variable depth in a wind tunnel. The nominal tunnel speeds were 75 and 210 ft/sec. There is no large difference in the shape of the pressure distributions on the cavity walls, for the two speeds, thus indicating little if any influence of the approaching turbulent boundary layer thickness on the cavity flow type. Roshko also noted a fluctuation in pressure readings on the cavity walls in the range of ϵ/w from approximately 0.45 to 0.85. The lower ϵ/w value at which Roshko observed fluctuations in wall pressure is near that in which Folsom noted fluctuations. In addition Roshko observed fluctuations at ϵ/w values of 2 to 2.5. Roshko does not report any findings for values of $\epsilon/w > 2.5$. It is interesting, though perhaps only coincidental, that the fluctuating flow character was noted by both Folsom and Roshko in roughly the same range of ϵ/w values. Further investigations similar to those of Roshko were carried out by Mills [34].

Another aspect of the pulsating flow observed by Roshko has been presented by Maull and East [32]. Using an experimental arrangement essentially the same as that of Roshko, Maull and East made some flow visualization studies. Visualization of the flow was accomplished by noting the pattern formed by an oil film on the cavity bottom. Maull and East conclude that there occurs in cavities a three dimensional cellular type flow. They cite as evidence of this cellular structure the curved shape of the oil film formed by flow on the cavity bottom. Maull and East postulate that the unsteady pressures observed by Roshko and Mills were caused by the inability of the cavity spans to accommodate an integral number of the preferred three dimensional cell lengths. Thus the cavity fluctuated between two flow configurations. The span of the cavity used by Roshko was 32 in. and that used by Maull and East was 19 in. Maull and East note a collapse in the cellular flow for $0 \leq \epsilon/w \leq \approx 0.45$, $0.85 \leq \epsilon/w \leq 1.25$, $\epsilon/w > \approx 2.2$. This is in broad agreement with the regions in which Roshko and Mills noted relatively steady pressure distributions.

Charwat, et al. [3, 4] have conducted a series of experiments in two parts with supersonic and subsonic flow over single cavities. The first part was concerned with the pressure distribution and the second with heat transfer. Both the ratio of width to breadth of the cavity and the geometry of the recompression step were varied. Charwat concludes that the approaching thickness of a turbulent boundary layer has little effect on the cavity pressure distribution until δ/ϵ becomes > 1, where δ is the total thickness of the approaching turbulent boundary layer and ϵ is again the depth of the cavity. This may account for the report by Wieghardt mentioned earlier, to the effect that the approaching boundary layer did not influence the cavity flow pattern. In addition Charwat reports that small changes in the geometry of the downstream civity wall have little effect on the pressure distribution within the cavity. Charwat did not use cavities in the range of ε/w values which have the cellular and unsteady flow characteristics reported by Maull and East, by Roshko and by Folsom. Charwat does note that the cavity flow is unsteady and also that the exchange of fluid between the cavity and outside flow takes place quite freely. Of interest from the heat transfer studies of Charwat is the remark that "The ratio of heat transfer to an open cavity[3] to that of an equivalent attached boundary layer (on a flat plate) is primarily a function of the thickness of the oncoming (turbulent) boundary layer. If it is thin[4] the heat transfer ratio is reduced by a factor of approximately two; if it is thick, the heat transfer can even be increased." The drag of a notched wall is always, according to Charwat, an order of magnitude greater than that of a smooth wall.

Additional investigations have been made of the heat transfer characteristics of both a rough surface produced by sand grains, by knurling, by square threads, by rings, and by fin type roughnesses on the inner tube of an annular configuration. Fortescue and Hall [13] report

---

[3] Charwat defines an "open cavity" as one in which the outside flow does not reattach to the cavity bottom but separates and spans the cavity width.

[4] Less than one notch depth, $\varepsilon^* > 1,000$.

on a series of experiments carried out for the purpose of determining a heat transfer surface for nuclear reactor fuel elements. Several fin diameters and spacings were tested for air flowing in an annular space with fins on the inner tube. The heat transfer was from the inner finned tube to the air. Knudsen and Katz [24] conducted a similar series of experiments, but with water and oil as the working mediums. The results of the two investigations indicate that by the addition of fins to the inner tube an improvement in heat transfer rate as well as a reduction in pumping power for a given heat transfer rate can be achieved for the annual geometry in this particular application. The fin spacing, fluid, and Reynolds number all influence the heat transfer, friction pressure drop relationships.

Knudsen and Katz also made some visual studies of the flow between the annular fins. The observations for turbulent flow were similar to those of Folsom. Knudsen and Katz, however, made some observations for the case of laminar flow in the annulus. The laminar case is particularly interesting as it shows that the dye, used for visualization, does not enter the space between the fins, even though it is introduced very close to the fin tips. This indicates very poor exchange of fluid between the cavity and the outside flow which may be contrasted with the very good exchange of fluid noted by other investigators for turbulent flow across cavities and annular fins.

Sams [43] conducted a series of experiments in tubes in which the roughness was produced by square threads. The working medium was air. The tubes had a nominal inside diameter of 0.5 in., and were 24 in. long with roughness ratios, ϵ/D, of 0.016, 0.025, 0.037 and 0 (smooth). The tubes were heated electrically. Among Sams' conclusions is the statement that the roughness ratio ϵ/D is not sufficient to determine the frictional behavior of rough tubes. The friction coefficient of the tube with $\epsilon/D = 0.025$ was above that of the tube with ϵ/D in 0.037 in the fully rough range. Although Sams makes no comparison of the heat transfer efficiency of these tubes, Dipprey [9] using Sams' data, concludes the effectiveness (C_h/C_f) is below that of a smooth tube.

Nunner [36] performed a series of experiments in a smooth and in artificially roughened and naturally rough pipes. In these experiments air was the working medium and measurements made of the heat transfer and friction coefficient. In addition velocity and temperature profiles were determined. As artificial roughnesses Nunner used split rings inserted into a brass tube. Four such set of rings, one ring with a square cross section, and the other three of a semicircular shape, were used. The spacing between rings was varied as well as the ring shape. The outer surface of the brass tube was heated by condensing steam and the Reynolds number of the flow was varied from 500 to 8×10^4. Nunner found an increase in the heat transfer coefficients for rough tubes, and proposed a model of the flow to explain this increase. This flow model postulated that the increase in heat transfer was caused by increased turbulence in the core fluid. The wall layers were assumed to remain unaffected by the roughness elements.

Hastrup [16] produced an artificially rough inner surface on a tube by knurling the outer wall. Water was used as the working medium and the tube heated electrically. By varying the water temperature the influence of Prandtl number could be determined. Experiments similar to Hastrup's were carried out by Dipprey [9], using rough tubes formed by electroplating nickel over a mandrel covered with sand grains and then chemically removing the mandrel. Thus a three dimensional sand grain type roughness was produced. Again water was the working medium and the tubes were heated electrically. The experiments of Dipprey were extensive; heat transfer and friction coefficient measurements were made over a range of Reynolds numbers from approximately 10^4 to 10^6 and Prandtl numbers from 1.2 to 5.94 for three rough and a smooth tube. The rough tubes show the transition region which is characteristic of the sand grain roughened pipes used by Nikuradse.

In all cases the rough tubes used by Dipprey show an increase in the heat transfer coefficient over that of a smooth tube. It is also interesting to note that a maximum in the heat transfer coefficient occurs near the high end of the roughness transition region ($\epsilon^* \approx 70$).

Dipprey used as a measure of heat transfer effectiveness the ratio $2C_h/C_f$. Two of the rough tubes showed a higher heat transfer effectiveness than the smooth tube; however, this improved effectiveness was shown only at higher Prandtl numbers and in the transition region of the friction coefficient. The heat transfer measurements of Hastrup did not show this improvement in effectiveness. Combined, the results of Sams, Hastrup and Dipprey show that the fluid Prandtl number and both the roughness size and particularly the roughness geometry influence the heat transfer and friction coefficient relationships of a surface.

III. PRESENT PROBLEM

As can be seen from the foregoing review of literature, several investigators have been concerned with the flow conditions in tubes with various types fins and wall roughnesses and with the flow in cavities. Thus far no flow visualization studies have considered the possible effect of a wide variation of the thickness of the laminar sublayer of an approaching turbulent stream. Up to the present investigations have been for $\epsilon^* > 500$. In fact, both the variations in turbulent boundary layer thickness and the ratio of the laminar sublayer thickness of the approaching turbulent boundary layer to roughness height have been relatively small. Of the authors reporting the effect of the turbulent boundary layer thickness on cavity flow or cavity pressure distribution the general conclusion is that the boundary layer of the approaching flow has little if any effect, at least for the large ϵ^* regions investigated. These observations may be contrasted with the observed changes in the friction and heat transfer coefficients [9, 35] as some types of rough surfaces pass through the transition region of the friction coefficient. Although the friction and heat transfer coefficients are quantities averaged over many roughness elements, a change in such an average quantity may indicate a different flow pattern about individual roughness elements. These changes in behavior, however, occur when the laminar sublayer thickness of the turbulent boundary layer and the roughness size are comparable, i.e. at values of ϵ^* much below 500. Previous investigators have not observed changes in the flow pattern about roughness elements, possibly because the observations have not been made for low ratios of the roughness height to the laminar sublayer thickness. The focus of the present investigation is the flow process taking place in the neighborhood of a rough wall when the laminar sublayer thickness and wall roughness elements are of a comparable size. It is hoped that information concerning the flow in the vicinity of a wall roughness element will lead to a better understanding of the mechanism of heat and momentum transfer from rough surfaces.

IV. EXPERIMENTAL APPROACH

A. Flow Requirements

In the Section II several studies on the flow in wall cavities of various shapes were discussed. These studies involved the measurement of pressure distributions, heat transfer, and friction coefficients and in addition some direct visualization of the flow patterns. In the investigations of cavity flow the approaching turbulent boundary layers have been rarely as thick as the cavity depth, and have generally been less than the cavity depth. Thus the investigations made so far have been well into what is termed the "fully rough" flow condition for a rough surface, with ϵ^* values in excess of 500. For instance, if the total turbulent boundary layer thickness is the same as a roughness height, then the ϵ^*[5] value is about 1,000 as in the investigation of Wieghardt [47].

---

[5] It should be pointed out here, that in making these comparisons some liberty has been taken with the evaluation of ϵ^*. Nikuradse originally defined ϵ^* values for fully developed turbulent flow in rough tubes with the boundary layer developed over the full length of the rough tube surface. In this past discussion the ϵ^* value for cavities has been based on characteristics of the approaching turbulent boundary layer developed along a smooth wall. Consequently in single cavities a somewhat different ϵ^* value may result for the various regions of behavior of the friction coefficient. These present values of ϵ^* for cavities, nevertheless, serve to indicate the relative size of the laminar sublayer of the approaching turbulent boundary layer and the cavity.

The object of the present investigation was to observe the flow in the immediate vicinity of a wall roughness element for values as low as $\epsilon^* \approx 10$. The experiments also were to extend to sufficiently large values of ϵ^* so that comparisons with past investigations could be made. Observation of the flow at low ϵ^* values presents some difficulties because of the small physical size of the laminar sublayer thickness. For example in a smooth pipe operating at a Reynolds number of 5×10^4 the laminar sublayer thickness is about 0.001 in. at a mean velocity of 10 ft/sec. It was felt that visualization would be greatly facilitated if the roughness size could be made reasonably large, say 1/8 in. or larger. The desired thick laminar sublayers may be produced by operating at low mean velocities. The present investigation was carried out in an open surface water channel in which the flow over the bottom surface approximated that over a flat plate. The selection of a water channel or flume over a pipe was made on the basis of ease of operation and instrumentation. The open surface of the water channel facilitates installation of probes for velocity measurement and general operation. The boundary layers of both pipes and flat plates are very similar, especially close to the wall; i.e., at low values of Y^+, so that the results regarding the flow over the surface roughnesses should be applicable to both types of conduits.

A preliminary series of studies was made in an existing flume.[6] These studies, which included a velocity profile and some flow visualization, indicated that the boundary layer on the bottom of the flume did approximate that on a flat plate. The visualization studies in addition confirmed that roughness elements of at least 1/8 in. would be desirable so that existing photographic equipment and relatively simple visualization techniques could be used.

It was also necessary to estimate the free stream velocities required to produce the flow leading to the ε^* values desired for the minimum roughness size of 1/8 in. This estimate was obtained from the equations for the friction coefficient, C_f. Several empirical relationships are available which give the local friction coefficients of flat plates as functions of the Reynolds number based on the length from the leading edge. Two such equations which well represent the experimental data are the following:

$$C_f = \frac{0.370}{(\log_{10} Re_x)^{2.564}} , \tag{4}$$

which is due to Schultz-Grunow [11], and

$$C_f = \frac{0.0592}{(Re_x)^{1/5}} , \tag{5}$$

---

[6] The 33 1/2 in. flume located in Keck Laboratory, CIT.

which was proposed by Schlichting [44]. The friction coefficient, C_f, and the friction velocity, u_τ are defined by the equation

$$C_f = \frac{\tau_w}{1/2\, \rho\, U_\infty^2} = \frac{2u_\tau^2}{U_\infty^2} \tag{6}$$

so that

$$u_\tau = \sqrt{C_f/2}\, U_\infty \quad . \tag{7}$$

The dimensionless parameter ϵ^* was defined previously as

$$\epsilon^* = \frac{\epsilon\, u_\tau}{\nu} \quad , \tag{8}$$

and therefore,

$$\epsilon^* = \frac{\epsilon\sqrt{C_f/2}\, U_\infty}{\nu} \quad . \tag{9}$$

The values of C_f given by the two equations do not differ by more than 5%. Using the simpler one of Schlichting, the expression for ϵ^* becomes

$$\epsilon^* = \frac{\epsilon\, U_\infty\, 0.171}{\nu(Re_x)^{0.1}} \quad , \tag{10}$$

which may be written as

$$\epsilon^* = 0.171\, \epsilon \left(\frac{U_\infty}{\nu}\right)^{0.9} (x)^{-0.1} \quad . \tag{11}$$

The length x of the last expression is the distance from the leading edge of the flat plate, or in this instance the flume length. For the present investigation this was limited to about 48 ft by the length of the channel. The two factors available to produce different ϵ^* values are then the cavity depth ϵ and the ratio U_∞/ν. Increasing the viscosity of the working fluid at first appears to offer a good means for decreasing the value of ϵ^*. However, an increased viscosity also delays transition from laminar to turbulent flow on a flat plate. In order to keep the transition region within the confines of the flume the ratio U_∞/ν cannot be decreased below a fixed value. For this reason increasing the viscosity of the working medium by using, for example, a solution of water and glycerine instead of water alone does not lead to substantially decreased ϵ^* values, and consequently water was used as the working medium. Using water as the working medium, a plate length of 48 ft and a minimum ϵ of 1/8 in. one can compute the relationship between ϵ^* and U_∞, by using the last equation. In the case of the flume used this calculation leads to values of velocities in the range of 0.1 to 0.75 ft/sec. Using these free stream velocities and roughness sizes from 1/8 to 1 in., ϵ^* values from approximately 11 to 250 were achieved experimentally. These experimental ϵ^* values are based upon empirically determined local shear stress values a short distance ahead of the roughness elements.

B. Roughness Geometry

There are a large number of geometries which could have been used for the roughness elements. For this investigation a simple two dimensional square cavity was selected. The flow in this type of cavity has been studied for large ϵ^* values and this made possible comparisons between the flow at ϵ^* values in the fully rough region with those of previous investigators. The axis of the square cavities was placed perpendicular to the main stream flow direction. The width of the dividing wall between cavities is equal to one half of the cavity depth. A sketch of the cavity geometry is shown in Figure 3. Four such series of geometrically similar cavities were constructed of plexiglas having depths of 0.125, 0.250, 0.500 and 1.00 in. The minimum size was limited by a desire to keep the roughness element and flow patterns visible to the unaided eye and to facilitate visualization and photographic recording. The establishment of this minimum size also simplifies the illumination problem as, for a given negative size, the required intensity of lighting increases as the size of the element is reduced. Intense lighting is undesirable as it introduces a sufficient amount of heating to cause extraneous convection currents at the low velocities used.

While it is true that square cavities do not necessarily represent an important type of roughness encountered in practice, they do provide a simple and scalable model which still may be expected to preserve many of the characteristics of a typical roughness.

C. Cavity Installation

The cavities were installed in the channel with the upper surface of the dividing walls in the same plane as the preceding smooth channel bottom. A drawing of a cross section through the channel center line at the cavity section is shown in Figure 4. In order to install the cavities in this manner a false bottom of plexiglas was inserted for a length of 3 ft. upstream of the cavity section. Both the cavity section and the plexiglas false bottom were mounted on adjustable screw jacks to permit leveling with the channel bottom. Adjustments were also necessary due to the expansion of plexiglas in water.

The axial length of the cavities was 18 in. in all cases. The axis of each cavity was aligned perpendicular to the channel walls within ± 1/32 in. in their 18 in. length. Several holes for admitting dye were located on the channel centerline in different cavities and various positions within these cavities. Axial motion of dye within the cavities were slight and showed no preferential direction, thus indicating satisfactory alignment. The data of this report were taken from observations of the fourth cavity downstream of the series. The number of cavities in the series varied from eight in the case of the 1 in. cavities to as many as fifteen for the 1/8 in. cavities.

D. Channel Description

As has been noted in a past section an open surface water channel was selected as the means for producing the thick laminar sublayer required for this investigation. Figures 5, 6, and 7 show photographs and a sketch of the complete channel, the entrance section and the recirculating circuit. The channel cross section is 33.5 in. wide and 12 in. deep. The overall length of the channel is 60 ft., with the test section for the present series of experiments located at 48 ft. from the entrance section. A series of screens was placed in both the entrance and exit sections. The screens served to reduce the free stream turbulence and to eliminate surface waves. In operation the water surface was "glassy smooth" up to a free stream velocity of 0.5 ft/sec. Only at 0.75 ft/sec. very slight surface waves, caused by the entrance section, were noted. Measurements of the free stream turbulence showed a maximum level of about 0.8% for all velocities. The free stream velocity in the channel was controlled by varying the speed of the return pump and adjusting a throttle valve in the return line.

As can be seen from the photograph and sketch of the channel the pump and its motor were solidly mounted to the floor and were not in rigid contact with the channel structure. The only mechanical contact was through a "rubber boot" on the exit section. This boot was necessary to allow changes in the slope of the channel. The boot was flexible enough and the floor mounting sufficiently rigid so that no surface waves or vibrations were transmitted to the channel by the pumping system.

The series of six entrance screens in the channel were the only devices installed to reduce the turbulence level. No tripping wires or entrance roughnesses were used to promote boundary layer transition. For the purposes of this investigation it was not felt necessary to reduce the secondary flow which is present in a channel of rectangular cross section. The secondary flow was small in the neighborhood of the region in which measurements were made and the flow profile did exhibit the main characteristics of a turbulent boundary layer flow, as was desired. The uniformity of the velocity across the center of the channel was established by several velocity profiles which are presented in Section VI, Part A.

E. Working Medium

The working fluid was water taken from the city water supply. Small amounts of chlorine were added to prevent the growth of algae. The water was continuously filtered before and during tests by a filtering system using diatomaceous earth as the filtering agent in order to remove particles which would interfere with flow visualization and observation. The water was continuously exposed to air and since no deaireation system was used the water may be considered as nearly saturated with air. The total volume capacity of the channel was approximately 1,300 gallons. The large heat capacity of this amount of water kept temperature variations to less than $\pm 2^{\circ}F$ over test periods as long as 12 hours.

V. INSTRUMENTATION AND METHODS OF MEASUREMENT

A. Velocity Measurements

The present series of experiments require very low stream velocities in order to produce the required laminar sublayer thicknesses. The measurement of these low velocities introduces several problems. The average free stream velocities of 0.75, 0.5 and 0.25 ft/sec. were determined by means of a propeller probe. At 0.125 ft/sec. the average free stream velocity was obtained by measuring the time for a dye spot to move a known distance. However, neither the propeller probe nor the dye were suitable for measuring the average velocity within the boundary layer itself and consequently several other methods were considered. Of the three methods, involving a hot film anemometer, a pitot tube, and tracer particles, the method based on the use of a hot film anemometer was found to be the most suitable.

Constant temperature hot wire anemometers have for some time been used for measurements of mean velocities and turbulent fluctuations in air. Although several investigators [28, 42] have reported successful operation of hot film or hot wire systems in water, this application of anemometry is relatively new. Several factors combine to make the operation of hot films in water much more difficult than in air. The temperature difference between the film and the ambient fluid, or overheat, is a major factor in determining the requirements placed upon the controlling anemometer circuitry. In water the overheat is limited to approximately 20°F due to the formation of air bubbles, if the water is nearly saturated with air as it was in the present investigation. Low wire overheats result in reduced sensitivity and increases in error due to resistance variations of the wire or film. Despite these difficulties, a hot film anemometer has several important characteristics which make it attractive for the present application. Of major importance to this investigation was that suitable probes of small size could be obtained. Hot wires of 0.0001 in. diameter are common and hot films of 0.001 in. diameter are commercially available.[7] This small probe size allows velocity measurements to be made within 0.01 to 0.001 in. of the wall without causing major disturbances to the flow. The laminar sublayer thickness at 0.75 ft/sec. free stream velocity in the present investigation was about 0.020 in., thus a small probe size is required in order to make velocity measurements within this laminar sublayer.

Consultation with the electronics company of Shapiro & Edwards concerning the amplifier system for a constant temperature hot film

---

[7] From Thermo-Systems, Inc., 2418 E. Hennepin Avenue, Minneapolis, Minnesota.

anemometer for use in water resulted in the construction of such a unit by the above firm. The amplifier produced was a modification of Shapiro & Edwards commercial unit model 60B. A circuit diagram of the anemometer which has since become commercially available is shown in Figure 8. This system has been found to operate very satisfactorily. Measurements have been made of mean velocities from 1.00 to 0.027 ft/sec. and at distances from the wall as small as 0.005 in.

B. Hot Film Probe

A very important part of the anemometer system is the hot film or wire probe itself. When it was decided to use an anemometer system initial attempts were made to construct a probe from 0.0002 in. diameter platinum wire, the supporting legs of which were lacquer coated to prevent electrolysis. These probes, however, suffered a high breakage rate due to the small wire size. Nevertheless, several of these probes were operated with some success. Use of very much larger wire is not convenient because the current capacity of the hot wire anemometer was not sufficient to allow a significant increase in wire diameter. At about the time of this experimentation some quartz coated platinum hot film probes became available commercially, in the appropriate size range (0.001, 0.002 and 0.006 in. diameter). A picture of two typical probes is shown in Figures 9 and 10. A cross section through the active portion is sketched in Figure 11. The outer quartz coating serves to protect the platinum film from chemical attack, and, in addition, insulates the probe electrically. All the probes were of similar construction. Tests of the commercial probes showed that they were sufficiently stable for operation in water, and in addition had the advantage of being relatively rugged mechanically. It was even possible, using care, to brush solid particles and air bubbles from the hot film probes without causing damage, something which had been impossible with a 0.0002 in. diameter wire. All the velocity measurements reported here were made with the commercial probes.

C. Linearizing Circuit

When operating the constant temperature hot film anemometer for making velocity measurements, the output voltage from the anemometer circuit was proportional to the current necessary to maintain the film at constant temperature. This current and consequently the voltage is not linearly related to the velocity past the film. Assuming only the velocity of the liquid to vary, the relationship is well approximated by King's Law [1, 7, 17, 18, 19, 22, 27]

$$Nu = A + B\ Re^{0.5} \tag{12}$$

where Nu is the Nussult number, Re is the Reynolds of the wire, and A and B are constants involving hot film and fluid parameters.

It is convenient for averaging and calibration purposes to have an electrical output which is linearly proportional to the velocity past the film. In the present application, for instance, mean velocity profiles were desired in a turbulent boundary layer at low velocities. The peak velocity fluctuations near the wall are often large, 20-40% [26, 40, 42] and, due to the low velocities, of long time duration, 2-10 seconds. This combination of large fluctuations and long time duration makes a linear output most desirable in order to be able to conveniently determine mean values of the velocity by electrical averaging methods.

As can be seen by inspection of the foregoing equation, a true mean velocity cannot be obtained by simply averaging the voltage output of the hot film anemometer under these velocity conditions. Consequently an analog circuit was constructed to invert Equation (12). This results in a voltage output, from the "linearizing circuit," which is directly proportional to the velocity past the film, under the condition that Equation (12) is valid. In addition an integration circuit was included in order to average velocities over long time periods. In the present experiments integration periods as long as 5 minutes were used.

A test of the linearizing circuit using D.C. voltages showed that it performed the desired analog functions within an accuracy of ± 3% at the 90% confidence level, from 2 to 100% of the voltage corresponding to the maximum velocity. A diagram of the general circuit elements is shown in Figure 12 together with a listing of the major components, Table 1. A more complete discussion of the overall accuracy of the velocity measurements made with the hot film anemometer and its linearizing circuit may be found in Section VI, Part A.

D. Shear Velocity Determination

In order to form the dimensionless parameter ε^* and to plot the boundary layer profile in the "universal" form of Y^+ vs U^+, the shear velocity u_τ must be determined from the wall shear stress τ_w.

The wall shear stress may be obtained in several ways. In closed conduits it may be determined directly from the measurement of the static head loss. The corresponding measurement for an open channel would involve a measurement of the slope. As the boundary layer is steadily growing this would, however, only lead to an average value of the friction coefficient over the channel length, and in the present experiment this average would include in some instances an appreciable length of laminar boundary layer. The determination of the local friction coefficient would require local measurements of the slope of the channel bottom as well as of the water surface at a given section making an accurate evaluation very questionable. Therefore, when dealing with a channel at low velocities, other methods of determining the local friction coefficient are preferred. One may for example infer the shear stress from a plot of the turbulent core profiles for various values of C_f, or compute it from the relationship given by Clauser [5]

$$\sqrt{2/C_f} = 5.6 \log Re_{\delta *} + 4.3 \qquad (13)$$

after determining the displacement thickness, δ^* empirically.

In the present investigation, however, the wall layer was of sufficient thickness compared to the diameter of the hot film probe such that the wall shear stress could be determined from the slope of the measured velocity profile in the laminar sublayer near the wall. It was usually possible to make as many as ten to twenty velocity measurements in this region which allowed a rather accurate determination of the velocity gradient. Assuming that the velocity gradient in the laminar sublayer is the same as that at the wall, the wall shear stress is then

$$\tau_w = \mu \left.\frac{du}{dy}\right|_{Y^+<5} \tag{14}$$

and the shear velocity

$$u_\tau = \sqrt{\tau_w/\rho} = \left[\nu \left.\frac{du}{dy}\right|_{Y^+<5}\right]^{1/2} . \tag{15}$$

This measured value of the shear velocity is compared with the value obtained from the empirical relationship of Schlichting in Section VI, Part A.

In addition the displacement thickness δ^* was determined from the velocity profiles and the friction coefficient computed from Equation (13) as given by Clauser. The values as computed from Equation (13) and from the laminar sublayer velocity profile agree quite closely and are probably the more reliable, as the equation of Schlichting is based on data for a flat plate and a turbulent boundary layer which starts essentially at the leading edge of the plate.

E. Traversing Mechanism

In order to make a velocity profile determination it is necessary to have a method of accurately varying the distance between the probe centerline and the channel bottom. For this purpose the traversing mechanism shown in Figure 13 was built. General construction consists of two parallel vertical cylindrical rods on which a probe holder rides. Ball bushings, that is, a linear motion ball bearing, were used as bearings for the probe holder. Adjusting screws for alignment of the vertical rods and for elimination of play in the ball bushings made for a very smoothly moving probe holder. A micrometer screw feed allowed movements of the probe centerline as small as 0.0001 in.

To locate the probe relative to the channel bottom, the initial location of the probe centerline was established by means of a locating rod, shown attached to the probe in Figure 14. The distance Y_1 of Figure 14 was determined by measurement on an optical comparator to an accuracy of ± 0.0005 in. The probe assembly was then mounted in the probe holder with the locating rod in contact with the channel bottom. The screw micrometer scale reading was next set to the value Y_1, previously determined, and the probe locked in place on the probe holder. The locating rod was then removed. In this manner the wall-probe distance could be determined within a maximum absolute error of ± 0.0015 inches for the first 1.0 in. from the wall.

F. Visualization Techniques

Several visualization techniques were tested before the selection of dye as the most suitable. A comprehensive discussion of several forms of flow visualization methods is presented by Clutter et al., [6]. The generally desired properties of a flow visualization medium are:

1. That it be highly visible;
2. That it can be easily introduced into the flow field without causing large disturbances;
3. That it follows the flow closely and does not influence the flow path.

Two methods considered and tested before the selection of dye as the most suitable were those involving hydrogen bubbles and aluminum flakes.

The hydrogen bubble technique, suitable for water, utilizes as flow tracers small bubbles produced by electrolysis at the surface of a fine wire. If the wire is of small diameter, 0.001 in. for example, the size and consequently the rise rate of the bubbles produced is usually also small. Difficulty in the present investigation arose from the very low velocities which occur in the cavities, typically down to 10% of the velocity in the outside flow which itself may be as low as 0.1 ft/sec. At low velocities the gas sheath formed by electrolysis was not torn from the wire by velocity induced shear stresses, but instead grew until buoyant forces released the bubbles. These bubbles were then relatively large despite the small wire sizes. They rose at rates comparable with the velocities in the cavity and so rendered the hydrogen bubble method useless for a cavity flow study.

As an alternative approach aluminum particles were tried as tracers. Aluminum flakes of the size and type used as paint pigment were found to be very suitable for flow visualization. The flat flake configuration gave a high drag coefficient and despite the large density difference, settling rates were low. The most suitable particles could be selected by first settling out the heavier ones in a suspension in a jar. The main difficulty was caused by the flat shape of the flakes because of which they were visible only in certain orientations. The flakes could not be detected when turned edgewise and it became difficult to follow them for extended periods of time. Dye injection--actually one of the more common visualization methods--was then examined and found to be most suitable for the present conditions.

The dye selected was a very intense jet black aniline type. Because of the high intensity, relatively weak concentrations, with essentially the same density as water, gave good contrast. The densities could be matched so closely that the dye could be assumed to follow the flow pattern in the cavity at even the lowest velocities. A gravity feed system provided with a manifold and a set of throttling valves was used to control the rate of dye flow. Thus in practice the dye emerging from the small surface hole appeared to creep parallel to the surface for a short distance. By keeping the amount and velocity of dye injection small, disturbances to the flow were minimized. Typical photographs characteristic of those obtainable with aluminum flakes and hydrogen bubbles are shown in Figures 15 and 16.

G. Photographic Arrangement

In order to complete the visual study of the flow in the cavities, it was found to be desirable to take both still and motion pictures. The center of the channel was considered to be the best position for such photographs, since disturbances from the wall and induced secondary flow should be at a minimum at this location. This has been confirmed by the velocity profiles presented in Section VI, Part A. The principal photographic problem involved the small size (1/8 × 1/8 in.) of the smallest cavities and the minimum distance between the camera lens and the cavity centerline. The physical size of the channel does not permit location of the camera lens any closer than about 16 in. from the channel centerline, when viewing through a glass side wall in the channel. In order to obtain a satisfactory negative image size, a lens of 12 in. focal length was selected, giving negatives 1.5 times full size for the 1/8 × 1/8 in. cavities. Still photographs were obtained with a 35 mm camera and the above lens. Since velocities were relatively low, high speed motion pictures were not necessary and a standard 16 mm motion picture camera with framing rates of from 10 to 64 frames/sec. was used to record cavity flow with the same lens system. The motion pictures were later reviewed on a frame by frame basis to arrive at the data presented in the results. The observation time of the motion pictures was from 2-5 minutes, depending upon the framing rate. From fifty to one hundred and twenty still photographs were usually taken. Since the change in flow is quite rapid at the higher ϵ^* values, it is not possible to obtain a still photograph of any one given flow type at will. Therefore still photographs were taken at random times but in large numbers in order to record all variations in the flow. A comparison of still and motion pictures showed that in order to insure several still photographs of each flow type from 50 to 100 pictures were needed.

VI. EXPERIMENTAL RESULTS

A. Velocity Measurements

1. Shear Velocity

The mean velocity profiles presented in a subsequent section are plotted in the "universal" form of U^+ vs. Y^+, where

$$U^+ = \frac{u}{u_\tau} \tag{16}$$

and

$$Y^+ = \frac{y\, u_\tau}{\nu} \; . \tag{17}$$

Necessary for the formation of the U^+ and Y^+ quantities is the shear velocity u_τ which is formed from the wall shear stress τ_w and the fluid density ρ. As was mentioned earlier the wall shear stress, in the present investigation was determined directly from the slope of the velocity profile in the laminar sublayer. A straight line was fitted by the method of least squares to those points which were in the region $Y^+ \leq 5$. For a comparison the friction coefficient was also computed from the empirically determined displacement thickness δ^* in the relationship given by Clauser, Equation (13), and by using the equation given by Schlichting, Equation (5). Tables 2 and 3 give values of the local friction coefficient C_f, and the shear velocity u_τ respectively as found by the three methods. As can be seen the values of u_τ as determined from the slope of the velocity profile for $Y^+ \leq 5$ and the displacement thickness δ^* agree to within 4% on the average, with a maximum difference of 11%. The value of u_τ obtained from the equation of Schlichting agrees to within 10% on the average with a maximum deviation of 20% with that obtained from the slope of the velocity profile for $Y^+ \leq 5$. The values of u_τ as given by the equation of Schlichting are on the average slightly lower than those found empirically. It should be pointed out, however, that the equation of Schlichting's is based on experimental data for flat plates on which the flow was essentially turbulent from the leading edge onward. Since a considerable length of laminar boundary layer may exist in the forward portion of the flume this may account, at least in part, for the difference.

2. Laminar Sublayer Velocity Profiles

In Figures 17 through 22 graphs of the velocity profile in the region of the laminar sublayer are shown in the form of U^+ vs Y^+ for the four centerline velocity profiles of 0.129, 0.254, 0.498 and 0.769 ft/sec., and the off center profiles at 0.129 and 0.491 ft/sec. free stream velocity respectively. Figure 23 is a plot of the data points in the laminar sublayer for the six velocity profiles. These curves are an enlargement of the sublayer region shown on Figures 24 through 29 which are discussed in Section VI, Part A-3. In reducing the data for the plots for velocities in the region below $u = 0.1$ ft/sec. the calibration curve of Figure 32 was used. This curve was obtained from a direct calibration of the probe in a towing tank. Such a curve was found necessary since for velocities below 0.1 ft/sec., the value as derived from the hot film reading by means of King's equation was found to be consistently low. Above 0.1 ft/sec. accuracy of the probes was satisfactory. Section VI, Parts A-4 and 5 give more information on the accuracy and consistency of velocity measurements.

Straight lines were fitted to the points in the enlarged plots of U^+ vs Y^+ for the laminar sublayer region. It is noted that the lines for the profiles at different free stream velocities do not exactly coincide, also if the lines were extrapolated, the U^+ intercepts at $Y^+ = 0$ would differ slightly from zero.

The explanation for both of these discrepancies could well be experimental errors. If the confidence intervals of the straight lines fitted to the data points as well as inaccuracies in determining the probe location are considered, these could nearly account for the non-zero U^+ value in several instances. In addition there is the interference effect of the probe in the vicinity of the wall which is difficult to evaluate.

On the other hand it should be kept in mind that flow in the so-called laminar sublayer is unsteady and quite complicated, often involving three dimensional motion and periodic disturbances. Some such types of disturbances were described by Runstadler, Kline and Reynolds [42] and further evidence for disturbances reaching very close to the wall ($Y^+ < 0.5$) was obtained by Reiss and Hanratty [40]. Some of the data collected in the present investigation also supports these previous observations. For such a complicated flow field then, the average velocity profile for $Y^+ < 5$ could well be better fitted by a curved rather than a straight line. In that case the straight line extrapolation would not be representative of the true profile near the wall. It may be noted that past investigators have had similar difficulties when extrapolating lines fitted to data in the laminar sublayer to the wall. Nikuradse's [33, 35] results for example involved a shift of about $Y^+ = 7$. It should be stated here, however, that the suggestion that there may be actual slip at the wall so that U^+ should not go to zero is not believed to be a reasonable conclusion.

3. Velocity Profiles

The velocity profiles in the water channel were obtained by means of the hot film anemometer as described earlier. Vertical surveys at the center of the channel were conducted at each of the four free stream velocities of 0.119, 0.254, 0.498 and 0.769 ft/sec. Two additional velocity profiles were taken in a vertical plane, 5 in. off the channel centerline at the free stream velocities of 0.491 and 0.129 ft/sec., and furthermore a rather complete survey was conducted for a free stream velocity of 0.351 ft/sec.

The centerline velocity profiles for the four free stream velocities are plotted in Figures 24 through 27 in the universal form of U^+ vs Y^+. As may be seen from these profiles, the shape corresponds to that of a typically fully developed turbulent profile. The velocity profiles show the characteristic behavior of a "buffer region" for $5 \leq Y^+ \leq 30$, and of a turbulent core for $Y^+ > 30$. The velocity profiles for the turbulent core are fitted to the form

$$U^+ = A + B \log Y^+ . \tag{19}$$

The constants fitting the data best were selected by the method of least squares and are shown in Table 4. A comparison of the constants A and B determined from the data of this investigation may be made with the values determined by several other experimenters. Table 5 lists these values for comparison.

The average value of the constants for the centerline velocity profiles at 0.119, 0.254, 0.769 ft/sec. agree to within 5% with the values found by Nikuradse and Donch who worked with a pipe and a channel respectively. The conclusion drawn from the centerline velocity profiles is that the boundary layer existing near the channel bottom was fully turbulent and had a shape reasonably close to that found by other investigators in pipes or on flat plates.

The profile at 0.498 ft/sec. is excluded because it is suspect of an error due to severe corrosion noted on the legs of the hot film probe used to measure the buffer and core profiles. The velocity measurements in the sublayer at this velocity were made with a different probe and thus the friction coefficient is not suspect of error due to probe corrosion. Despite the fact that the core profile for 0.498 ft/sec. does not agree as closely with the other profiles, it also exhibits the characteristics of a fully turbulent velocity profile. This information is of some use for the present purpose and it is included here for this reason.

Since secondary flow is known to exist in a channel of rectangular cross section, as used in this investigation, two off center velocity profiles and a general velocity survey were made to determine the extent of the secondary flow. Of main interest here is the uniformity of the velocity profile across the channel width. The velocity profiles at 0.491 and 0.129 ft/sec., 5 in. off the channel centerline are shown together with the centerline velocity profiles in Figures 30 and 31. Although there are, as one would expect, differences in the profiles, the differences were not considered significant for the purpose of this investigation. The interest in this investigation is confined to the wall region at the channel center. A velocity survey was also made of the channel cross section at the intermediate free stream velocity of 0.351 ft/sec. There is again some change in the velocity at a given distance from the wall in traversing the width of the channel. Table 6 gives the mean velocities at given distances from the wall, together with the maximum and mean deviations from the average value for a distance of 8 in. from the channel centerline. As can be seen the maximum deviation in any case is 5.4% whereas the average is 2.9%. A plot of the velocity survey data is shown in Figure 33.

The change in velocity is small and indicates that the average velocity components in the direction of the channel width must be small compared to those along the axis of the channel. Consequently the secondary flow is not expected to have a major effect on the cavity flow. The percentages of velocity variation are, in fact, of the same relative size as the accuracy of the velocity measurements. The conclusion drawn from the off center velocity measurements is that the velocity in the channel is very uniform over a width of 16 in. or ± 8 in.

from the channel centerline. There is no reason to suspect that the uniformity of the boundary layer would change substantially at the other velocities.

In summary the boundary layer velocity profiles indicate the boundary layer existing ahead of the wall cavities is a typical fully developed turbulent profile much as would occur in a pipe or on a flat plate. Furthermore the velocity profile does not show significant changes with lateral position in the central portion of the channel, which is the portion where the principal experiments were conducted. It is therefore reasonable to conclude that flow conditions about a wall roughness in this channel are typical of those to be found in a pipe or on a flat plate.

4. Confidence Limits of the Velocity Profiles

The calibration data of the hot film anemometer system presented in Section VI, Part A-5 describes the general level of accuracy for individual velocity measurements. In addition to this calibration data a statistical analysis [20] of the velocity profile data was made to determine the confidence intervals of the constants of the curves fitted to the data. This statistical analysis was made for the core profiles, which were fitted to an equation of the form

$$U^+ = A + B \log Y^+ \tag{20}$$

and for the laminar sublayer profiles which were fitted to an equation of the form

$$u = C_1 y + C_2 \quad . \tag{21}$$

The confidence intervals for the constants were computed at the 90% confidence level in all cases. The slope of the velocity profiles in the laminar sublayer region (the constant C_1 of Equation (21)) had confidence intervals of ± 19%, ± 6.4%, ± 6%, ± 12% and ± 6% for the four centerline velocity profiles at free stream velocities of 0.769, 0.498, 0.254 and 0.129 ft/sec. and the off center profile at 0.491 ft/sec. respectively. Table 4 shows the confidence intervals for the constants A and B of Equation (20) as fitted to the velocity data of the turbulent core ($Y^+ > 30$). The average confidence interval for A is ± 4.5% with a maximum of 6.5% and the average for B is ± 6.3% with a maximum of ± 16%. Although this statistical analysis does not include systematic errors it does indicate the consistency or repeatibility of the velocity measurements.

5. Hot Film Anemometer System Calibration

The hot film anemometer system, consisting of the hot film probe, anemometer and linearizing circuit must be calibrated in order to make measurements of unknown velocities. The calibration methods used for the system consisted of two separate procedures.

For the first procedure, King's Law (Equation (12)) was assumed to hold and the calibration procedure consisted of determining the constants. King's Law may be rewritten in the form

$$I^2R = C_3 + C_4 \sqrt{u} \tag{22}$$

and two known velocities are then sufficient to determine the constants C_3 and C_4. In actual use recalibration is necessary at 20-30 minute intervals, and it was convenient to use zero velocity and the free stream velocity in the channel as the two velocity references. The free stream velocity in the channel was determined by a propeller probe at the velocities above 0.25 ft/sec. and by timing a dye spot at lower velocities. The use of zero velocity in order to determine the constant C_3 of Equation (22) is not rigorously correct since Equation (22) does not apply when free convection effects are important.

In order to determine the error which would be introduced into the velocity measurements by using the two point, free stream and zero velocity calibration method, a second calibration test was performed with the aid of a tow tank. The tow tank consisted of a tank of still water through which the probe could be towed on a carriage driven by a variable speed D. C. motor. In addition to determining the accuracy of the two point calibration procedure the tow tank tests also indicate the applicability of Equation (22), King's Law. In the tow tank tests, the constants C_3 and C_4 were determined as before by using a known velocity and zero velocity. Next runs were made at velocities between zero and the upper known velocity, and readings taken of the velocity as indicated by the hot film anemometer system and as indicated by determining the time for the carriage to traverse a known distance. The data gathered using this procedure are shown in Figure 32. One coordinate of this graph, U_1, represents the velocity as computed from the probe readings by means of King's equation in which C_3 and C_4 were determined as described above. The other coordinate, U_t, represents the velocity as determined by timing the rate of motion of the carriage. Figure 32 shows that King's equation in conjunction with the two point calibration (free stream and zero velocity) yields very satisfactory results between 0. 1 and 1. 0 ft/sec. The average error for 45 data points in this range is 5% with a maximum of 13% in one instance. These data also confirm King's Law as a satisfactory representation for the relationship between heat transfer rate and velocity in this region.

Below 0. 1 ft/sec., however, the velocity as indicated by the hot film anemometer system is slightly but consistently lower than the true velocity. The error at 0. 05 ft/sec. is approximately 20%, and is due to the overestimate of the value of C_3 in Equation (22) caused by using zero velocity as a calibration point. Below 0.05 ft/sec. free convection effects begin to show an influence. The curve of Figure 32 may be used to correct velocity measurements below 0.1 ft/sec. A correction using Figure 32 was applied to all velocity data below 0.1 ft/sec. It should, however, be noted that the tow tank calibration was made in "still" water, whereas the velocity in the boundary layer fluctuates. Consequently the corrections applied by using the curve of Figure 32 may not be exact and the margin of error in this range is estimated at ± 10%.

In summary, the hot film anemometer system measured velocities to within an average error of ± 5% from 0.1 to 1.0 ft/sec., and to within ± 10% below 0.1 ft/sec. when the curve of Figure 32 is used to correct the velocity readings.

B. Cavity Flow

1. The Characteristic Flow Modes

The purpose of this investigation was to determine what changes, if any, occur in the flow about a selected type of wall roughness element (a square cavity) as the thickness of the approaching laminar sublayer of a fully turbulent boundary layer and the roughness scale are varied. The investigation was to cover a range of ϵ^* values from the roughness transition region to the fully rough region. As already mentioned, a turbulent velocity profile having a sufficient laminar sublayer thickness was produced in a water channel 60 ft. in length. At free stream velocities from 0.125 to 0.75 ft/sec. ϵ^* values from 11.8 to 259 respectively were obtained for cavities ranging in depth from 1/8 to 1 in.

The flow in the cavities was studied both by direct observation and by means of still and motion pictures. In order to adequately describe the flow, several characteristic patterns which seemed to reoccur frequently were defined. A description of these flow patterns is given in the following paragraphs.

Five different characteristic patterns or flow modes were selected in order to categorize the flow observed. The five flow modes were termed "divide," "inflow," "weak exchange," "strong exchange," and "vortex." The names were chosen to indicate the general behavior of the flow in the cavity. Thus in the "divide" mode the dye stream emitted from the top of the upstream wall "divides" the cavity from the external flow with little or no fluid entering or leaving the cavity. This is illustrated in Figure 34 by a sketch and a typical photograph. The mean external flow in all photographs of cavity flow is from right to left. Note that the dye streak is seen to run parallel to the top of the cavity. The "inflow" mode, shown in Figure 35 again by a sketch and typical photograph, denotes flow into the cavity from the outside with the dye streak actually dipping into the cavity. The "weak exchange" mode denotes some removal of cavity fluid. Figure 36 shows a sketch and photograph of the flow in this mode in which the dye streak lifts above the downstream corner of the cavity at a shallow angle. The "strong exchange" mode, of Figure 37 denotes removal of cavity fluid as did the weak exchange. It is characterized, however, by the dye streak making a steep angle ($> 30^o$) with the horizontal, the removal of a large part of the cavity fluid, and a very noticeable removal of dye from the cavity. The induced velocities associated with the strong exchange are noticeably larger than those of the first three modes. Several sequences of 16 mm motion picture film shown in Figures 39, 40 and 41 serve to illustrate further these first four modes. Note in Figure 39 the first column, the 4th, 5th, 6th and 7th frames from the top which show the sequence of a strong exchange. The dye streak which had been entering the cavity in the 3rd, 4th and 5th frames reverses its direction in the 6th frame and is removed by the 7th frame. Each of these first three modes is superimposed on a more or less well defined vortex motion, which may be disturbed by a mode change or be entirely destroyed as in the case of a strong exchange. The fifth flow mode has been termed the "vortex" mode to indicate the existence of a well defined vortex within the cavity. Figure 38 shows a typical photograph and sketch of the vortex flow mode. In the "vortex" mode the cavity vortex is strong and essentially uninfluenced by outside disturbances. The flow over the opening of the cavity in this mode seems highly turbulent and effective fluid exchange seems to take place by relatively large scale turbulent mixing at the cavity opening. Thus, as can be seen in the photograph of Figure 38 and the 16 mm film of Figure 42, fluid may alternately enter and leave the cavity at the same time at different positions across the cavity opening.

It is realized that the foregoing five modes cannot be very rigidly defined. Nevertheless, it is felt that they are useful in describing the history of the flow in the cavities and its dependence on ε^*.

2. Cavity Flow

The description of the flow behavior in the cavity will be given in three parts, corresponding to values of ϵ^* below 100, to the range of ϵ^* between 100 and 200, and to values of ϵ^* above 200.

The motion in the cavities at $\epsilon^* < 100$ may be described in terms of the four flow modes of "divide," "inflow," "weak" and "strong" exchange. As the ϵ^* value increases the vortex motion becomes more pronounced, although it is still interrupted periodically by the strong exchange mode and disturbed to a lesser degree by other mode changes. The change from one mode to the next does not seem to follow a regular sequence. The various modes seem to follow each other in random fashion and no regular frequency is detectable. Of the above modes, the one termed "strong exchange" is perhaps the most interesting.

As was previously stated, the strong exchange has associated with it velocities which appear to be significantly larger than the velocities associated with the other modes. It causes a rather rapid, large outflux of cavity fluid and results in the complete destruction of the vortex which may have existed in the cavity. As with changes in the other modes, the occurrence of the strong exchange cannot be predicted by any preceding motion in the cavity.

A complete series of still photographs of each flow type together with a sketch of the flow, is shown in Figures 43 through 78, together with the motion picture frames of Figures 39 through 42.

An examination of the photographs shows that the general character of the cavity flow does not change in the range of ϵ^* values from 11-100.

As the ϵ^* value is increased from 100 to 200 the fifth mode (the so-called "vortex" mode) begins to appear as the vortex motion within the cavity becomes stronger. A study of the motion pictures at $\epsilon^* = 126$, for example, showed that, as before, the divide, inflow, weak exchange, strong exchange, occur, but that for small periods of time the vortex mode also appears. On the other hand the strong exchange mode which was such a characteristic feature of the flow at low values of ϵ^*, becomes less frequent.

At $\epsilon^* > 200$ the vortex flow mode becomes dominant, and the other four modes ("divide," "inflow," "weak" and "strong" exchange) have essentially disappeared. In fact, no examples of these modes are found in the motion pictures of cavity flow at $\epsilon^* = 201$ and 259 and only a well established vortex is evident at these ϵ^* values. Although exchange of fluid does take place between the cavity and the external flow, the effects of the flow causing this exchange are limited to the immediate vicinity of the opening of the cavity and at no time is the vortex motion destroyed by these exchanges. The cavity-external flow interface is wavy as shown by the dye streak bending into and out of the cavity in Figures 76 through 78. As a consequence the dye streak seems to flip into and out of the cavity as dye passes the downstream corner. This flipping is not the same phenomenon as that described by the "inflow" or "weak" exchange mode. In the "vortex" mode only the fluid in the immediate vicinity of the cavity opening takes part in the exchange with no disturbance to the cavity vortex motion. This may be contrasted to the influence which the inflow and weak exchange modes exert on the entire cavity fluid. The type of flow characteristic of the "vortex" mode and the flipping of the flow into and out of the cavity at the downstream corner has been observed and previously described in part by several investigators [3, 4, 12, 24, 47].

3. Cavity Strouhal Number

In an attempt to describe the cavity flow more quantitatively, the motion picture photographs were analyzed frame by frame, and each frame was classified as to the flow mode it represented. The number of frames examined in this manner corresponded to observation times from 2-5 minutes. These times are long compared to any time scale of cavity motion. From the classification of each frame into the flow mode it represents it is possible to determine the frequency with which changes from one mode to another occur, as well as the percentage of the total time occupied by each flow mode.

The average frequency of mode changes for $\epsilon^* < 100$ is here defined as the total number of modes (divide, inflow, weak or strong exchange) observed for a given time period divided by that period. This frequency may also be regarded as some indication of "activity" in the cavity. For $\epsilon^* = 125$ the cavity spends very small amounts of time in the "vortex" mode. This small percentage of time, however, is not significant and so for the frequency determination at $\epsilon^* = 125$ the same criterion is used as for values of $\epsilon^* < 100$. The observations made at $\epsilon^* = 201$ and 259 show that the cavity flow is characterized by the single "vortex" mode. For these two values of ϵ^* the average frequency as defined above would be zero. However, the frequency of another phenomenon may be defined, namely the number of times the flow flips into or out of the cavity at the downstream corner for a given time period.

For ϵ^* values over 200 this flipping in and out was used as the basis for a cavity frequency.

In order to make the two frequencies dimensionless, they were put in the form of a Strouhal number, with the cavity depth as the reference length and the shear velocity as the reference velocity. The Strouhal number then becomes

$$S = \frac{f\epsilon}{u_\tau} \tag{23}$$

where f is the frequency of mode changes, ϵ is the cavity depth, and u_τ is the shear velocity. This Strouhal number has a meaning slightly different from the usual one because the frequency is not a regular one. A plot of S vs ϵ^* is shown in Figure 79 and tabulated in Table 7 for the four cavity sizes and velocities investigated. A straight line is fitted to the points for $\epsilon^* < 100$ and interpolated to the origin. The values of S at $\epsilon^* = 201$ and 259 are shown on the same plot. The behavior of the cavity Strouhal number as defined by mode changes, when plotted vs ϵ^* shows a linear increase for values of $\epsilon^* < 100$. At $\epsilon^* = 201$ and 259 the Strouhal number as defined with the flipping of the streakline as a frequency, apparently becomes constant. There does seem to exist a good correlation between S and ϵ^*, which gives some confidence to the assumption that ϵ^* is a suitable similarity parameter.

4. Percentage of Time Occupied by Flow Modes

In addition to the frequency of mode changes a determination of the percentage times occupied by each flow mode was also made from the classification of motion picture frames. The percentage times did not show the same degree of correlation with ϵ^* as did the Strouhal numbers as may be seen from Table 7. It was not felt that any reliable conclusions could be drawn from this data. Several possible reasons for this lack of correlation were considered, in particular the consistency with which the duration of each mode could be determined. This point is discussed in some more detail in Section VII, Part B.

5. Summary of Cavity Flow Behavior

We may now briefly summarize the behavior of the flow in the cavities. At low values of ϵ^* ($11 < \epsilon^* < 100$) the flow in the cavities may be described in terms of four definite modes. The "strong exchange" mode is strikingly in evidence and the pure "vortex" mode is not observed. The average Strouhal number (based on the changes between the four modes) increases linearly with ϵ^* in this range. For ϵ^* values in the range 100 to 200 the fifth mode (the pure "vortex" mode) begins to appear and the other four modes gradually become less frequent, until beyond $\epsilon^* = 200$ the pure vortex mode is the only one visible. For this flow a different Strouhal number may be defined which is based on the waving stream passing over the opening of the cavity. This Strouhal number was found to be essentially independent of ϵ^*.

VII. DISCUSSION OF RESULTS

A. Similarity Parameter ϵ^*

The results of the present investigation have been presented using ϵ^* as the similarity parameter. As previously defined

$$\epsilon^* = \frac{\epsilon\, u_\tau}{\nu} \tag{24}$$

where ϵ is the cavity depth, $u_\tau = \sqrt{\tau_w/\rho}$ is the shear velocity and ν is the kinematic viscosity. The selection of ϵ^* as a parameter was made on the basis that the wall conditions should be the determining factor for the flow within a cavity, when the cavity size is comparable to laminar sublayer dimensions. If one then considers the wall region, the parameters of this region are the fluid properties, ρ and ν, the shear stress at the wall τ_w, and a length, such as the distance from the wall or a roughness height. Dimensional analysis then yields ϵ^* as the pertinent non-dimensional quantity to characterize the roughness. In the previously discussed investigation by Nikuradse [35] which was concerned with the frictional behavior of rough tubes, ϵ^* was also found to be the non-dimensional parameter reflecting the behavior of the friction coefficient. In forming ϵ^* Nikuradse used the sand grain height, and in the present investigation the cavity depth was used instead. Since the present investigation is concerned with conditions in the wall region, ϵ^* was again felt to be the parameter which should define the flow conditions within the cavities. The results of the present investigation are generally in support of this argument.

A word may be said about the range of values of the dimensionless roughness parameter ϵ^*. For the present somewhat artificial roughness, the observations indicate that fully rough flow occurs for values of ϵ^* in excess of about 200. In Nikuradse's experiments this flow regime was obtained for values of ϵ^* above 67. When comparing these measurements one has to keep in mind the arbitrary selection of the appropriate roughness dimension ϵ, as well as the difference in the roughness pattern. No particular meaning should, therefore, be attributed to the numerical difference of the value for ϵ^* beyond which the fully rough behavior begins. In addition the parameter ϵ^* is also dependent on the shear stress τ_w, which bears a relation to the main velocity profile. This relation depends on whether the surface along which the profile is developed is rough or smooth. In the present experiments the profile approaching the test section was developed over a smooth channel. A somewhat different relationship between the observations and ϵ^* might have occurred, had the approaching profile been obtained from a rough surface.

B. Cavity Flow Modes

In the previous section five modes of cavity flow were defined in order to better describe the general cavity flow picture. These modes were called "divide," "inflow," "weak exchange," "strong exchange," and "vortex." Reference will again be made to these patterns in the following discussion.

Perhaps the most striking finding of the present investigation was the presence of the "strong exchange" mode at low values of ε^* and its disappearance at large values of ε^*. In addition the occurrence of the three modes of divide, inflow and weak exchange at low values of ε^* was unexpected. The so-called "vortex" mode, on the other hand, which appeared for high values of ε^*, had been observed previously by several investigators. The "strong exchange" is of particular interest because of the significant velocities it induces in the cavity and consequently in the boundary layers along the cavity walls. The large disturbance characteristic of the strong exchange undoubtedly has an influence on heat and momentum transfer between the cavity and the external flow and on the heat exchange between the cavity walls and the cavity fluid. Some thoughts on the extent of the influence of the strong exchange are given later in this discussion.

Two quantitative approaches were attempted to better describe the cavity flow picture in terms of flow modes. Of these the more successful was that concerning the rate of change of the flow modes. The rate of change of flow modes was made non-dimensional as previously described in Section VI and presented in terms of a Strouhal number for the cavity, Figure 79. The fact that the Strouhal number seems to correlate well with ε^*, indicates that ε^* is probably the proper similarity parameter for the cavities in this investigation.

In addition to investigating the frequency of mode changes, the percentage of the total time which the cavity flow spent in each of the various modes was also determined and is tabulated in Table 7. It was stated that the correlation between the percentage of time spent in each mode and ε^* is poor. It is felt that this is primarily due to errors in measurement of the time spent in a mode. The major difficulty experienced in making this determination was the uncertainty as to the dividing point between mode changes. The characteristic forms of the modes are easily recognizable; however, intermediate flow conditions do occur during a mode change and the exact beginning or end of a mode is difficult to determine accurately. This uncertainty is reflected in the percentage time measurements. It should be mentioned that the data on percentage times did seem to fall into separate groupings according to the size of the cavity. This makes one suspect a possible lack of complete geometric similarity or the influence of some other dynamic parameter. Reiss and Hanratty have in fact reported an effect of the bulk Reynolds number on fluctuation in the boundary layer.

Accordingly an attempt was made to organize the percentage time data as a function of $Re_\delta = U_\infty \delta / \nu$ where δ is the turbulent boundary layer thickness and U_∞ the free stream velocity; however, this did not lead to any improved correlation. The inaccuracies in measuring the duration of each flow pattern is probably the principal cause for the poor correlation, but some further investigation of this point is required.

C. Possible Effects of Flow Mode Changes on Heat Transfer

One may next wish to consider the possible effect of the changes in flow modes and the general unsteady, random behavior of the cavity flow on heat transfer. Good heat transfer requires both transfer from the wall to the cavity fluid and from the cavity fluid into the main flow. The general observations of this investigation indicate that the exchange of fluid between the cavity and the external flow takes place quite readily. Charwat et al., [3, 4] also support this observation at least for very large ϵ^* values and their experimental environment. If the flow modes promote generally good fluid exchange between the cavity and the external flow, it follows that the cavity wall boundary layer remains as the major resistance to heat transfer from a rough wall. One may then speculate as to the influence of flow mode changes on this boundary layer and on the heat transfer. The mode appearing to cause the largest disturbance in the cavity flow is the one which was called "strong exchange." The strong exchange effects a large removal of cavity fluid and destruction of any vortex motion which might have existed in the cavity. This large disturbance probably destroys the wall boundary layer. Such action may lead to an important reduction of the thermal resistance of this layer, which, as stated earlier, is a major factor in the heat transfer from the cavity. In the same way, the flow during a change of mode is expected to have a similar effect on the wall boundary layers, although to a lesser extent. On the other hand the rather strong and stable vortex motion observed at large ϵ^* values would tend to have a more stable cavity wall boundary layer, and thus may not be as favorable to heat transfer. In all cases the resistance to heat exchange across the opening of the cavity is assumed to remain relatively low. The flow pictures substantiate this assumption. At low values of ϵ^*, for example, the "strong exchange" greatly promotes energy transfer across this opening, and at high values of ϵ^* the strong turbulence in the region of the opening accomplishes the same effect.

The foregoing conclusions, although quite qualitative, may actually serve to explain some of the trends in the heat transfer results of Dipprey [9]. These results show an increase in heat transfer coefficients in the transition region and a decrease in coefficients for higher values of ϵ^*. The rough tubes ($\epsilon/D = 0.0488$ and $\epsilon/D = 0.0138$) used by Dipprey show a maximum in the heat transfer coefficient at approximately the transition point to fully rough flow ($\epsilon^* = 67.5$) for all values of the Prandtl number (1.20, 2.79, 4.38 and 5.94) investigated. (Only limited information can be obtained from the third rough tube [$\epsilon/D = 0.0024$] as it reached the fully rough condition only for a single Prandtl number.)

The results quoted from the work of Dipprey were obtained in tubes with three dimensional sand grain type roughnesses. Nevertheless, other roughnesses may be expected to lead to similar results, and this is indicated by the comparison of Dipprey's results with others obtained for different roughnesses. One may then on the basis of the present investigation, construct a flow picture for square cavities to account for the behavior of the heat transfer coefficient as a function of ϵ^* which may have some general validity.

The general pattern of cavity flow as described before seems to be the following. For values of ϵ^* between 11.5 and 100 the cavity flow picture is described by the four modes of divide, inflow, weak and strong exchange. The flow fluctuates between these modes with no apparent systematic variation. Large disturbances, the strong exchange, greatly disturb the cavity flow for about 10% of the time with smaller but significant disturbances caused by the other flow modes. The Strouhal number, which as defined here may be considered as an indication of "activity" in the cavity also increases directly as ϵ^*. The picture of cavity flow consists of large fluctuations, and increasing activity in the range $11 \leq \epsilon^* \leq 100$. Correspondingly one may now expect the heat transfer coefficient to improve continuously in this range. As higher values of ϵ^* ($\epsilon^* > 100$) are approached, the steady cavity vortex develops and the flow no longer changes from one to the other of the several flow patterns. The boundary layers in the cavity are then no longer being disturbed and the heat transfer coefficient will tend towards that determined by the steady vortex flow in the cavity. This coefficient could well be somewhat lower than that reached in the this is indicated by the comparison of Dipprey's results with others obtained for different roughnesses. One may then on the basis of the present investigation, construct a flow picture for square cavities to account for the behavior of the heat transfer coefficient as a function of ϵ^* which may have some general validity.

The general pattern of cavity flow as described before seems to be the following. For values of ϵ^* between 11.5 and 100 the cavity flow picture is described by the four modes of divide, inflow, weak and strong exchange. The flow fluctuates between these modes with no apparent systematic variation. Large disturbances, the strong exchange, greatly disturb the cavity flow for about 10% of the time with smaller but significant disturbances caused by the other flow modes. The Strouhal number, which as defined here may be considered as an indication of "activity" in the cavity also increases directly as ϵ^*. The picture of cavity flow consists of large fluctuations, and increasing activity in the range $11 \leq \epsilon^* \leq 100$. Correspondingly one may now expect the heat transfer coefficient to improve continuously in this range. As higher values of ϵ^* ($\epsilon^* > 100$) are approached, the steady cavity vortex develops and the flow no longer changes from one to the other of the several flow patterns. The boundary layers in the cavity are then no longer being disturbed and the heat transfer coefficient will tend towards that determined by the steady vortex flow in the cavity. This coefficient could well be somewhat lower than that reached in the region near $\varepsilon^* = 100$ where the alternating flow patterns are likely to reduce the boundary layer resistance. Consequently, a maximum in the heat transfer coefficient might be reached in this range. As the established vortex pattern corresponds to "fully rough flow" and the appearance of the several modes corresponds to the "roughness transition" range, the maximum of the heat transfer coefficient may be expected to occur for a value of ε^* just before "fully rough" flow is established.

D. Cause of Flow Mode Changes

One of the principal features of the flow in the cavities at low ϵ^*, was the unsteady nature of the flow, and one may wish to give some consideration to the cause for this behavior. At least two possible explanations come to mind. First, fluid in a rectangular cavity exposed to a shear may not be able to move stably in a two dimensional pattern. Instead it may have to break up into cells or some other three dimensional motion. Secondly, the observed instabilities and mode changes may be caused by the fluctuations in the turbulent boundary layer outside the cavity. There is also the possibility that these two mechanisms may combine to effect changes in the cavity flow mode. The results of the present investigation appear to support the hypothesis that outside pressure and velocity fluctuations play at least a dominant role in causing cavity flow mode changes, for the following reasons. First, successive cavities often have the same flow mode at the same time, indicating that the disturbance probably comes from the outside and is not bound to the cavity. Figure 80 shows a photograph in which successive cavities are in the same flow mode, the "strong exchange" mode in this case. Secondly, patterns of modes often travel to successive downstream cavities as if connected to a traveling wave in the outside flow. And thirdly, one would generally expect a less random and more systematic behavior (as, for example, caused by the appearance and disappearance of cells) if a cavity flow instability were the cause.

The work of Runstadler, Kline and Reynolds [42] lends further support for the thought that external disturbances are causing the changes in the flow in cavities, and particularly for the appearance of "strong exchanges" in successive cavities. These investigators made an extensive visual study of a turbulent boundary layer on a flat plate. In this investigation they noted so-called "turbulent bursts" during which fluid leaves the wall layer regions and penetrates into the buffer and core regions of the boundary layer. The "turbulent bursts" reported seem to be similar to the type of motion observed during a strong exchange mode as shown in Figure 80, and one could well imagine that for a rough surface these "bursts" would remove fluid not only from the wall layer (as in the case of a flat plate) but also from the roughness cavities.

The situation in the case of the strong established vortex at $\epsilon^* > 200$ is somewhat different from conditions at low values of ϵ^*. At $\epsilon^* > 200$ the roughness--or cavity depth--is large compared to sublayer dimensions. The average dimensionless penetration distance of the bursts corresponds most likely to some fixed value of Y^+, and consequently the bursts will affect less and less of the flow in the body of the cavity for high values of ϵ^*. In that case only the fluid near the opening is disturbed by the bursts and the main cavity flow consists of a fairly steady vortex driven by shear forces at the interface with the external flow.

That the cavity flow is three dimensional is clear from the flow pictures shown and mass conservation considerations within the cavity. At values of $\epsilon^* < 100$ where the modes "divide," "inflow," "weak" and "strong exchanges" are present, the velocity components induced along the axis of the cavity seem to extend to about 2 cavity widths or less. The above figure represents an estimate based on the observation of the axial motions of dye within the cavities. It is of interest that the strong vortex flow--although essentially two dimensional--also seemed to induce some axial dye motion. This may indicate that this type of flow is not purely two dimensional, but divides into a cellular structure as suggested by some authors [32].

All of the detailed information of this investigation was obtained from the fourth cavity downstream in a short series of cavities. However, it appeared that the flow did not significantly change from one cavity to the next and it was therefore felt that the fourth cavity gave a flow pattern typical of that occurring in a short series.

E. Summary

The purpose of the present investigation was to study by visualization methods the flow about individual roughness elements of a rough surface. The boundary layer thickness and roughness sizes were to be such that the flow would be dynamically similar to that about a roughness element for the transition region of the friction coefficient shown in Figures 1 and 2.

The roughness selected for this study is a two dimensional square cavity, of the geometry shown in Figure 3. Roughness dimensions ranged from 1/8 to 1 inch. The flow was made visible by using dye injection and studied by direct observation and by means of motion picture and still photographs.

Suitable boundary layer conditions were produced on the bottom surface of a water channel. The channel was of rectangular cross section, and 60 ft. in length. Using free stream velocities of from 0.1 to 0.75 ft/sec., the value of ϵ^* (the wall Reynolds number based on the cavity depth) varied from 11 to 250. Mean velocity measurements near the channel bottom confirmed that the boundary layer was fully turbulent and that its shape was close to that of the so-called "universal profile". The mean velocity measurements were made using a constant temperature hot film anemometer.

A study of the motion picture and still photographs showed that the flow which existed for ϵ^* values less than 100, was of a type which had not been previously observed. This flow was classified into four "modes", shown in Figures 34 to 37. The flow changed from one mode to the next in a random fashion. For ϵ^* values in excess of 200 the flow was similar to that previously observed by several investigators. The relatively steady flow observed at high ϵ^* values is believed to correspond to the hydraulically "fully rough" behavior and that for lower ϵ^* (< 100) to the roughness transition region.

The disturbances responsible for the unsteady flow for low values of ϵ^* are believed to come from the boundary layer flow outside the cavities. The largest disturbances may possibly correspond to the "turbulent bursts" described by Runstadler, Kline and Reynolds [42].

The unsteady flow at low ϵ^* values may well improve the heat transfer from the cavity walls by periodically destroying the wall boundary layer. This action may be responsible for the improved heat transfer coefficient in the transition region which has been noted in earlier experiments by Dipprey [9].

SYMBOLS AND ABBREVIATIONS

A	Constant used in King's Law and in the Universal Velocity Profile, Equations 12 and 19.
B	Constant used in King's Law and in the Universal Velocity Profile, Equations 12 and 19.
C_3	Constant in King's Law as written in Equation 22.
C_4	Constant in King's Law as written in Equation 22.
C_f	Friction coefficient $C_f \equiv \frac{\tau_w}{1/2 \; \rho \; u_\infty^2}$
C_h	Heat transfer coefficient $C_h \equiv \frac{\mathring{q}}{\rho u \; C_\rho \; [T_w - T_L]}$
D	Tube diameter.
f	Frequency of mode changes [mode changes/sec.].
I	Current in hot film [amps.].
Nu	Nussult number.
R	Resistance of hot film probe [ohms].
Re_x	Reynolds number of a flat plate based on the distance from the leading edge, $Re_x = \frac{U_\infty x}{\nu}$
S	Strouhal number $S = \frac{f\epsilon}{u_\tau}$
t	Time
U_∞	Free stream velocity, [ft/sec.]
U^+	Dimensionless velocity $U^+ = \frac{u}{u_\tau}$

u	Local mean velocity, $u = u(y)$
u_τ	Shear velocity $u_\tau = \sqrt{\tau_w / \rho}$
x	Length from the entrance section of the channel or the leading edge of a flat plate.
y	Distance from flat plate or channel bottom.
Y^+	Dimensionless distance from flat plate or channel bottom, $Y^+ \equiv \frac{y\, u_\tau}{\nu}$

Greek Letters:

δ	Thickness of the turbulent boundary-layer.
δ^*	Displacement thickness of the turbulent boundary-layer $\delta^* \equiv \int_0^\infty \left(1 - \frac{u}{U_\infty}\right) dy$
ϵ	Roughness dimension, sand grain height, cavity depth
ϵ^*	Dimensionless roughness parameter $\epsilon^* = \frac{\epsilon\, u_\tau}{\nu}$
ν	Kinematic viscosity
ρ	Density
τ_w	Wall shear stress

REFERENCES

1. Bradshaw, P., Johnson, R. F., "Turbulence Measurements with a Hot Wire Anemometer," Notes on Applied Science, No. 33, Her Majesty's Stationary Office, London (1963).

2. Chapman, D. R., "A Theoretical Analysis for Heat Transfer in Regions of Separated Flow," NACA TN 3792.

3. Charwat, A. F., Dewey, C. F. Jr., Roos, J. N., Hitz, J. A., "An Investigation of Separated Flows--Part I: The Pressure Field," Journal of the Aerospace Sciences, Vol. 28 No. 6, 457-470 (1961).

4. Charwat, A. F., Roos, J. N., Dewey, F. C. Jr., Hitz, J. A. "An Investigation of Separated Flows--Part II: Flow in the Cavity and Heat Transfer," Journal of the Aerospace Sciences, Vol. 28 No. 7, 513-527 (1961).

5. Clauser, F. H., "The Turbulent Boundary Layer," Advances in Applied Mechanics, Vol. IV (1956).

6. Clutter, D. W., Smith, A. M. O, Brazier, J. G., "Techniques of Flow Visualization Using Water as the Working Medium," Report No. ES29075, Douglas-El Segundo (Apr. 1959).

7. Collis, D. C., Williams, M. J., "Two-Dimensional Convection from Heated Wires at Low Reynolds Numbers," Jour. Fluid Mech, Vol. 6, pt. 3, 357-84 (1959).

8. Cope, W. F., "The Friction and Heat Transmission Coefficients of Rough Pipes," Proc. Inst. of Mech. Engin., Vol. 105, pp. 99-105 (1941).

9. Dipprey, D. F., "An Experimental Investigation of Heat and Momentum Transfer in Smooth and Rough Tubes at Various Prandtl Numbers," Ph.D. Thesis, California Inst. Tech. (1961).

10. Dipprey, D. F., Sabersky, R. H., "Heat and Momentum Transfer in Smooth and Rough Tubes at Various Prandtl Numbers," Int. J. Heat and Mass Transfer, Vol. 6, 329-353 (1963).

11. Eckert, E. R. G., Drake, R. M. Jr., Heat and Mass Transfer, McGraw-Hill, New York (1959).

12. Folsom, R. G., Ph. D. Thesis, California Institute of Technology, (1932).

13. Fortescue, P., Hall, W. B., "Heat Transfer Experiments on The Fuel Elements," Jour. of British Nuclear Energy Conf., Vol. 2 No. 2, 83 (1957).

14. Handbook of Chemistry and Physics, 44th Edition, The Chemical Rubber Publishing Co., Cleveland, Ohio, (1963).

15. Hama, F. R., "Boundary-Layer Characteristics for Smooth and Rough Surfaces," Trans. Soc. of Naval Architecture and Marine Engineers, Vol. 62, 333-358 (1954).

16. Hastrup, R. C., "Heat Transfer and Pressure Drop in Artificially Roughened Tube at Various Prandtl Numbers," Mech. Engin. Thesis, California Inst. Tech. (1958).

17. van der Hegge Zijnen, B. G., "Modified Correlation Formula for Heat Transfer by Natural and Forced Convection from Horizontal Cylinders," App. Sci. Res., Vol. VI, Sec. A, p. 129 (1957).

18. van der Hegge Zijnen, B. G., "Heat Transfer from Horizontal Cylinders in a Turbulent Airflow," Appl. Sci. Res., Vol. VII, Sec. A., p. 205 (1958).

19. Hinze, J. O., Turbulence, McGraw-Hill, New York (1959).

20. Hoel, P. G., Introduction to Mathematical Statistics, John Wiley & Sons, Inc., New York, Second Edition (1954).

21. Kemeny, G. A., Cyphers, J. A., "Heat Transfer and Pressure Drop in an Annular Gap With Surface Spoilers," Journal of Heat Transfer, (May 1961).

22. King, L. V., "On the Convection of Heat from Small Cylinders in a Stream of Fluid," Phil. Trans. Roy Soc., Ser. A, Vol. 214, 373-432 (1914).

23. Klebanoff, P. S., Diehl, Z. W., "Some Features of Artificially Thickened Fully Developed Turbulent Boundary Layers with Zero Pressure Gradient," NACA TN 2475 (1951).

24. Knudsen, J. G., Katz, D. L., "Heat Transfer and Pressure Drop in Annuli," Chem. Engin. Progress, October 1950.

25. Laufer, J., "The Structure of Turbulence in Fully Developed Pipe Flow," NACA, Report No. 1174 (1954).

26. Laufer, J., "Investigation of Turbulent Flow in a Two-Dimensional Channel," NACA TN 2123 (1950).

27. Laurence, J. C., Sanborn, V. A., "Heat Transfer from Cylinders," Symposium on Measurement in Unsteady Flow, Presented at the ASME Hyd. Div. Conf., Worcester, Mass., May 21-23, 1962.

28. Ling, S. C., "Measurement of Flow Characteristics by the Hot Film Technique," University Microfilms, Publication No. 12, 905, Ann Arbor, Michigan, Ph.D. Thesis, State Univ. of Iowa (1955).

29. Logan, E. Jr., Jones, J. B., "Flow in a Pipe Following an abrupt Increase in Surface Roughness," Journal of Basic Engineering, Trans. of the ASME (March 1963).

30. Lukasik, S. J., Grosch, C. E., "Velocity Measurements in Thin Boundary Layers," Davidson Lab., T. M. 122, Stevens Inst. of Tech. Castle Point Sta., Hoboken, N. J. (1959).

31. Martinelli, R. C., "Heat Transfer to Molten Metals," A.S.M.E. Trans. Vol. 69, 947-959 (1947).

32. Maull, D. J., East, L. F., "Three-Dimensional Flow in Cavities," Jour. of Fluid Mech., Vol. 16.

33. Miller, Benjamin, "The Laminar Film Hypothesis," A.S.M.E. Trans. Vol. 71, 357-367 (1949).

34. Mills, R. D., "The Flow in Rectangular Cavities," University of London, Ph.D. Thesis (1961).

35. Nikuradse, J., "Laws of Flow in Rough Pipes," NACA TM 1292 (1950).

36. Nunner, W., "Heat Transfer and Pressure Drop in Rough Tubes," VDI-Forschungsheft 455, Series B, 22, 5-39 (1956) A.E.R.E. Lib/Trans. 786 (1958).

37. Owen, P. R., Thomson, W. R., "Heat Transfer Across Rough Surfaces," Jour. Fluid Mech., Vol. 15, pt. 3, 321-24 (1963).

38. Piercy, N. A. V., Richardson, E. G., Winny, H. F., "On the Convection of Heat from a Wire Moving Through Air Close to a Cooling Surface," Proc. Phys. Soc., Series B., Vol. 69 (1956).

39. Piret, E. L., James W., and Stacy, M., "Heat Transmission from Fine Wires to Water," Ind. and Engin. Chem., Vol. 39, p. 1098 (1947).

40. Reiss, L. P., Hanratty, T. J., "An Experimental Study of the Unsteady Nature of the Viscous Sublayer," A. I. Ch. E. Journal, Vol. 9, No. 2; 154-160 (1963).

41. Roshko, A., "Some Measurements of Flow in a Rectangular Cutout," NACA TN 3488, (1955).

42. Runstadler, P. W, Kline, S. J., Reynolds, W. C., "An Experimental Investigation of the Flow Structure of the Turbulent Boundary Layer," AFORS-TN-5241, Report MD-8, Thermosciences Division, Dept. of Mech. Engin., Stanford Univ., Stanford, Calif. (June 1963).

43. Sams, E. L., "Experimental Investigation of Average Heat-Transfer and Friction Coefficients for Air Flowing in Circular Tubes Having Square-Thread-Type Roughness," NACA RM E52D17 (1952).

44. Schlichting, H., Boundary Layer Theory, McGraw-Hill, New York (1955).

45. Seban, R. A., "Heat Transfer to the Turbulent Separated Flow of Air Downstream of a Step in the Surface of a Plate," ASME Paper, No. 63-HT-36.

46. Teller, E. M., "An Electrochemical Method of Visualizing the Boundary Layer," M.S. Thesis, Mississippi State College, Dept. of Aero. Engin. (1954).

47. Wieghardt, K., "Erhöhung des turbulenten Reibungswiderstandes durch Oberflächenstörungen (Increase of the Turbulent Frictional Resistance Caused by Surface Irregularities)," Forschungsbericht 1563, ZWB, (March 1942); also Jahrb., deutchen Luftfhartforschung (1943).

TABLE 1

MAJOR COMPONENTS USED IN LINEARIZING CIRCUIT

Component	Type Used
Operational Amplifiers	Model UPA-2 George A. Philbrick Researches, Inc. 127 Clarendon St. Boston 16, Mass.
Power Supply	Model R-100B George A. Philbrick Researches, Inc.
Douglas Quadration	Type A, Model 10 Dept. G-76, Douglas Aircraft Company, 3000 Ocean Park Blvd. Santa Monica, Calif.

TABLE 2

COMPARISON OF LOCAL FRICTION COEFFICIENTS

U_∞ [ft/sec.]	C_f Schlichting Eq. (5)	C_f Clauser Eq. (13)	C_f Laminar Sublayer Velocity Profile
0.769	2.88×10^{-3}	2.98×10^{-3}	3.22×10^{-3}
0.498	3.15×10^{-3}	3.95×10^{-3}	4.23×10^{-3}
0.491 5" off ℄	3.15×10^{-3}	4.02×10^{-3}	5.10×10^{-3}
0.254	3.60×10^{-3}	4.45×10^{-3}	3.55×10^{-3}
0.129	4.13×10^{-3}	4.21×10^{-3}	4.94×10^{-3}
0.129 5" off ℄	4.13×10^{-3}	6.85×10^{-3}	3.36×10^{-3}

Eq. (5) $$C_f = \frac{0.0592}{(Re_x)^{0.20}}$$

Eq. (13) $$\sqrt{2/C_f} = 5.6 \log_{10} Re_{\delta*} + 4.3$$

δ^* = displacement thickness, which was determined from the empirical mean velocity profiles of this investigation.

TABLE 3

COMPARISON OF LOCAL SHEAR VELOCITIES

U_∞ [ft/sec.]	u_τ [ft/sec.] Schlichting Eq. (5)	u_τ [ft/sec.] Clauser Eq. (13)	u_τ [ft/sec.] Laminar Sublayer Velocity Profile
0.769	0.0291	0.0297	0.0308
0.498	0.0198	0.0221	0.0229
0.491 5" off C_L	0.0195	0.0220	0.0248
0.254	0.0108	0.0120	0.0116
0.129	0.00585	0.00592	0.00641
0.129 5" off C_L	0.00585	0.00755	0.00749

Eq. (5) $$C_f = \frac{0.0592}{(Re_x)^{0.20}}$$

Eq. (13) $$\sqrt{2/C_f} = 5.6 \log_{10} Re_{\delta*} + 4.3$$

$\delta*$ = displacement thickness which was determined from the empirical mean velocity profiles of this investigation.

$u_\tau = U_\infty \sqrt{C_f/2}$

TABLE 4

CONSTANTS A AND B OF THE EQUATION $U^+ = A + B \log_{10} Y^+$ FITTED TO THE TURBULENT CORE VELOCITY PROFILES AND THEIR 90% CONFIDENCE LEVELS

U_∞ [ft/sec.]	A	B
0.769	5.72 ± 8%	5.06 ± 4%
0.498	7.35 ± 5%	4.05 ± 2%
0.491 5" off ℄	5.02 ± 11%	4.64 ± 4%
0.254	4.27 ± 2%	5.87 ± 6%
0.129	5.15 ± 16%	5.51 ± 6%
0.129 5" off ℄	6.0	4.82

TABLE 5

CONSTANTS A AND B OF THE EQUATION $U^+ = A + B \log_{10} Y^+$ AS FOUND BY SEVERAL INVESTIGATORS

Investigator	Type of Apparatus	A	B
Nikuradse	Pipe	5.0	5.75
Nikuradse	Channel	5.0	5.75
Dönch	Channel	5.0	5.75
Laufer	Channel	7.2	5.75
Klebanoff and Diehl	Boundary-layer	4.2	5.75
Present Investigation Average Values	Channel Boundary-layer	5.01	5.48

Values of A and B for other investigators are given in Reference [23].

Average for the present investigation is composed of values at the free stream velocities of 0.769, 0.254 and 0.129 ft/sec. centerline profiles only.

TABLE 6

CHANNEL VELOCITY SURVEY AT $U_\infty = 0.351$ ft/sec.

y[in.]	$\overline{u}$[ft/sec.]	Max. Δu%	Avg. Δu%
9.6	.351	1.95	1.34
4.8	0.334	5.4	3.9
2.4	0.301	4.65	3.0
1.2	0.288	4.86	3.12
0.60	0.268	4.48	2.98

$\overline{u}$ is the average of four velocity readings at a given value of y, at distances of 0, 4, 8 and 12 in. from the channel centerline.

$$\Delta u\% = \frac{\overline{u} - u}{\overline{u}} \times 100$$

TABLE 7

CAVITY FLOW MODE DATA

Cavity	U_∞	ϵ^*	f		% Time in Flow Mode			
Size [in.]	[ft/sec.]		[mode changes/sec.]	$S = \frac{\epsilon f}{u_\tau}$	Divide	Inflow	Weak Exchange	Strong Exchange
1/8 × 1/8	0.255	11.8	1.02	0.936	15.0	55.4	25.2	4.19
1/8 × 1/8	0.510	24.3	4.60	2.04	28.6	35.9	27.8	7.7
1/4 × 1/4	0.127	13.1	0.310	0.951	17.2	37.7	35.8	9.34
1/4 × 1/4	0.127	22.7	0.834	1.58	12.6	52.1	26.7	8.58
1/4 × 1/4	0.520	49.3	3.44	3.00	17.9	44.7	32.6	4.89
1/4 × 1/4	0.835	68.5	5.12	3.22	19.9	23.9	50.8	5.42
1/2 × 1/2	0.123	25.6	0.25	1.68	11.3	33.3	41.3	14.1
1/2 × 1/2	0.252	46.6	1.02	3.76	18.0	40.9	33.3	7.3
1/2 × 1/2	0.510	96.6	3.78	6.72	23.4	34.9	35.3	6.29
1/2 × 1/2	0.768	126.	7.35	10.0	18.7	24.6	49.2	7.43
1 × 1	0.121	50.4	0.315	3.88	11.4	28.2	49.0	11.4
1 × 1	0.262	95.8	0.705	4.99	8.9	68.6	22.5	0
1 × 1	0.259	201.	2.32	9.63	-	-	-	-
1 × 1	0.788	259.	3.33	8.85	-	-	-	-

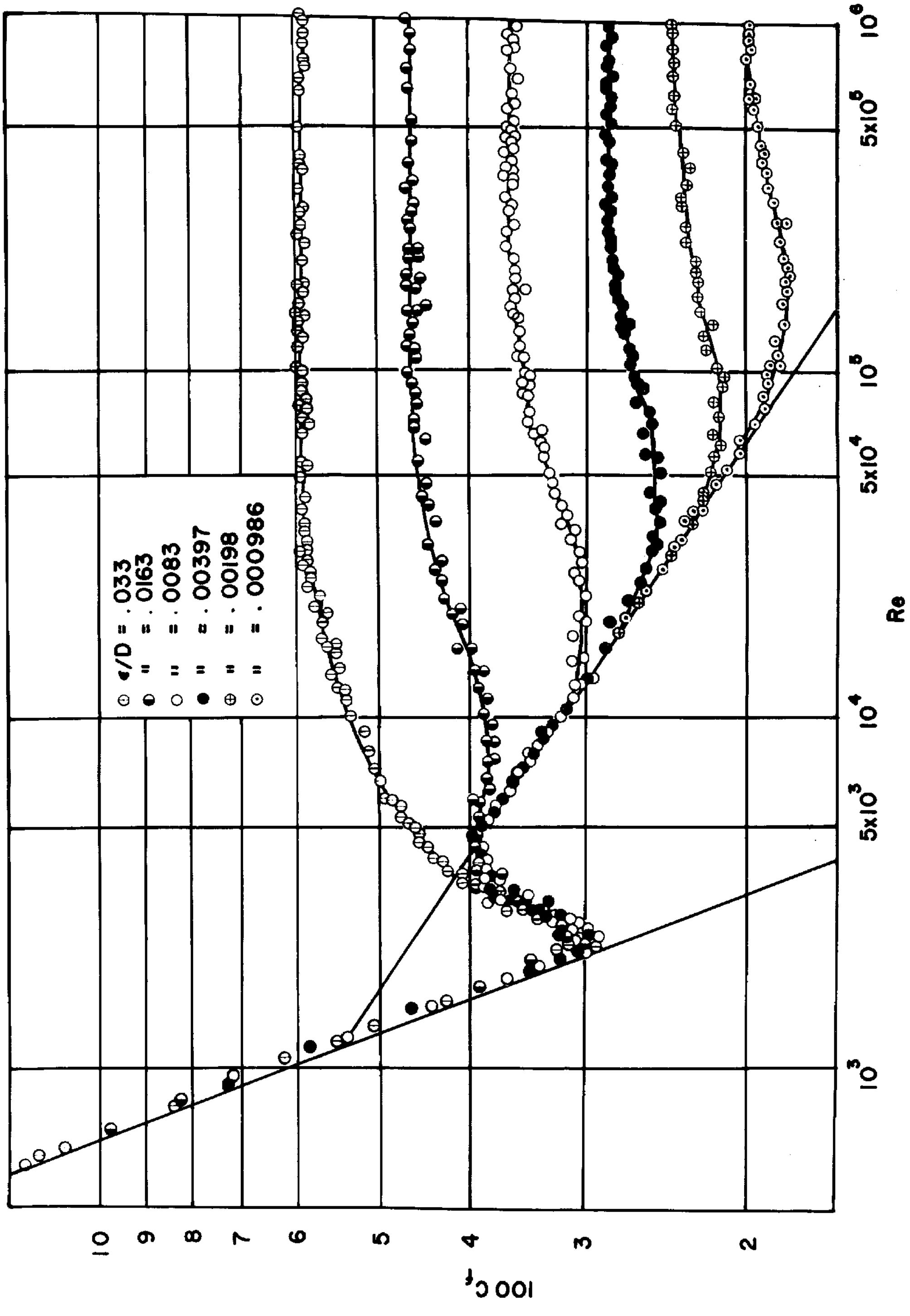

Fig. 1. C_f vs. Re_d from Nikuradse's measurements in sand grain roughened pipes.

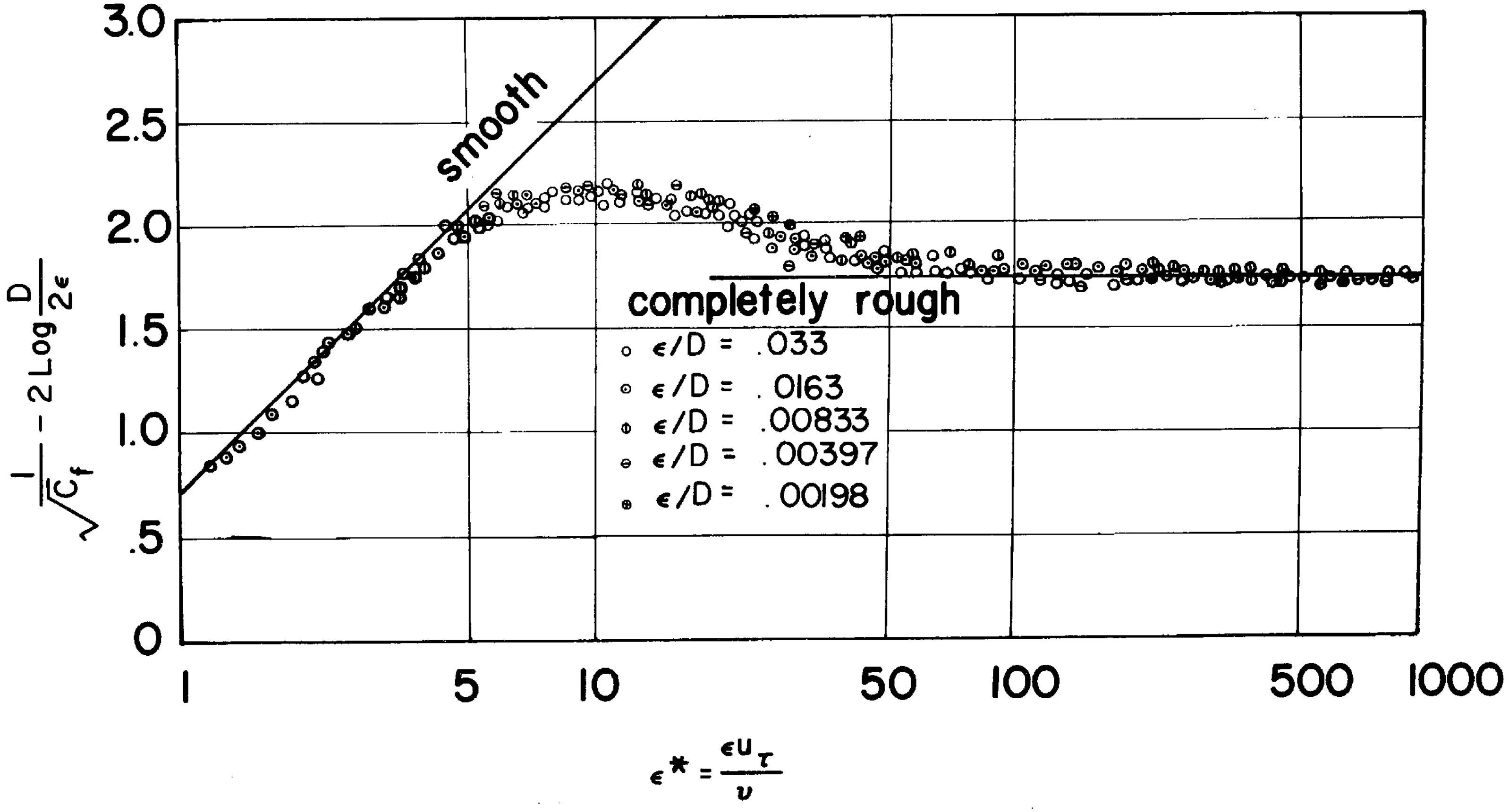

Fig. 2. The parameter $\frac{1}{\sqrt{C_f}} - 2 \log \frac{D}{2\epsilon}$ as a function of ϵ^* from Nikuradse's friction coefficient measurements for sand grain roughened pipes.

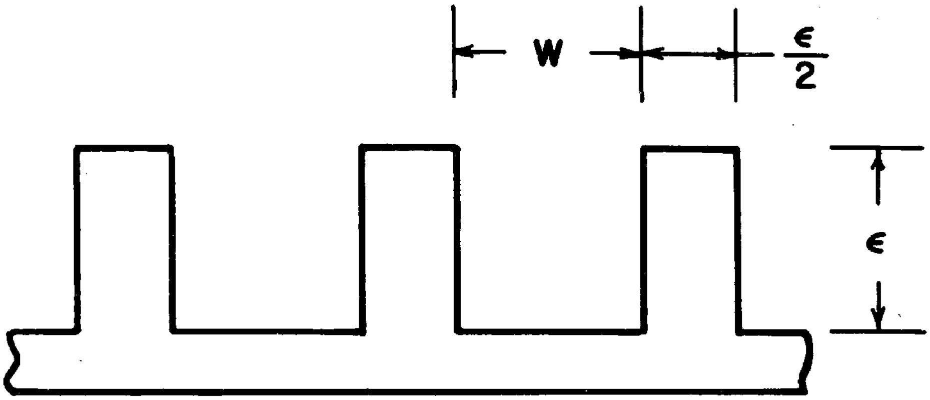

ϵ = Cavity Depth

W = Cavity Width

ϵ = W for all cavities

Fig. 3. The cavity geometry.

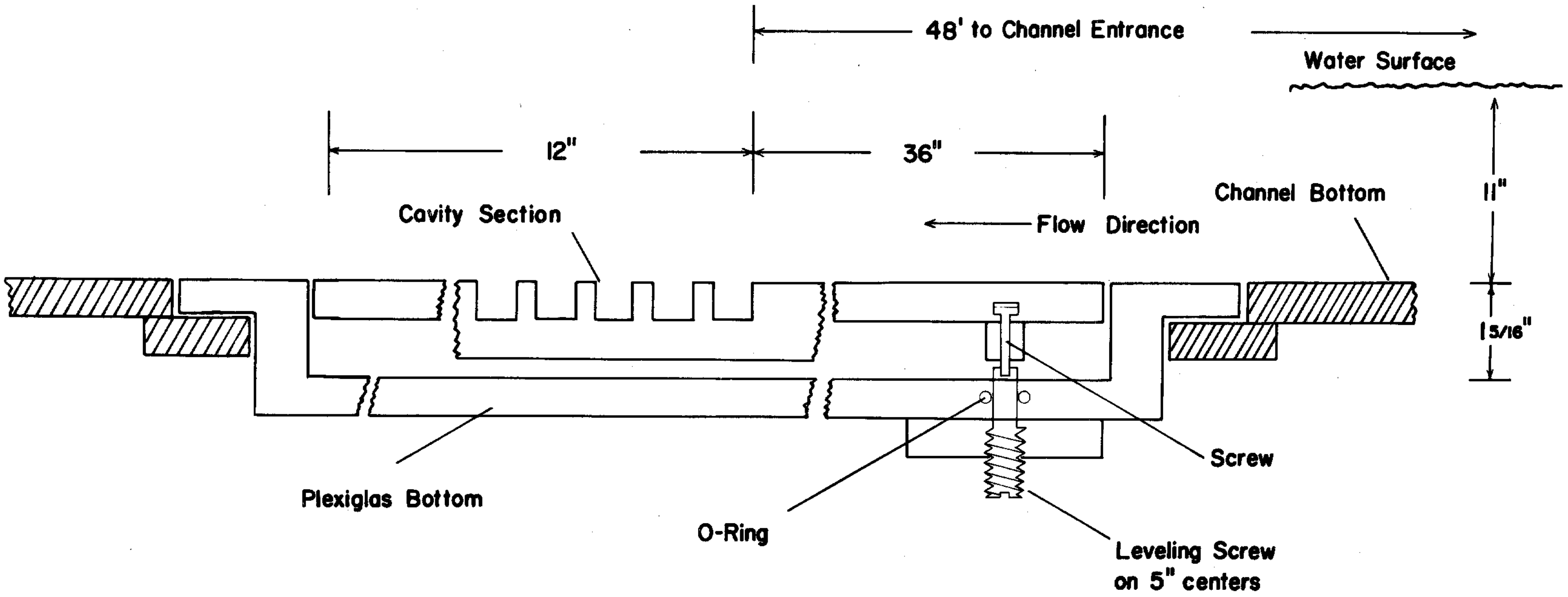

Fig. 4. Cross section of cavity installation relative to the channel bottom.

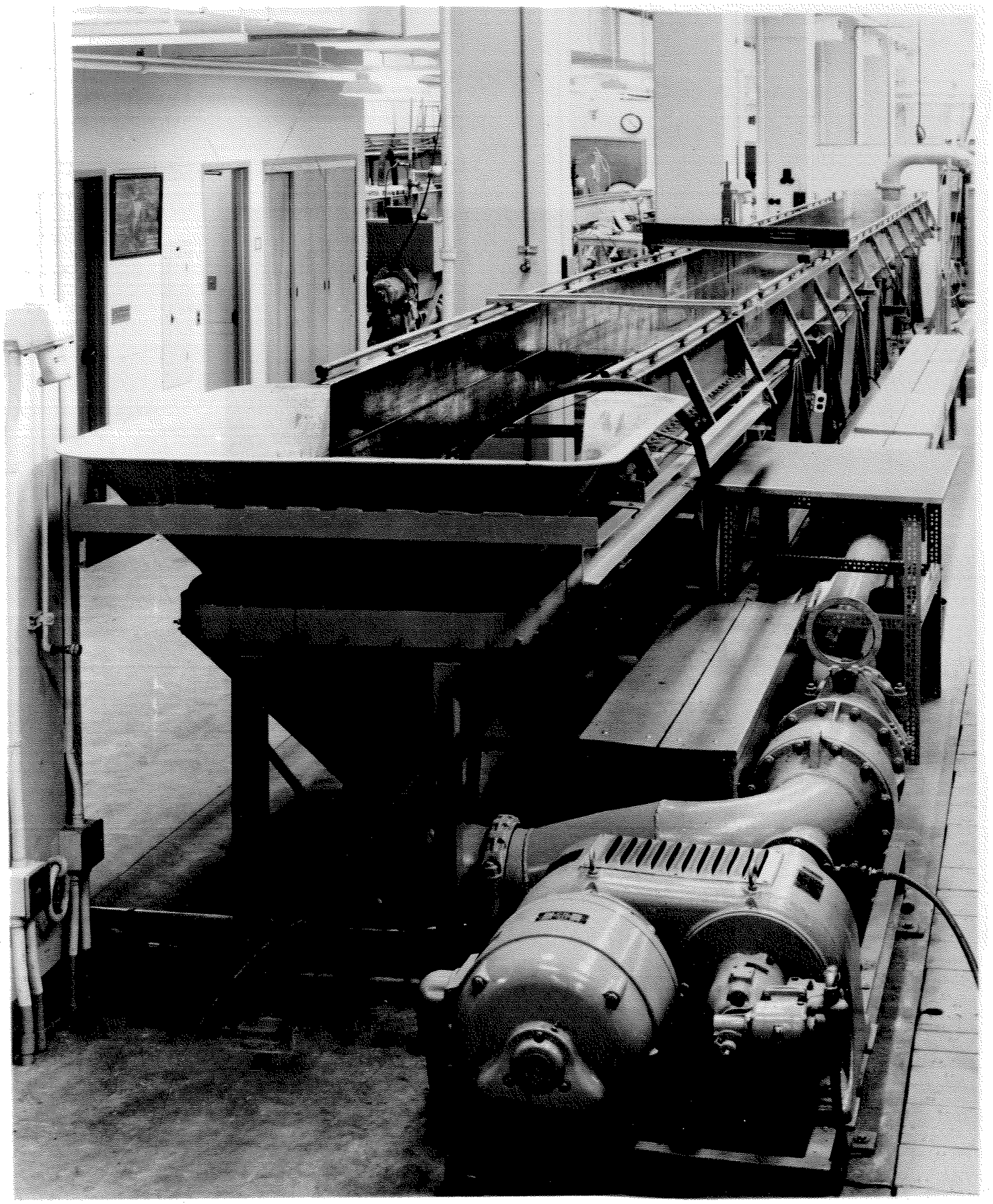

Fig. 5. Photograph of the channel looking upstream.

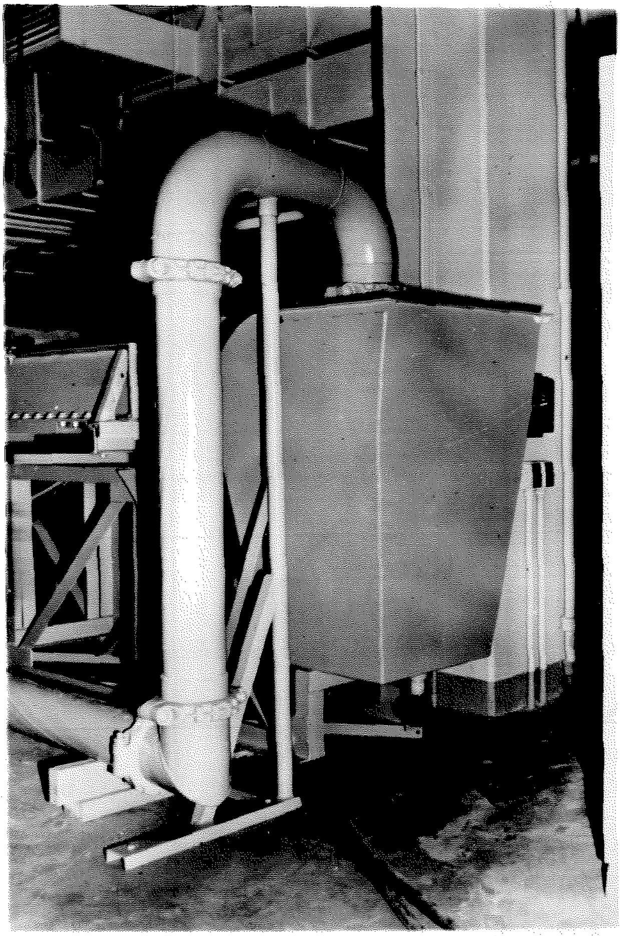

Fig. 6. Photograph of the channel entrance section.

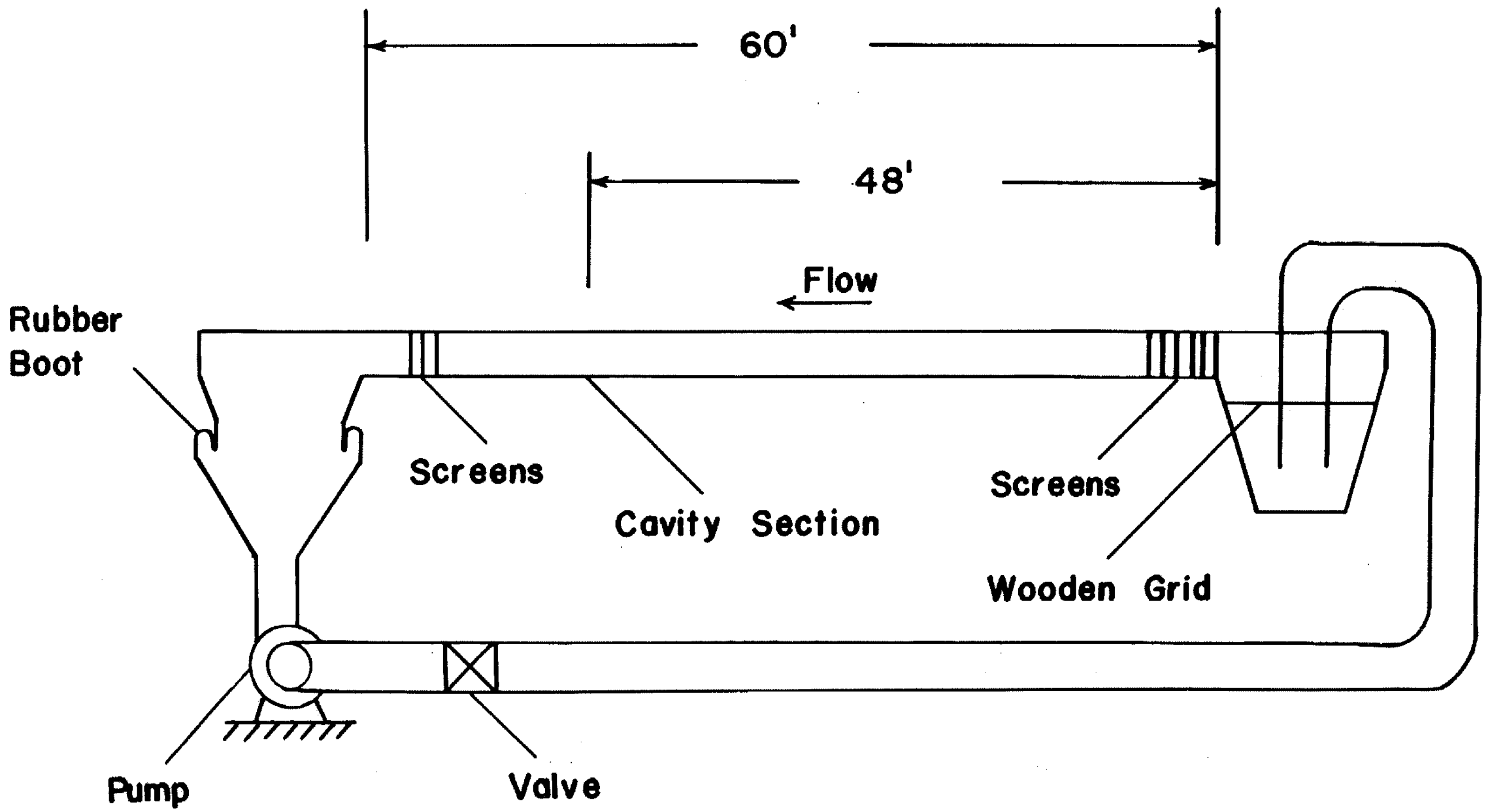

Fig. 7. Diagram of the channel, return pipe circuit.

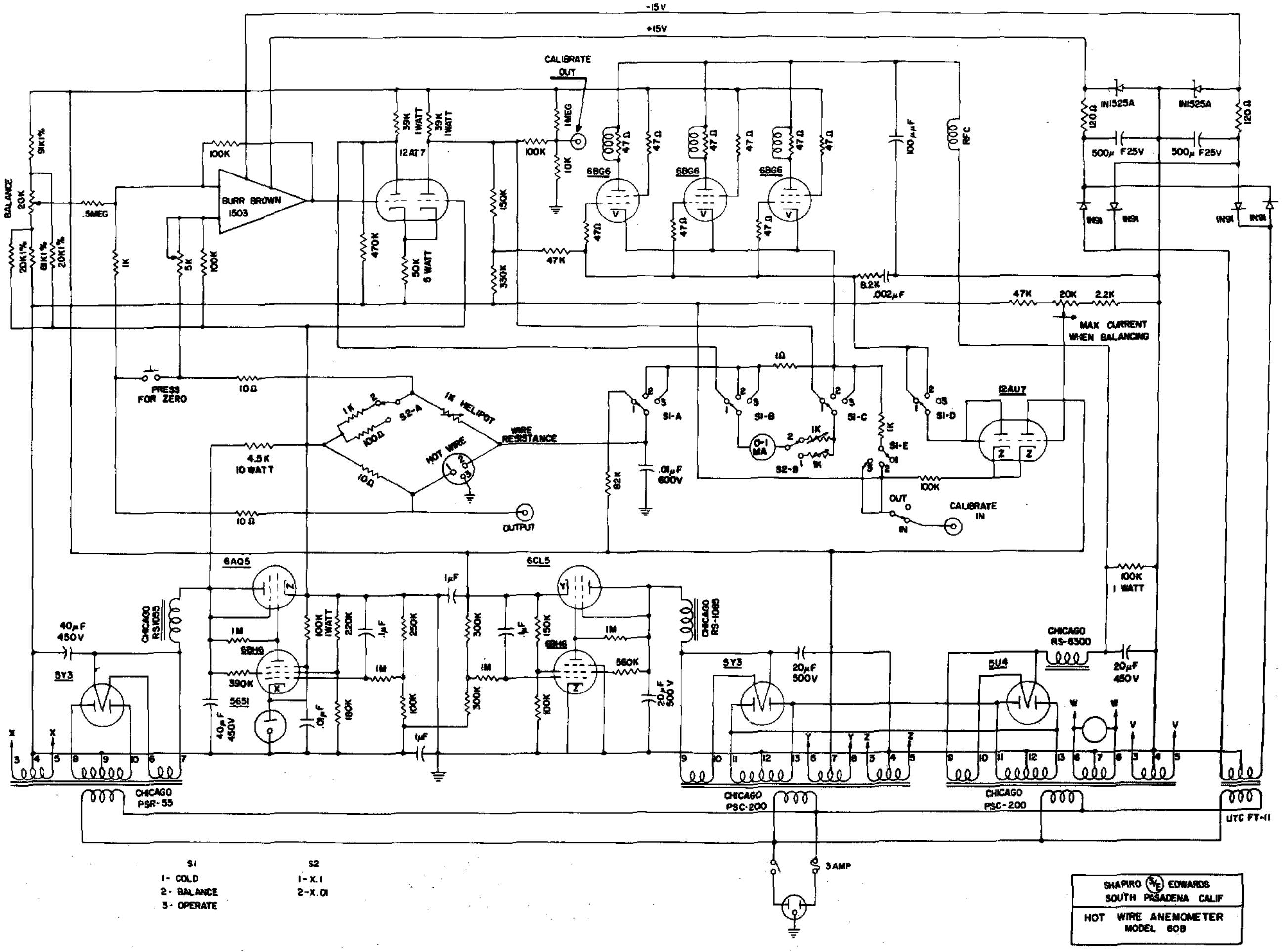

Fig. 8. Circuit Diagram of Shapiro & Edwards Model 60B, hot wire anemometer.

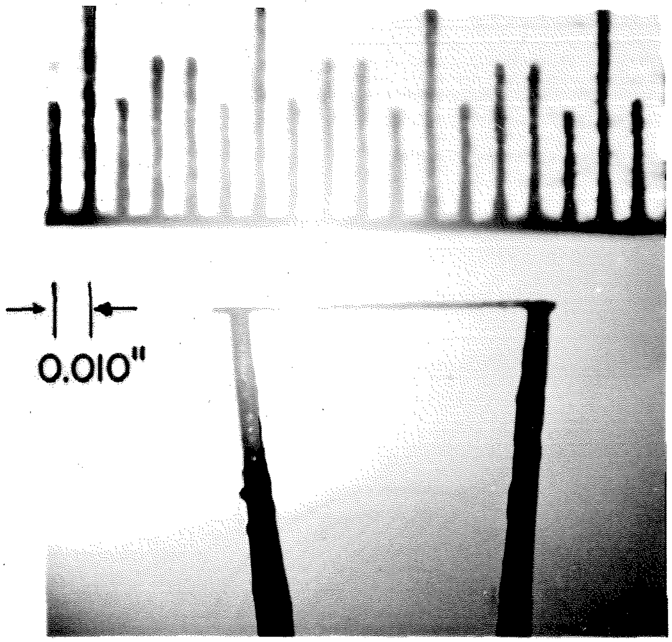

Fig. 9. Photograph of 0. 002 in. dia. platinum hot film probe.

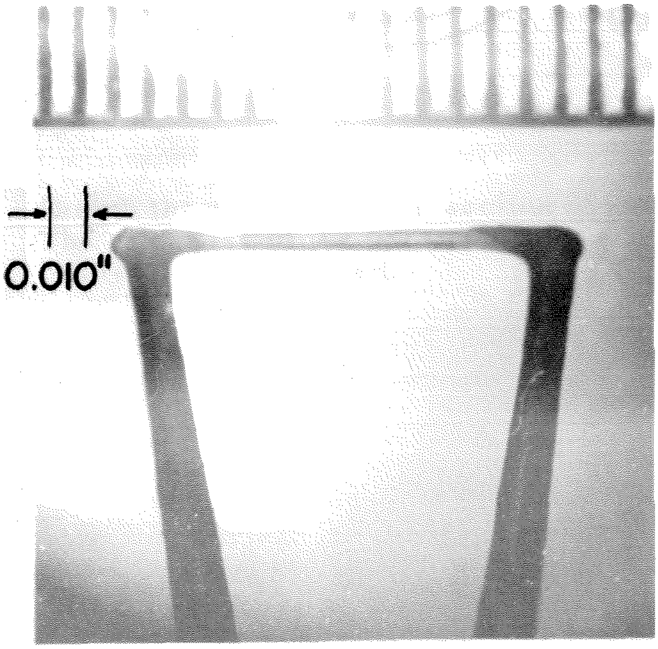

Fig. 10. Photograph of 0. 006 in. dia. platinum hot film probe.

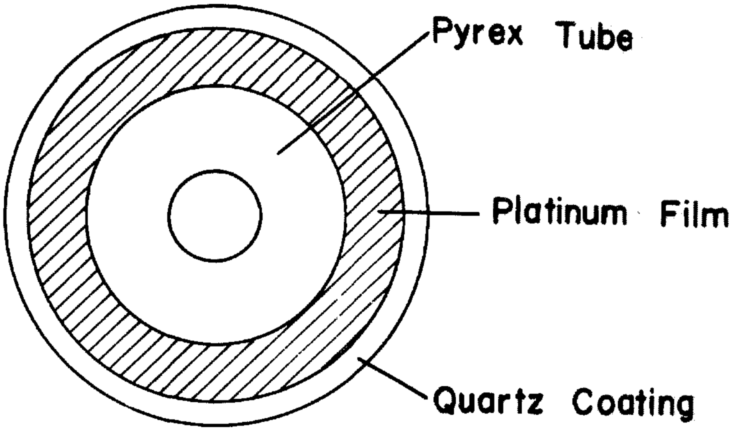

Fig. 11. Sketch through the active section of the hot film probes. The thickness of the platinum film and quartz coating is greatly exaggerated.

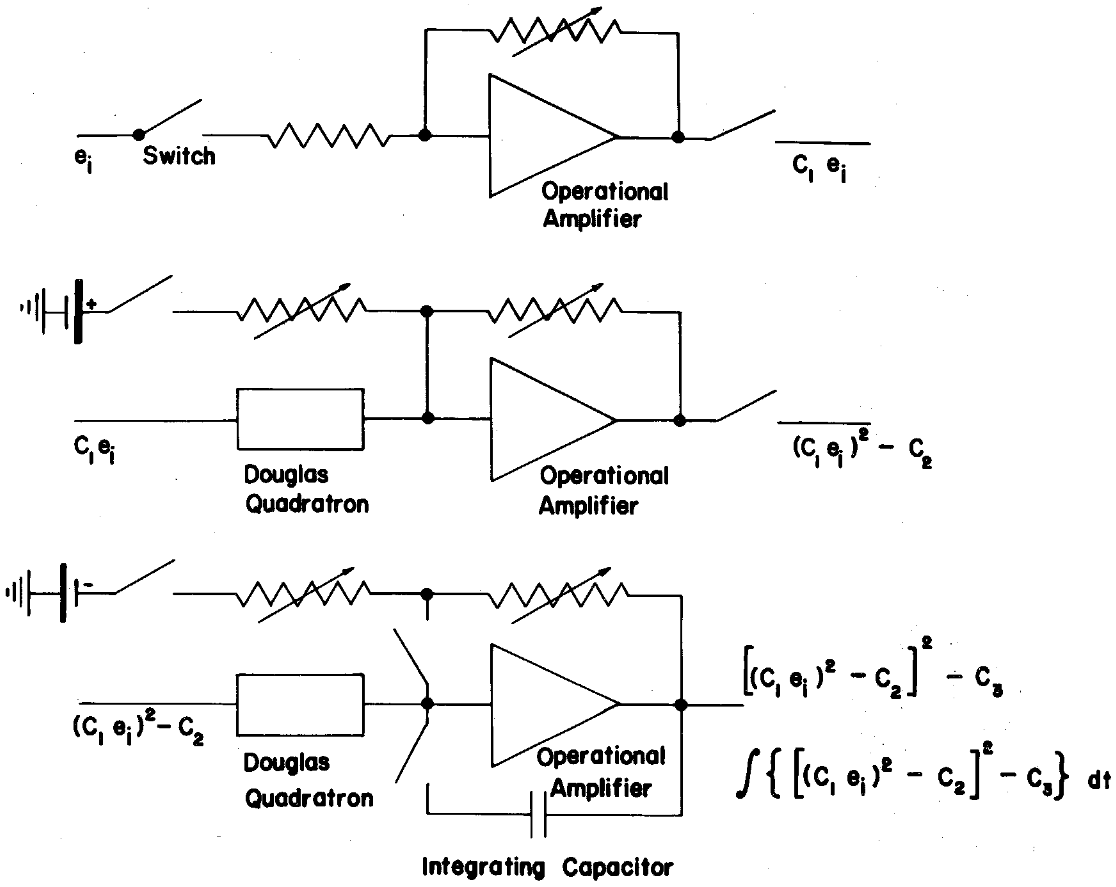

Fig. 12. Linearizing circuit diagram.

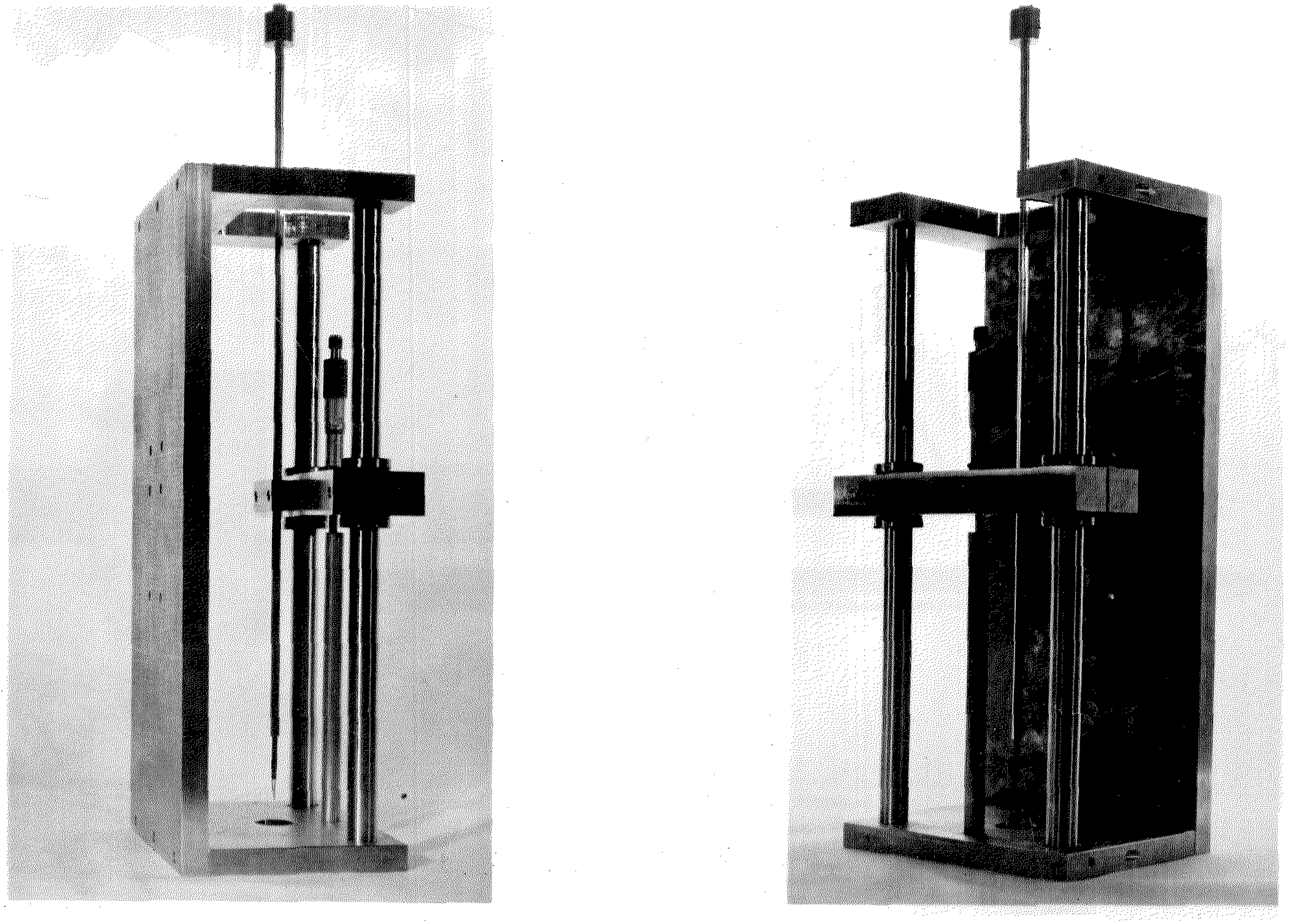

Fig. 13. Photographs of the traversing mechanism with the hot film probe.

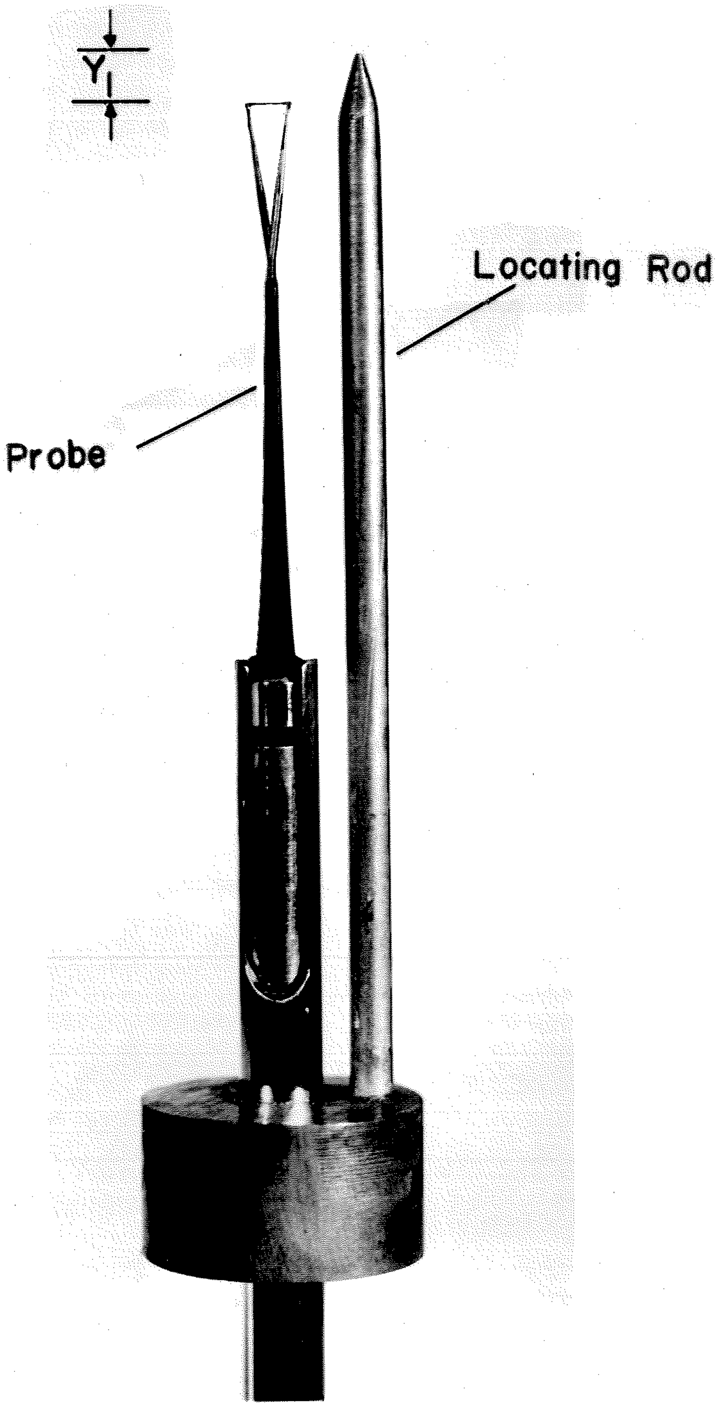

Fig. 14. The hot film probe and locating rod.

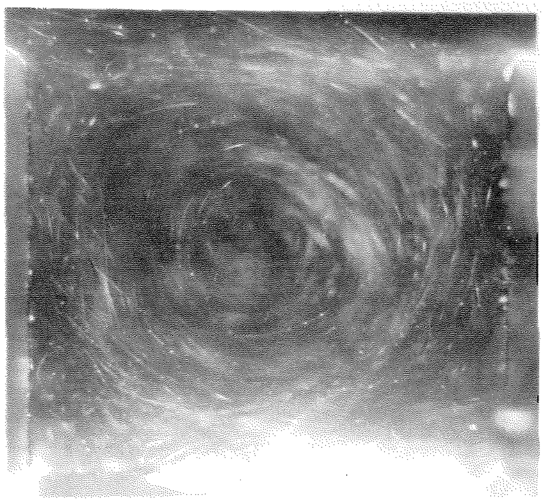

Fig. 15. Photograph typical of those obtainable with aluminum flakes as a visualization medium.

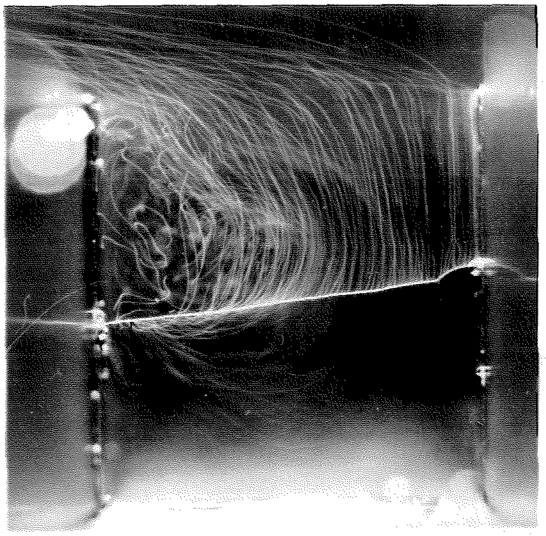

Fig. 16. Photograph using the hydrogen bubble method, showing the noticeable rise rate of the bubbles.

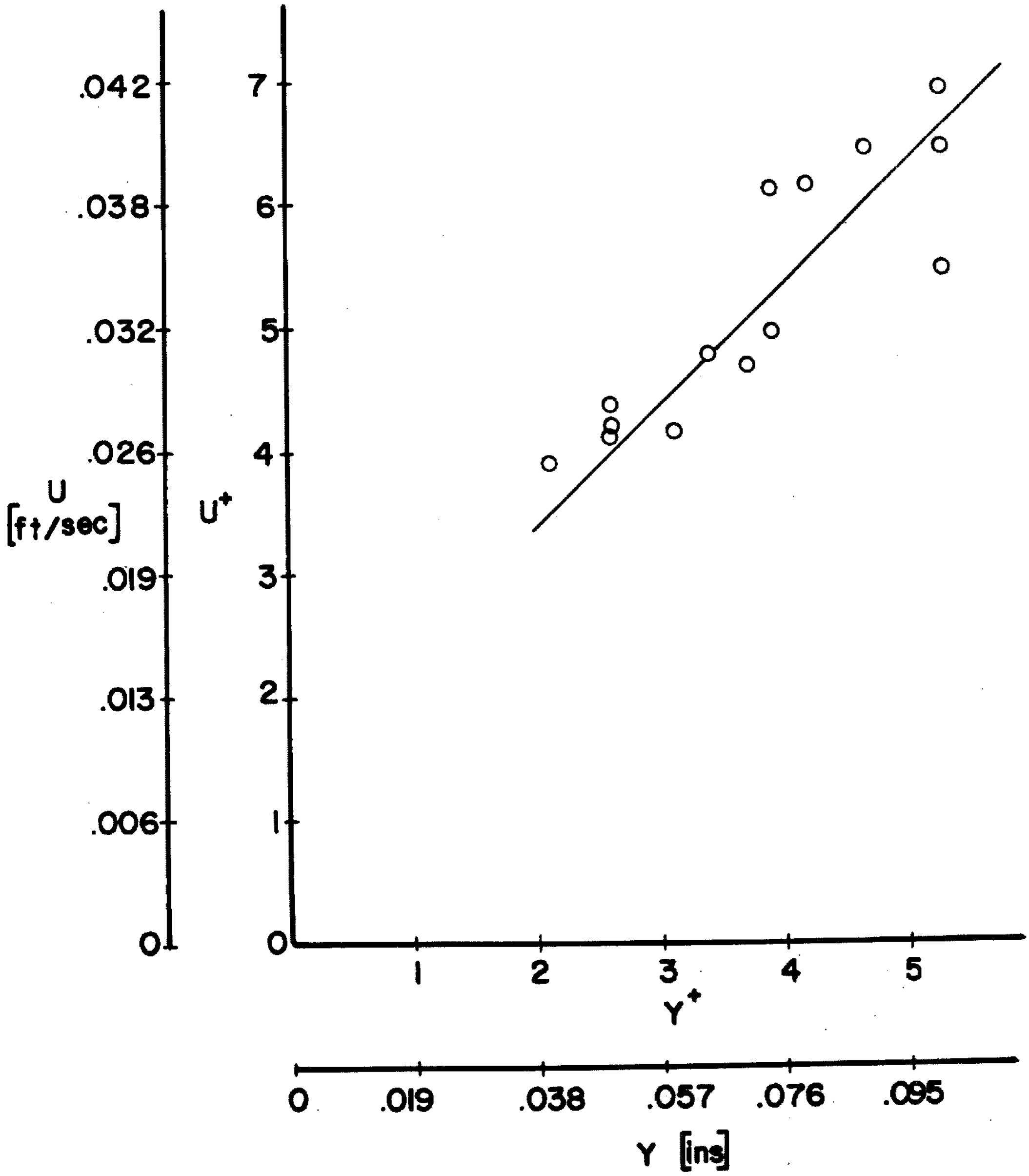

Fig. 17. Mean velocity data near the wall 0.5 ft upstream of the cavity section. $U_\infty = 0.129$ ft/sec. Hot film probe 0.006 ins. dia.

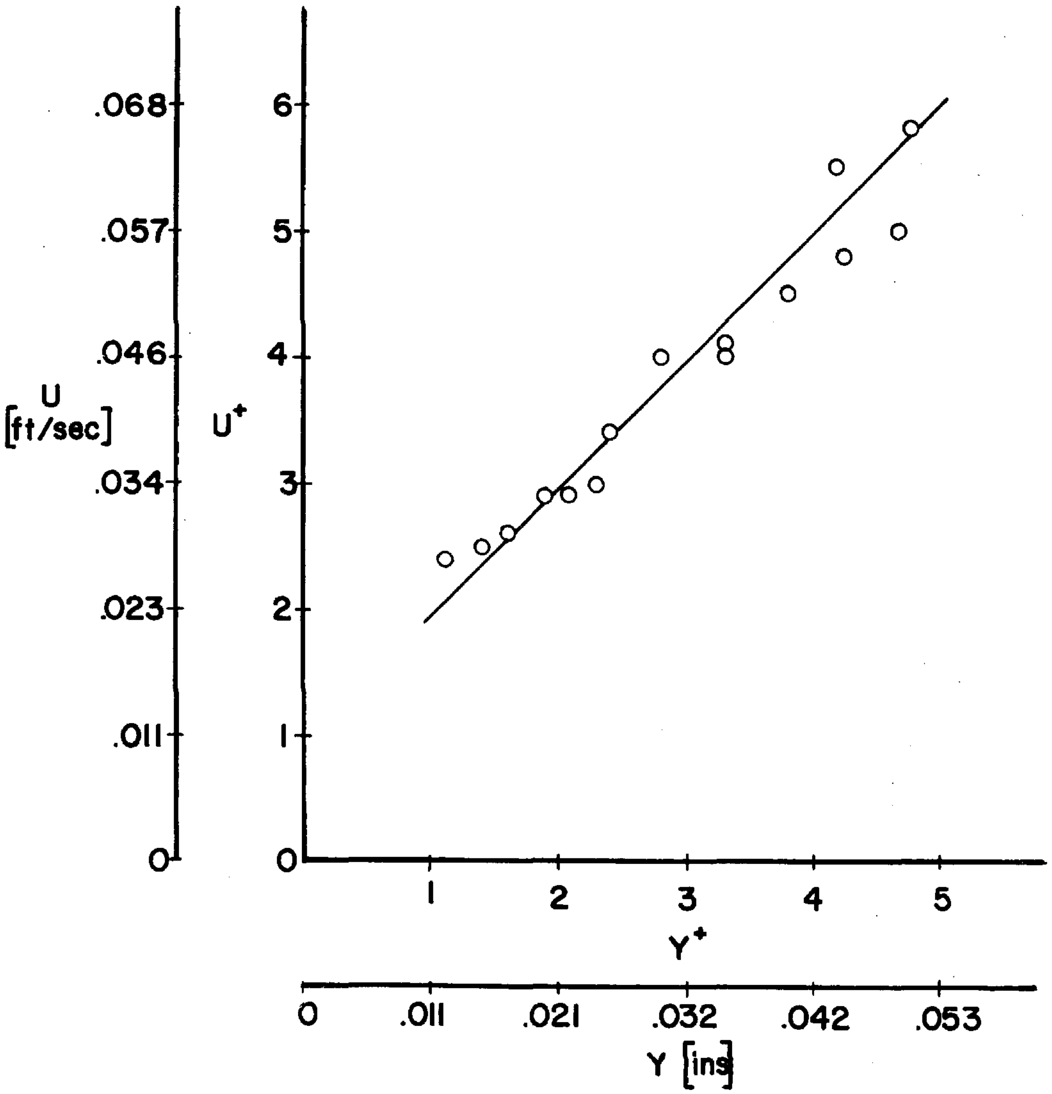

Fig. 18. Mean velocity data near the wall 0.5 ft upstream of the cavity section. U_∞ = 0.254 ft/sec. Hot film probe 0.001 ins. dia.

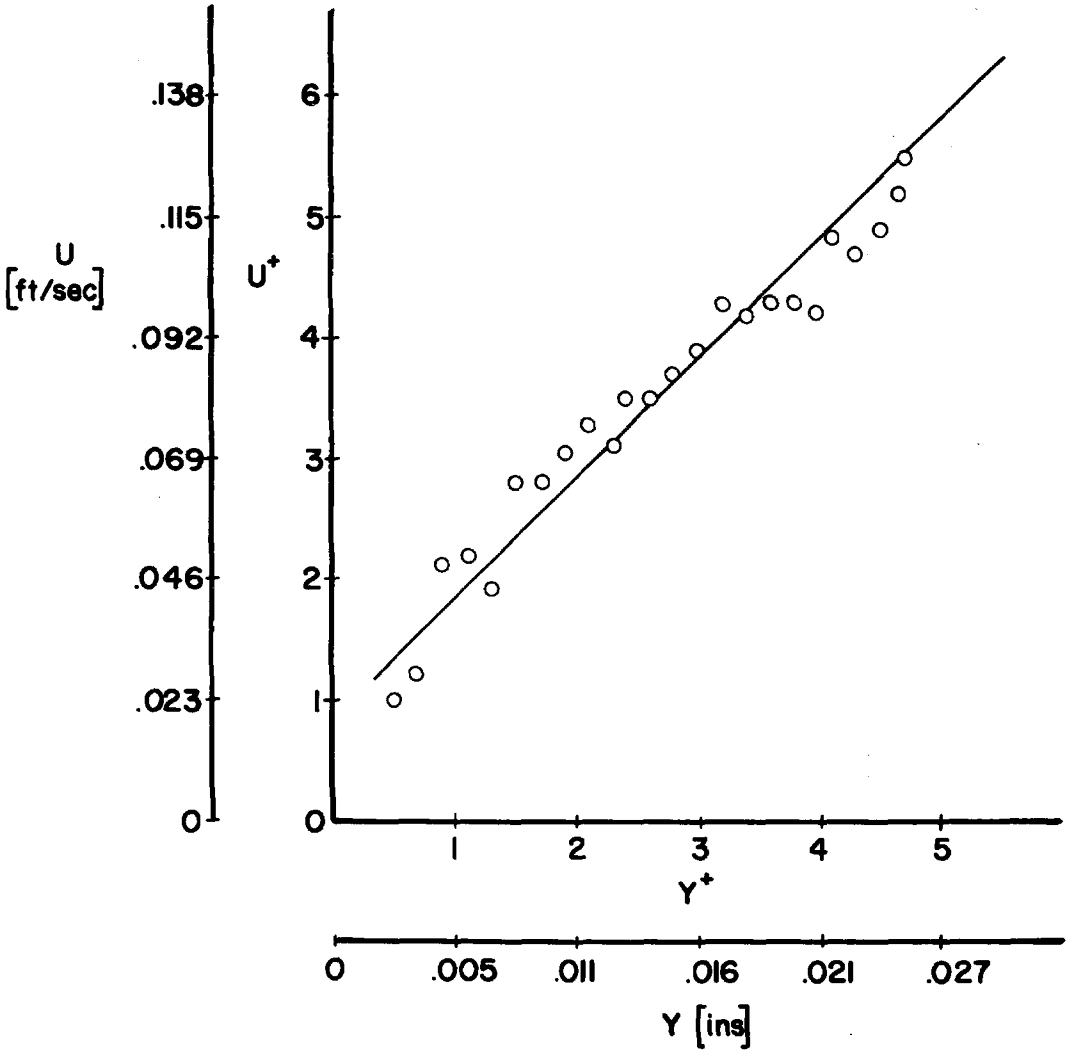

Fig. 19. Mean velocity data near the wall 0.5 ft upstream of the cavity section. U_{∞} - 0.498 ft/sec. Hot film probe 0.001 ins. dia.

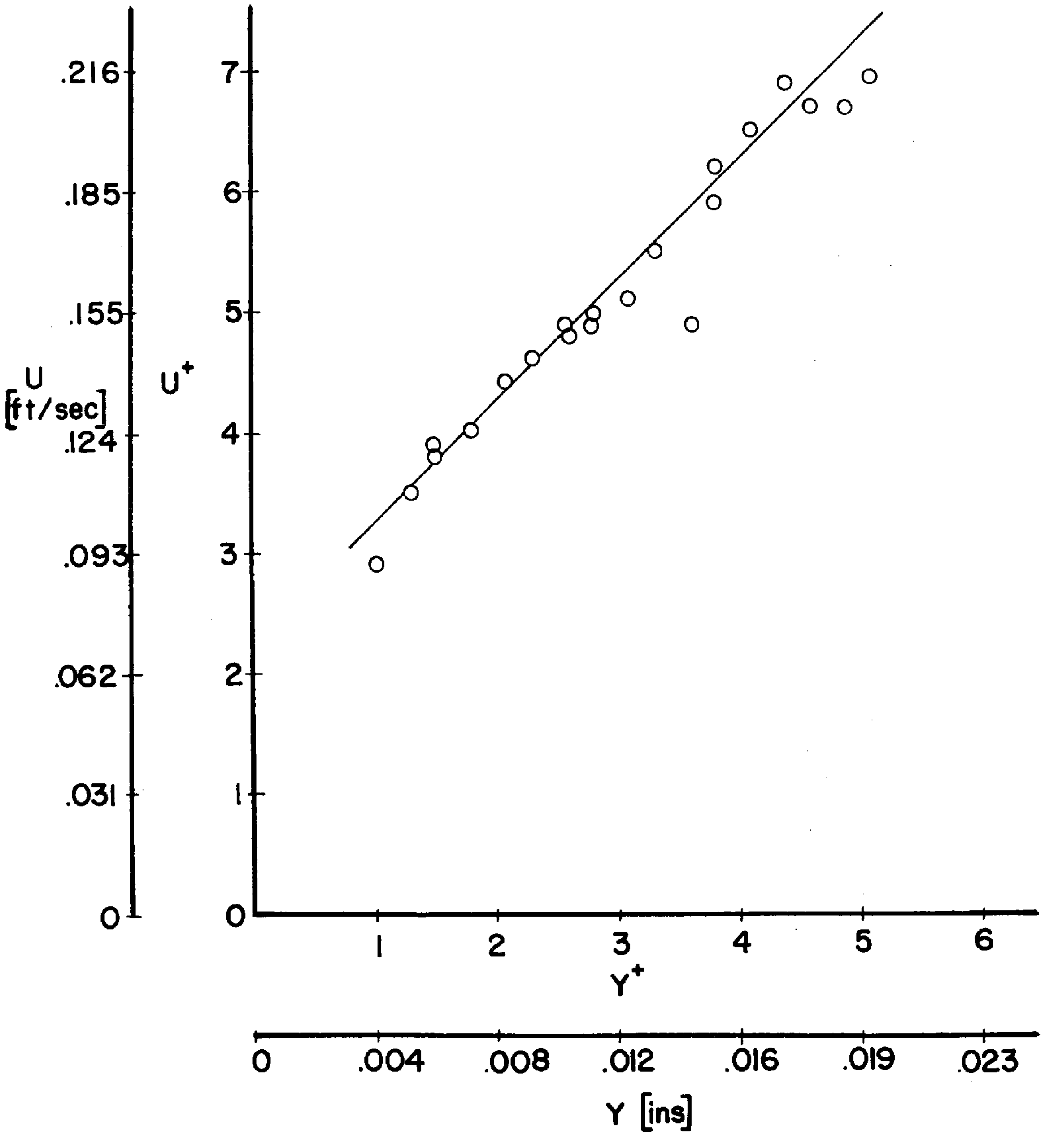

Fig. 20. Mean velocity data near the wall 0.5 ft upstream of the cavity section. $U_{\infty} = 0.769$ ft/sec. Hot film probe 0.001 ins. dia.

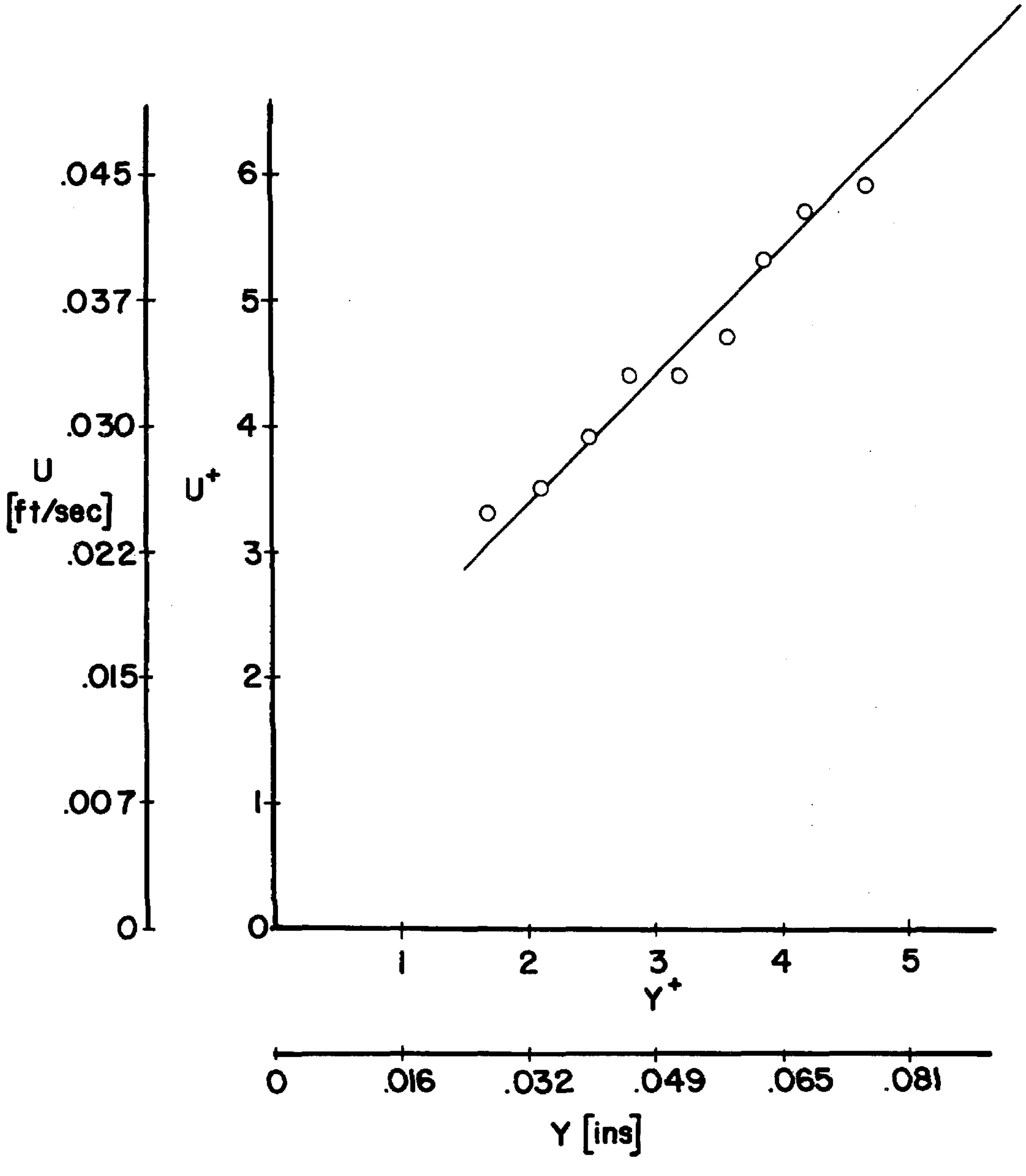

Fig. 21. Mean velocity data near the wall 0.5 ft upstream of the cavity section and 5 ins. off the channel centerline. U_∞ = 0.129 ft/sec. Hot film probe 0.006 ins. dia.

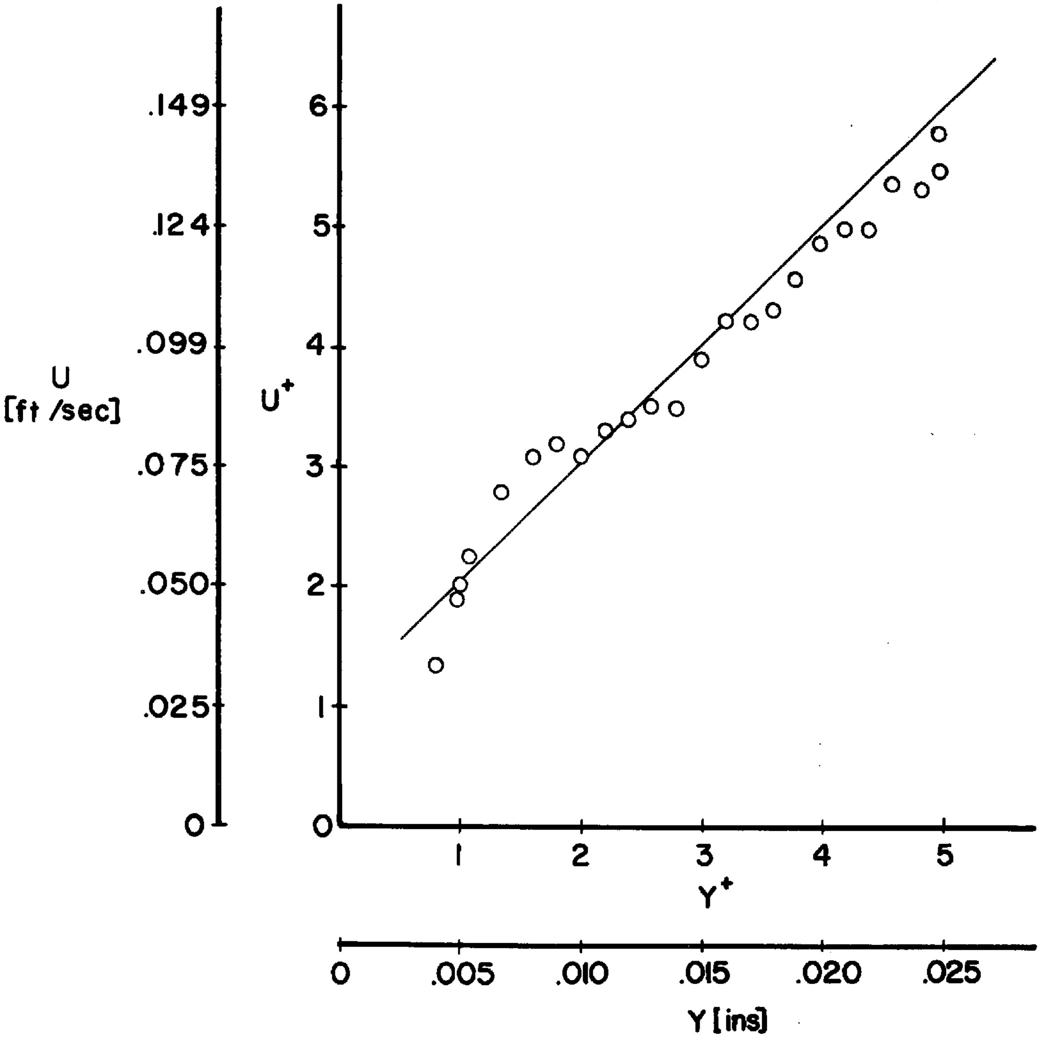

Fig. 22. Mean velocity data near the wall 0.5 ft upstream of the cavity section, 5 ins. off the channel centerline. U_∞ = 0.491 ft/sec. Hot film probe 0.001 ins. dia.

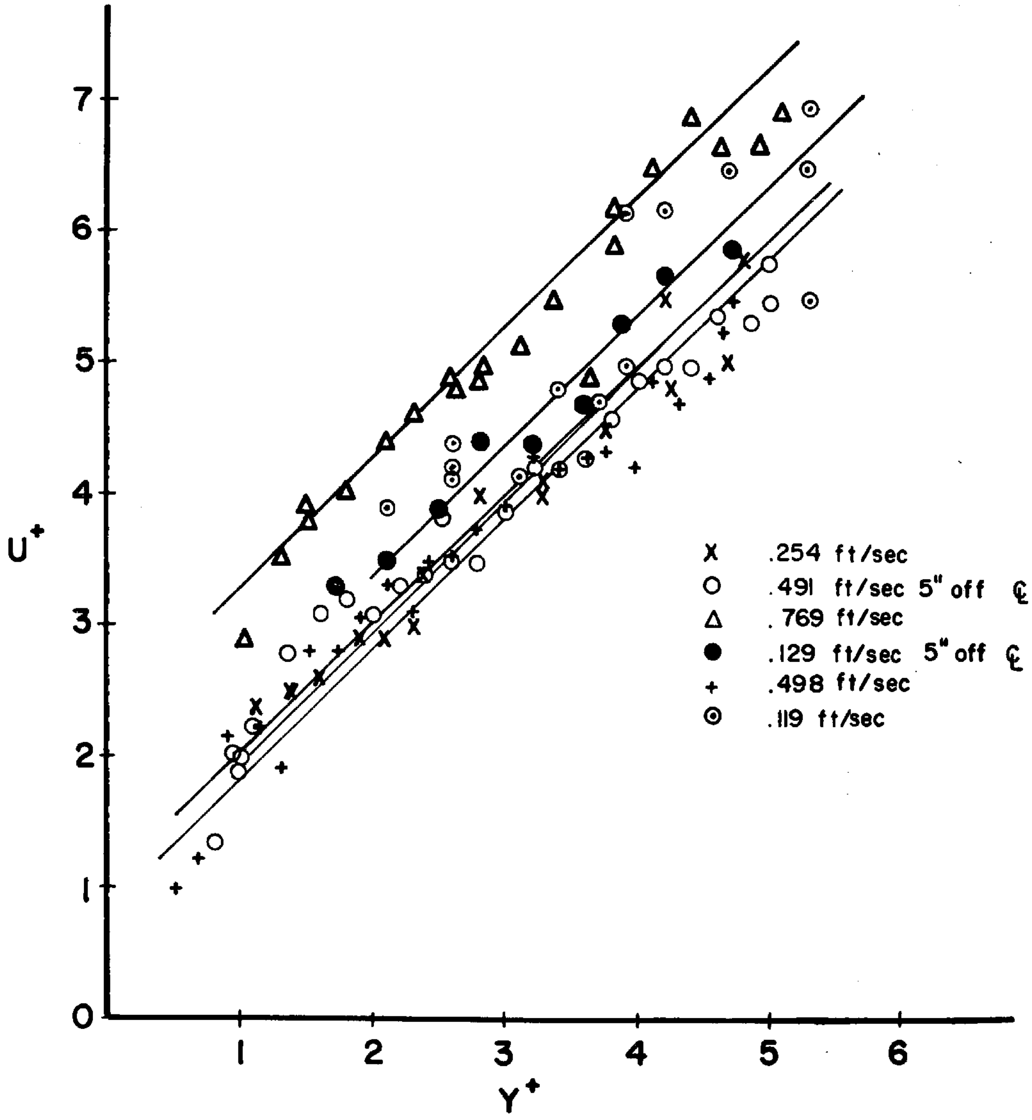

Fig. 23. Mean velocity data near the wall for all free stream velocities.

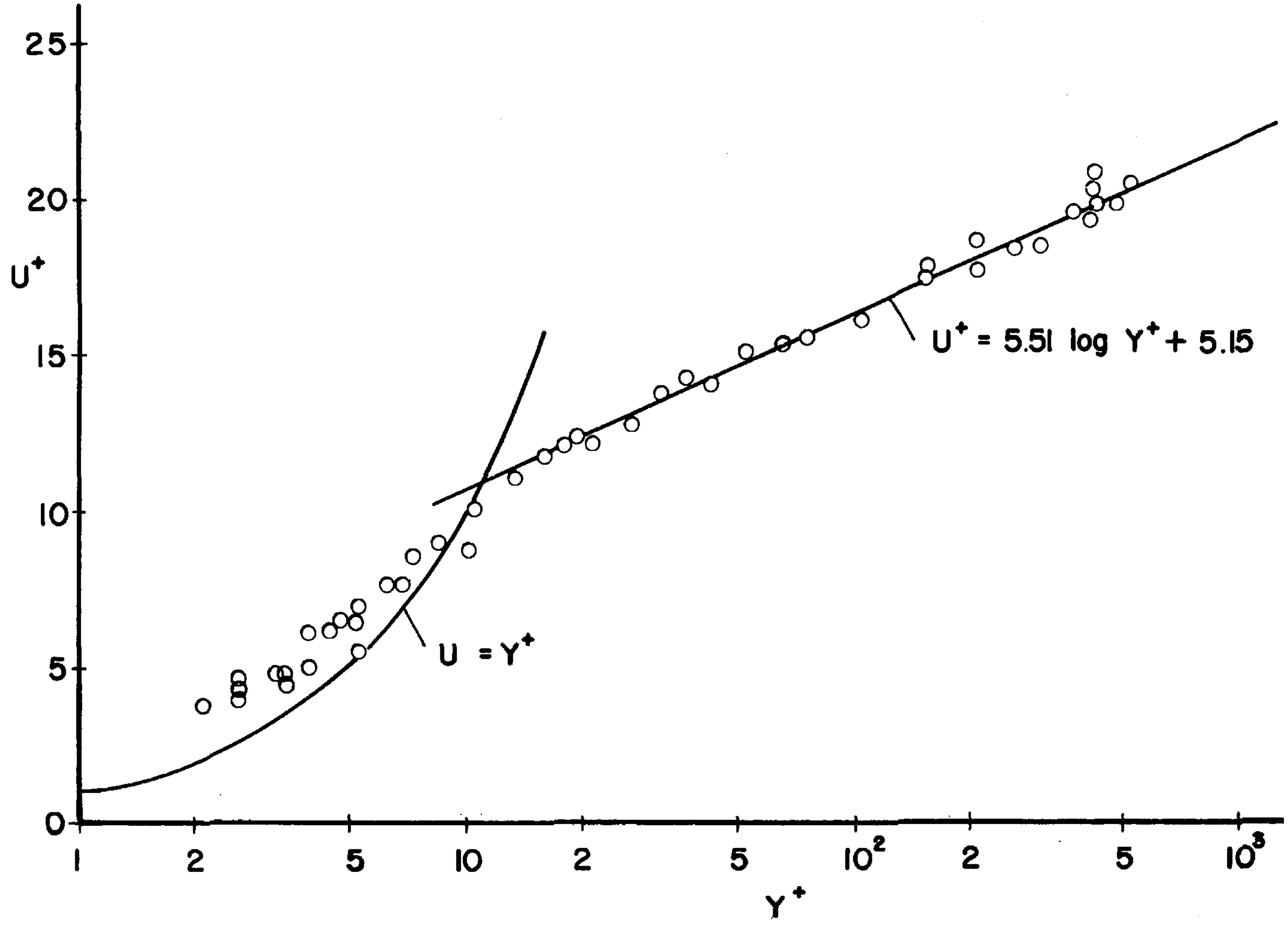

Fig. 24. Mean velocity profile at $U_\infty = 0.119$ ft/sec.

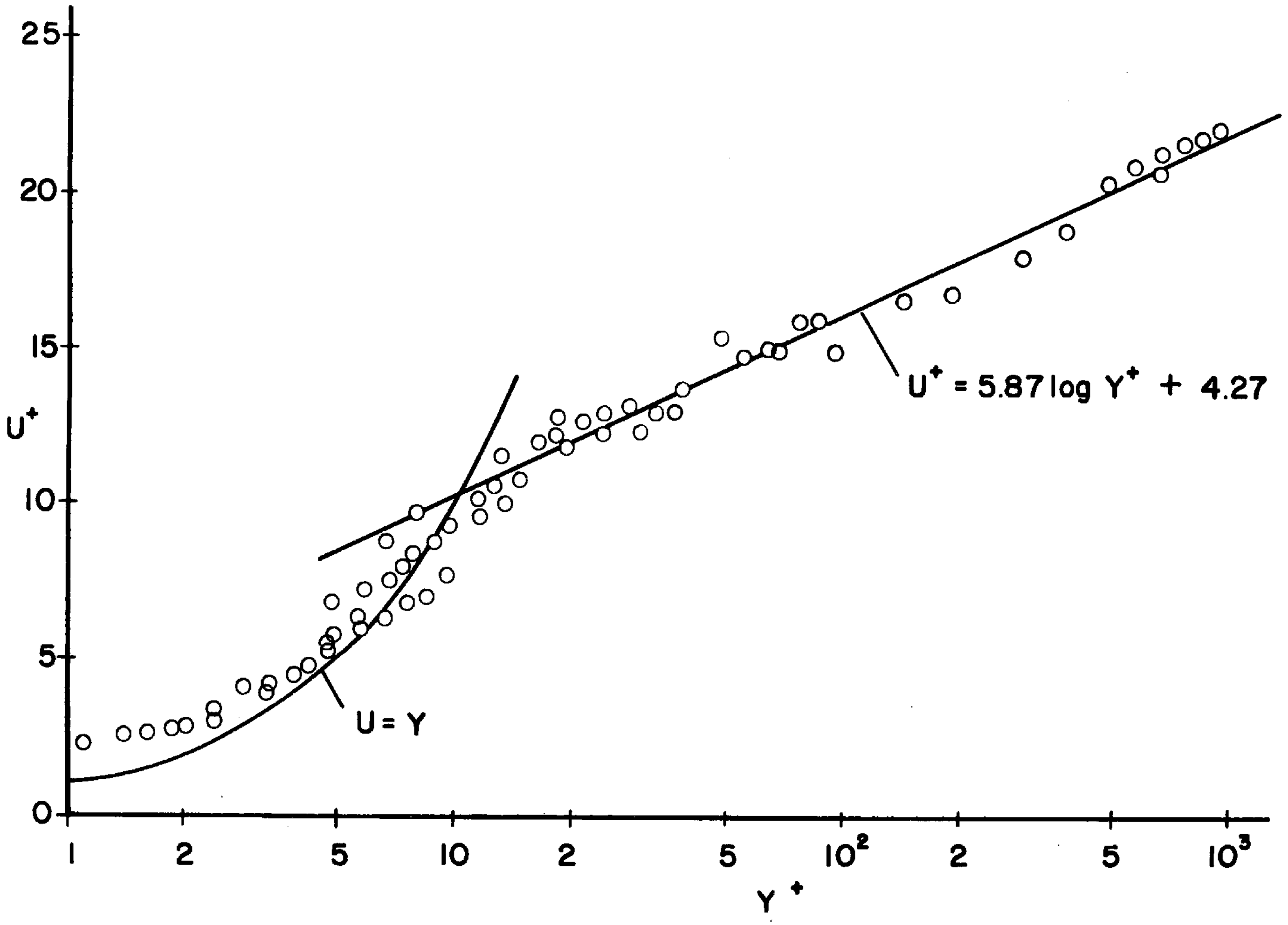

Fig. 25. Mean velocity profile at $U_\infty = 0.254$ ft/sec.

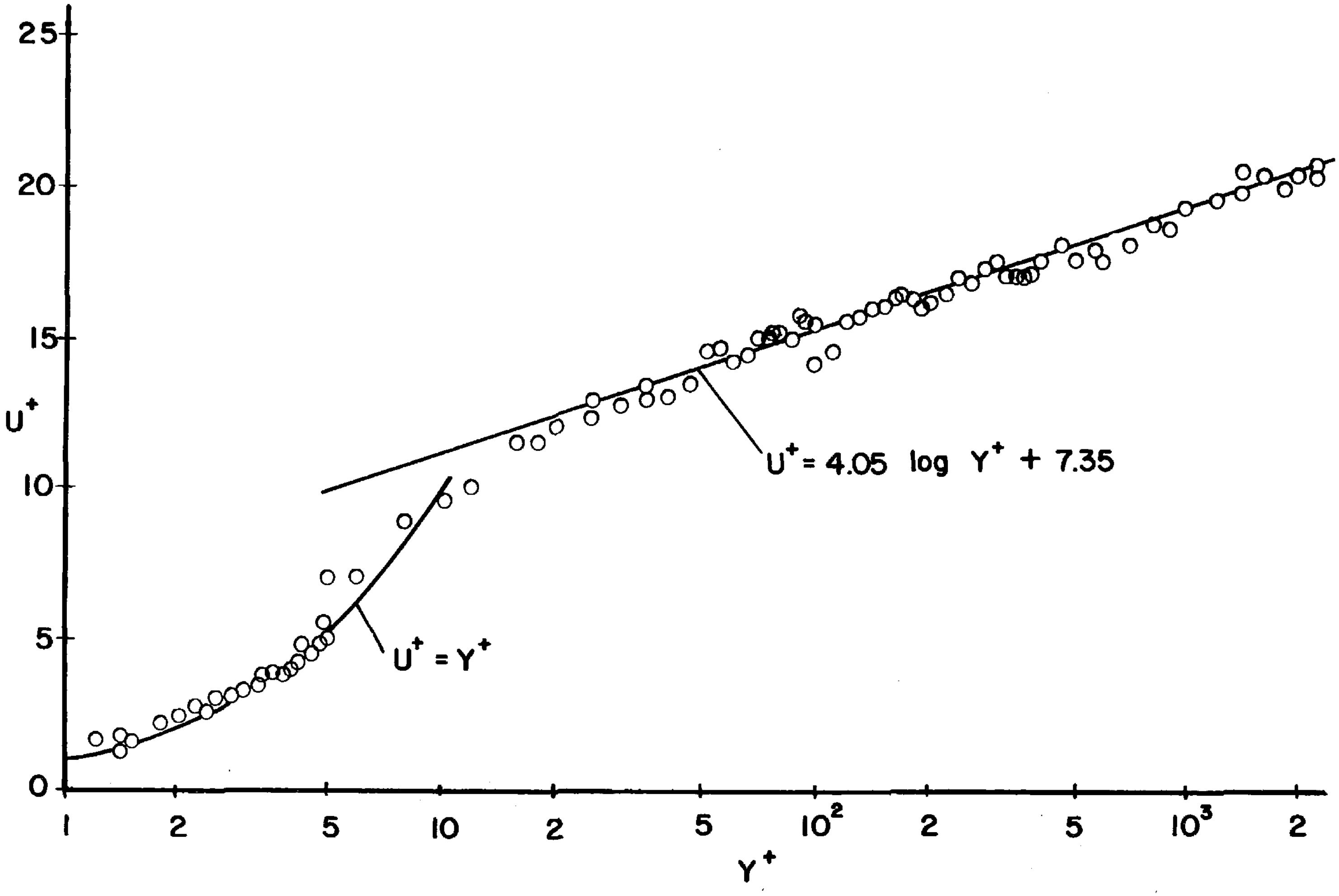

Fig. 26. Mean velocity profile at U_∞ - 0.498 ft/sec.

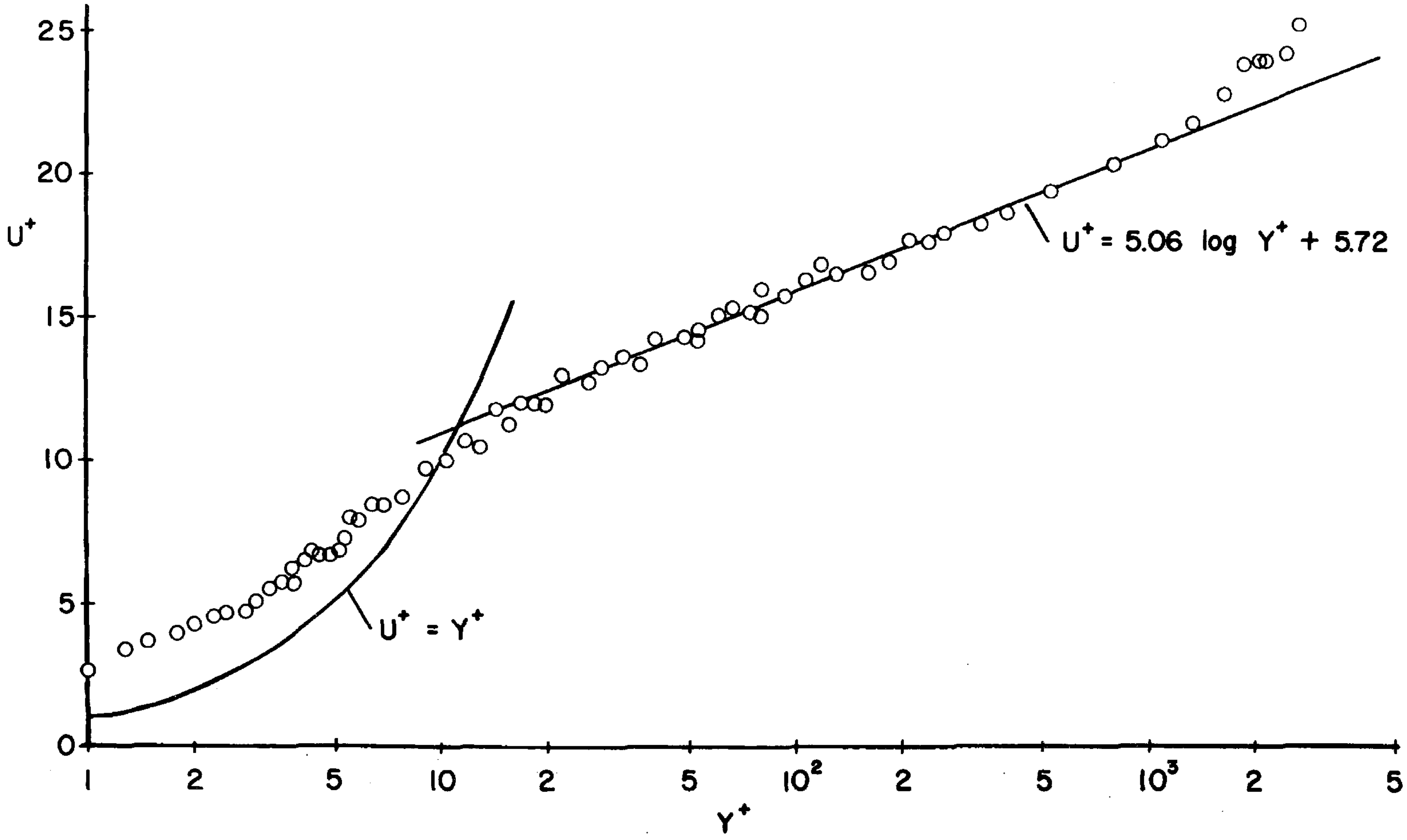

Fig. 27. Mean velocity profile at $U_\infty = 0.769$ ft/sec.

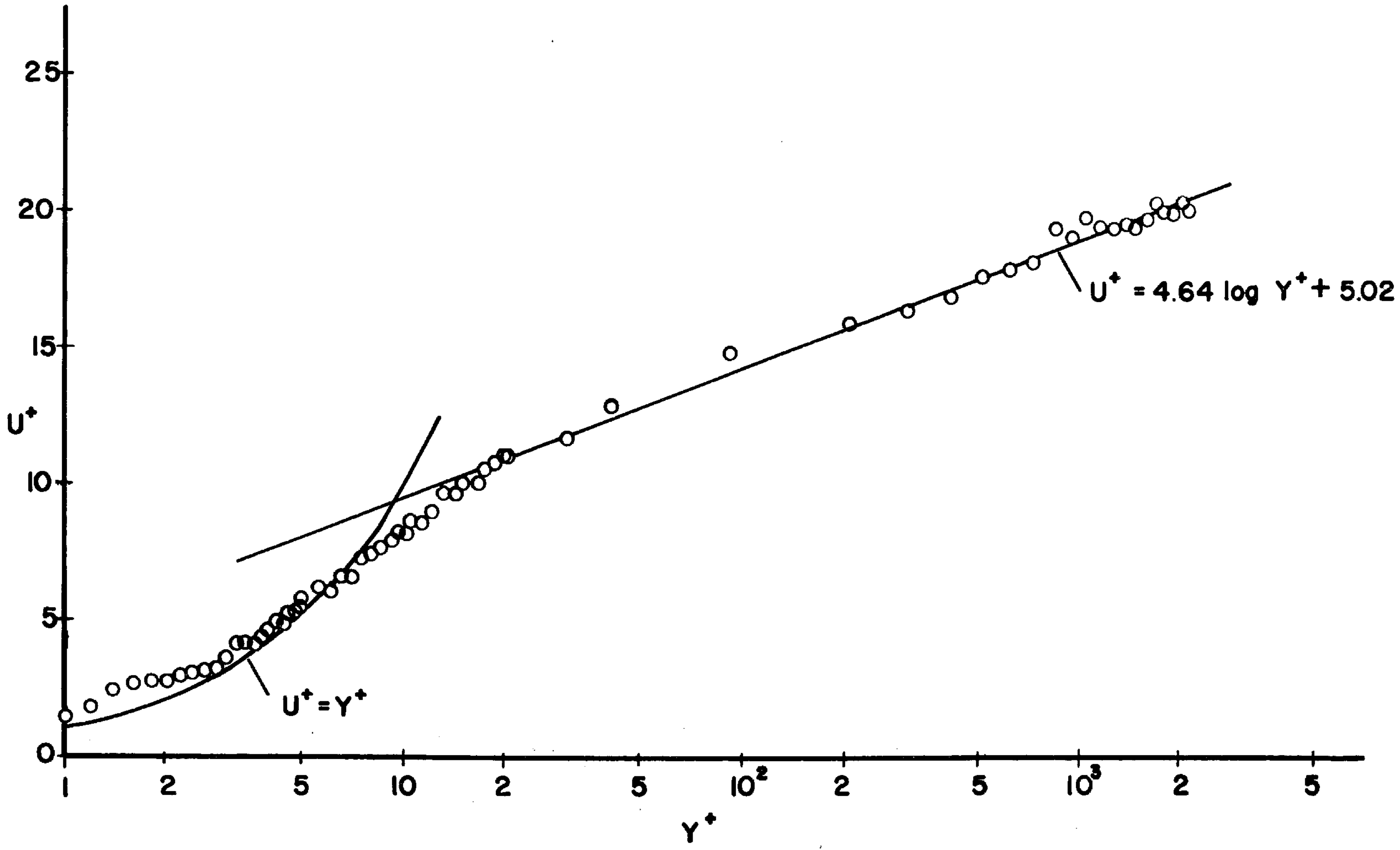

Fig. 28. Mean velocity profile at $U_\infty = 0.491$ ft/sec. 5 ins. off the channel centerline.

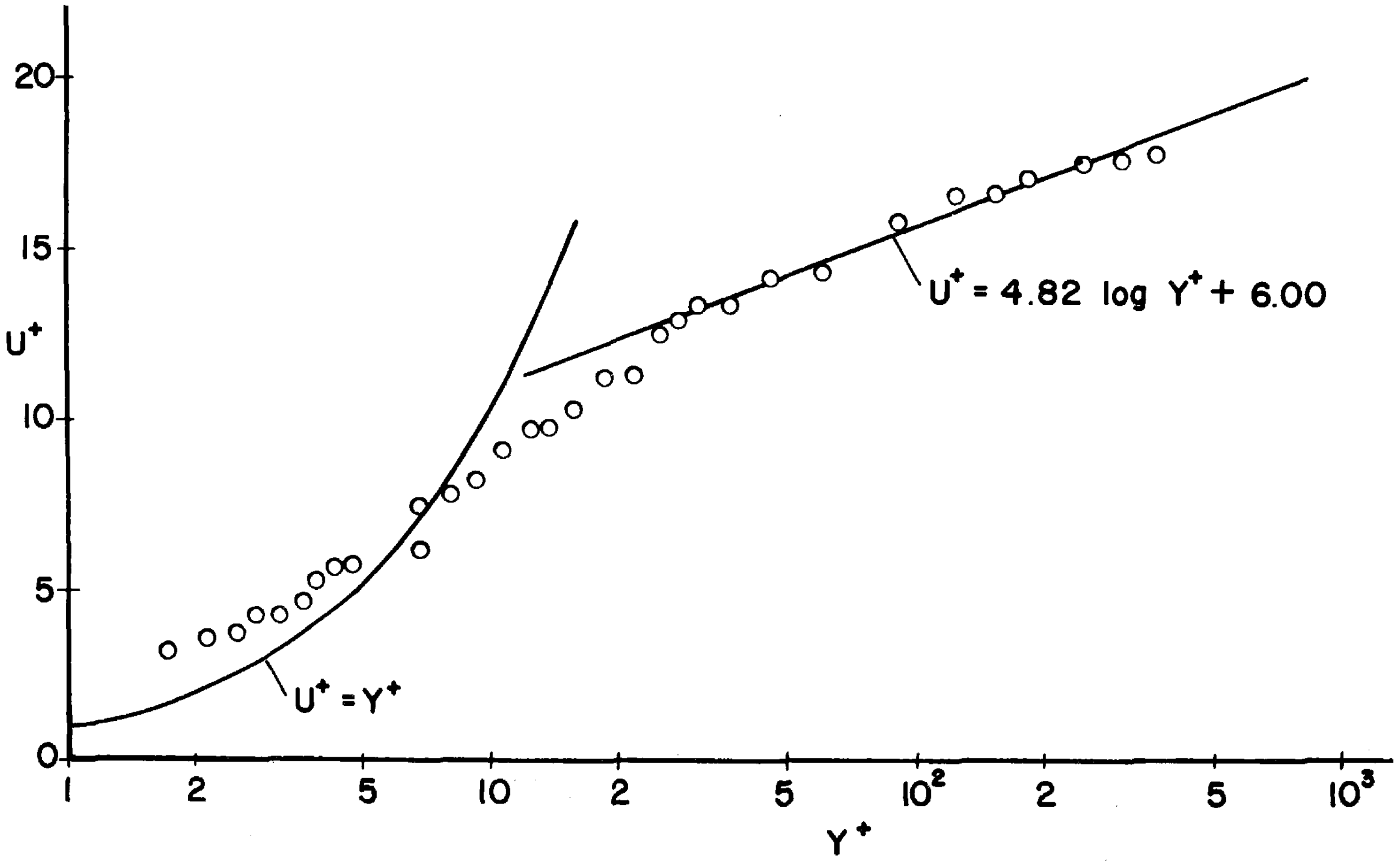

Fig. 29. Mean velocity profile at U_∞ - 0.129 ft/sec. 5 ins. off the channel centerline.

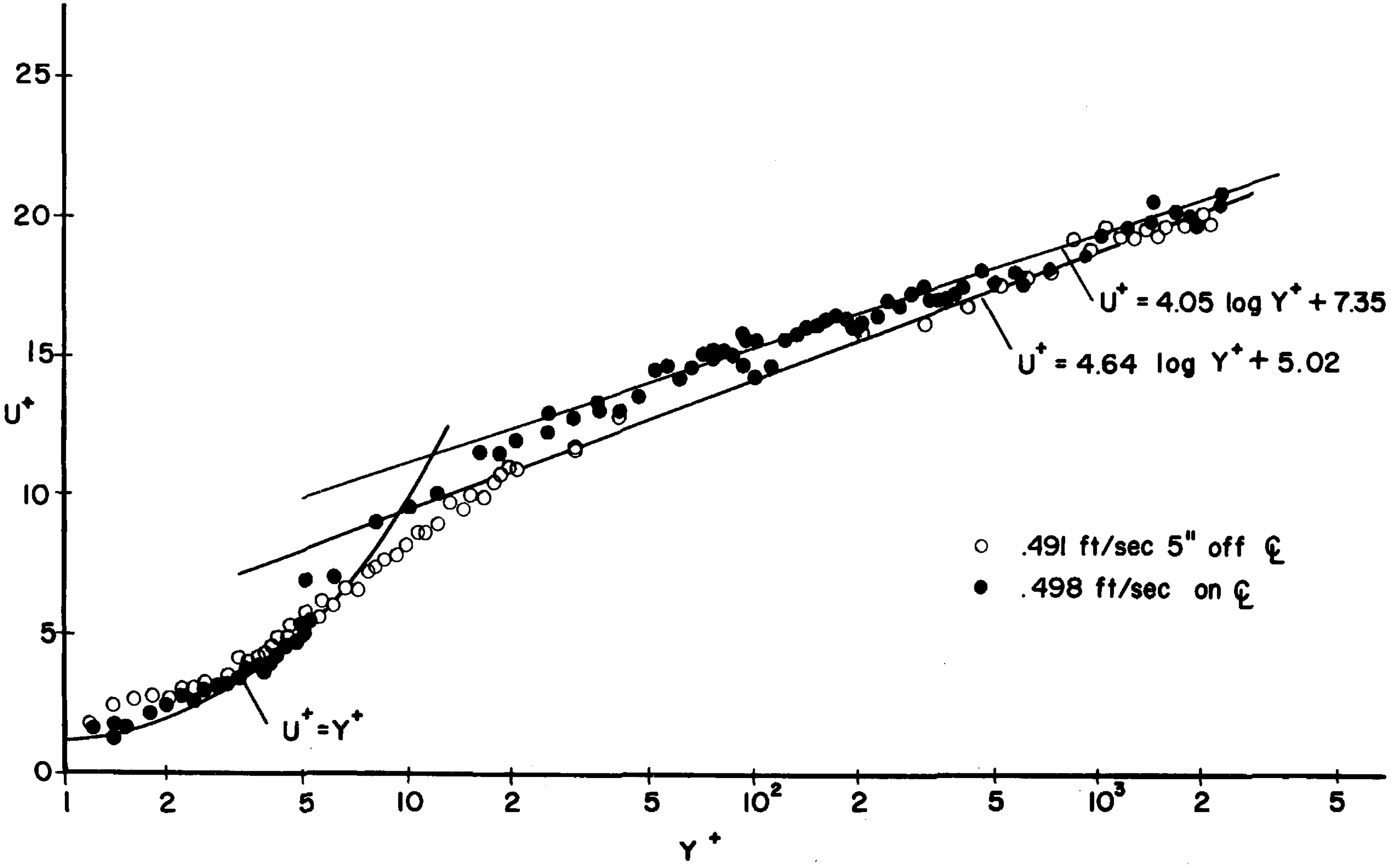

Fig. 30. The centerline velocity profile and that 5 ins. off the centerline at $U_\infty \approx 0.5$ ft/sec.

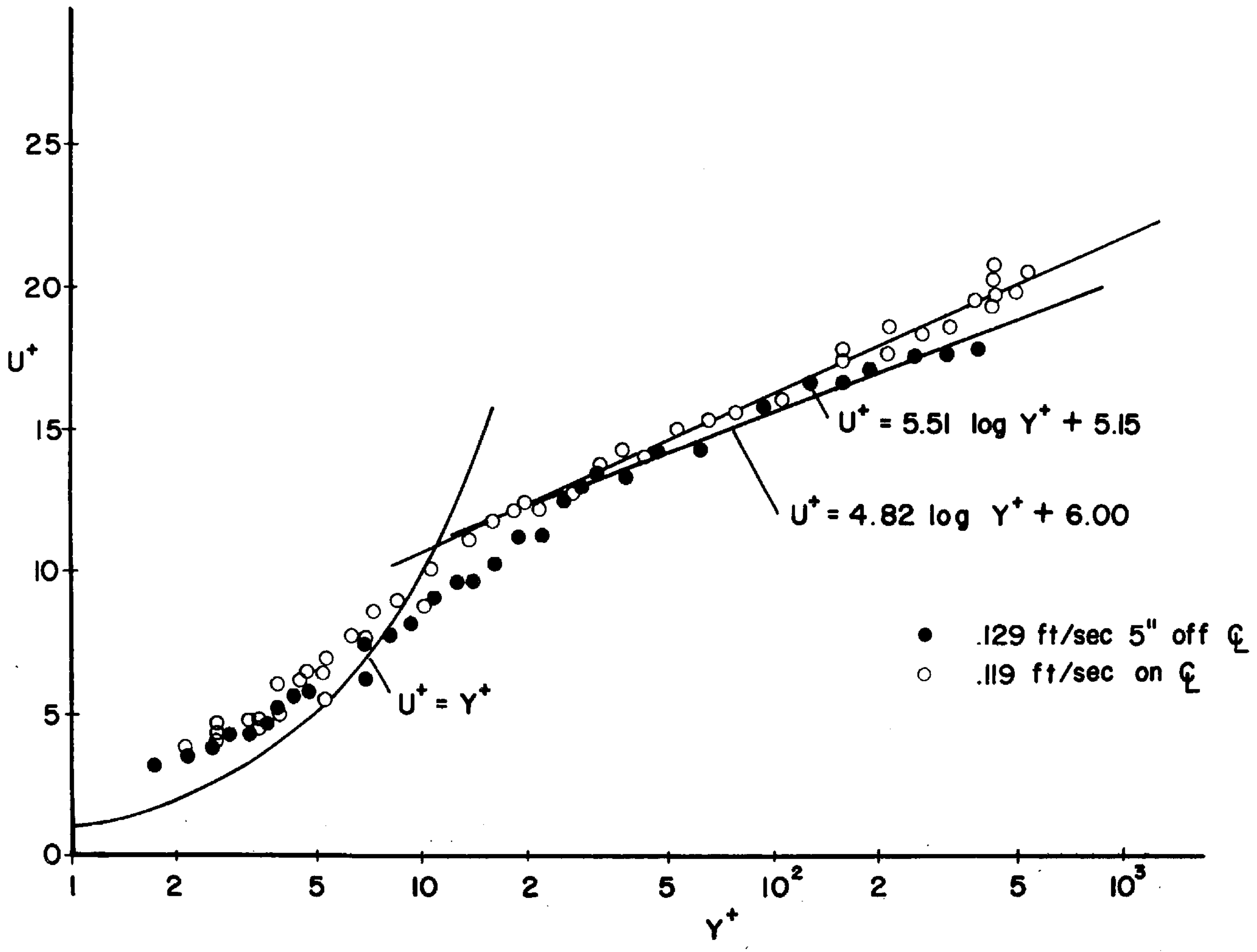

Fig. 31. The centerline velocity profile and that 5 ins. off the centerline at $U_\infty \approx 0.13$ ft/sec.

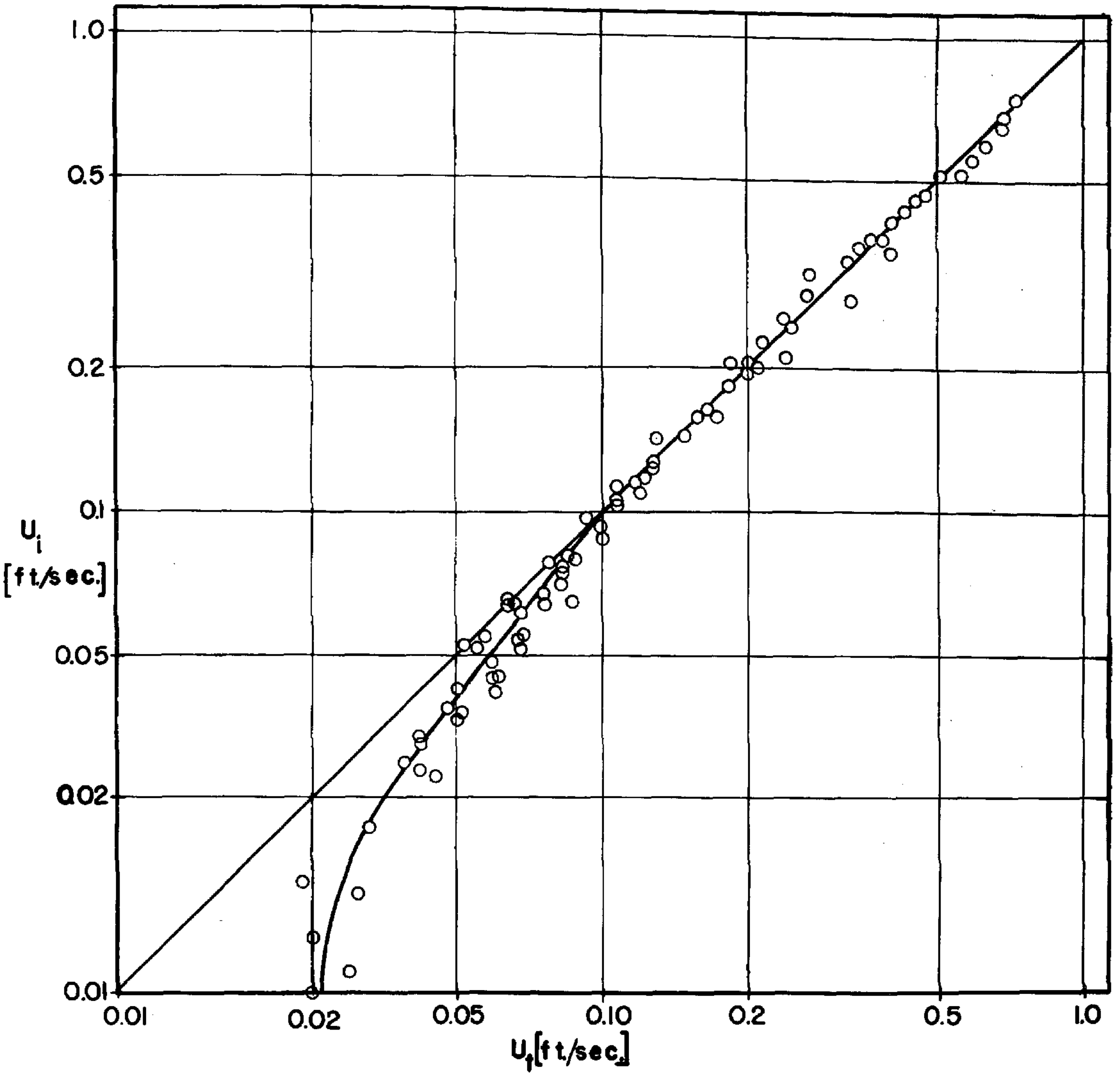

Fig. 32. The hot film anemometer system tow tank calibration curve. U_i = velocity indicated by the anemometer system. U_t = velocity determined by measuring the time for the carriage to traverse a known distance.

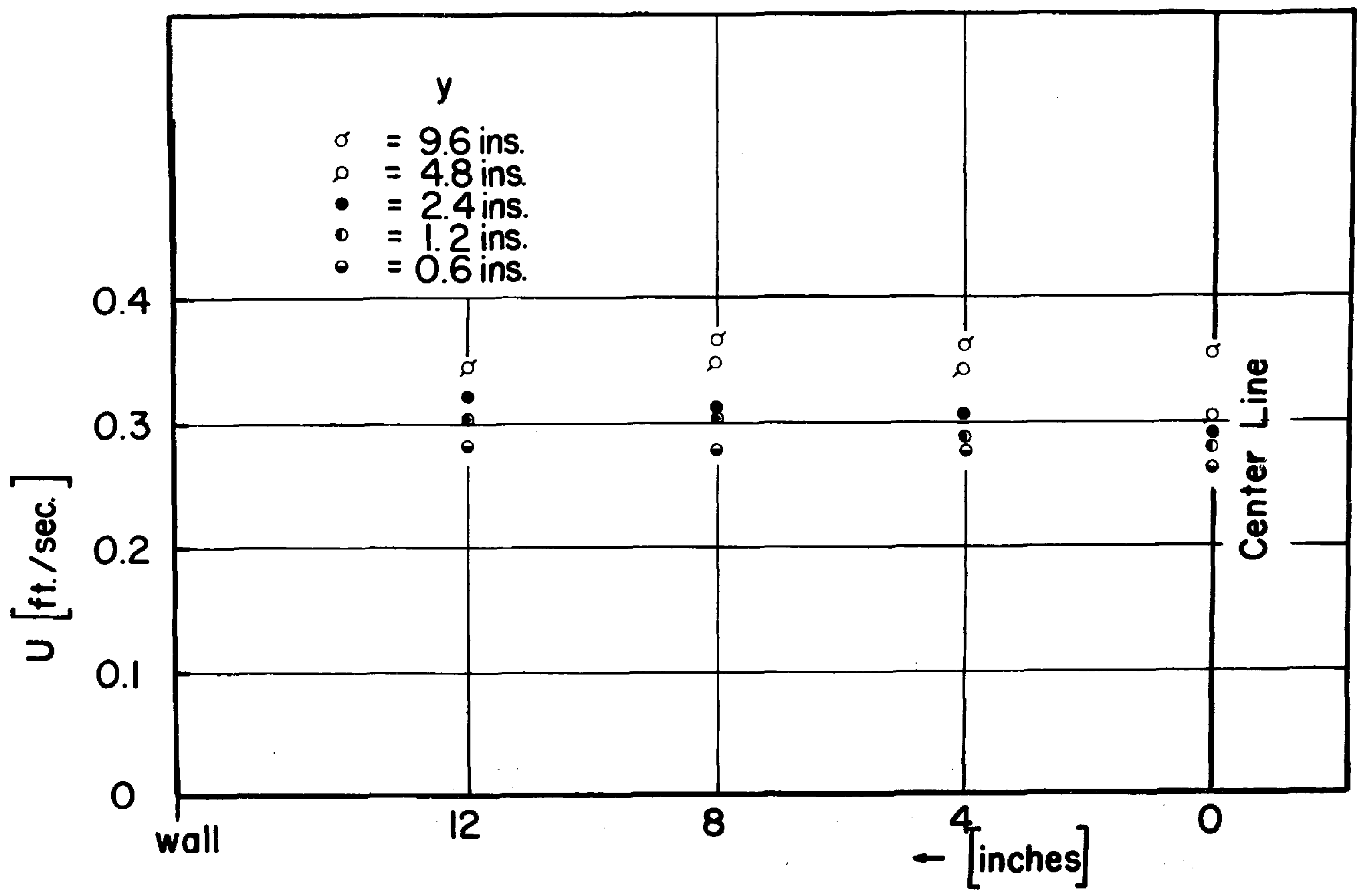

Fig. 33. Survey of mean velocities off the channel centerline at $U_{\infty} = 0.351$ ft/sec.

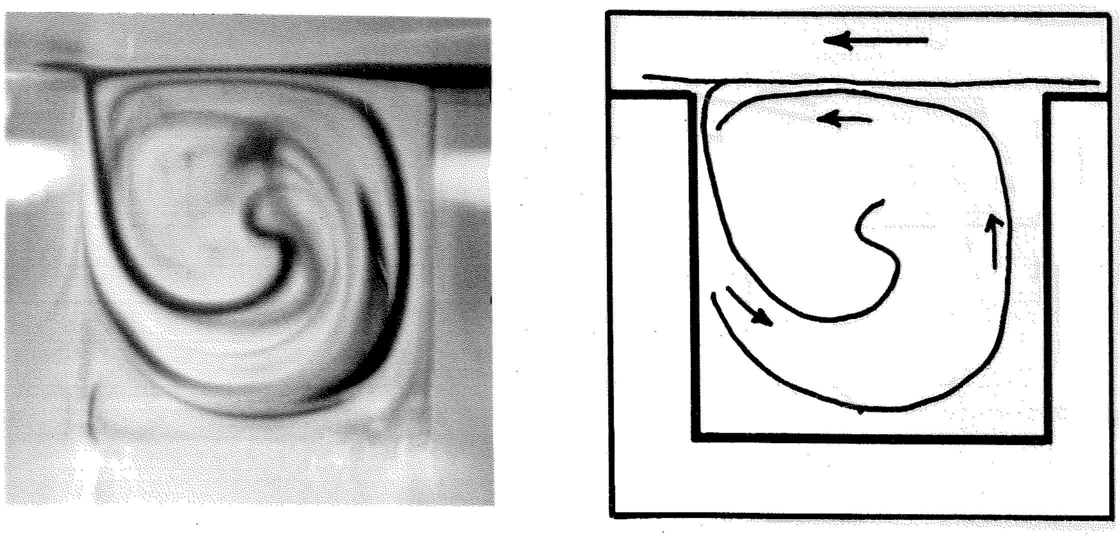

Fig. 34. Photograph and sketch of the "divide" mode of cavity flow.

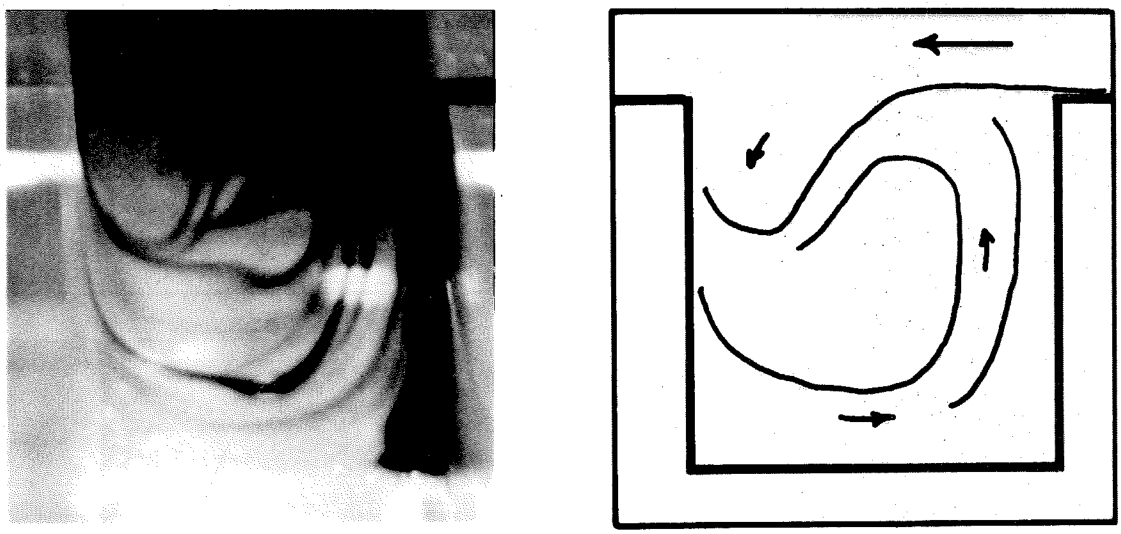

Fig. 35. Photograph and sketch of the "inflow" mode of cavity flow.

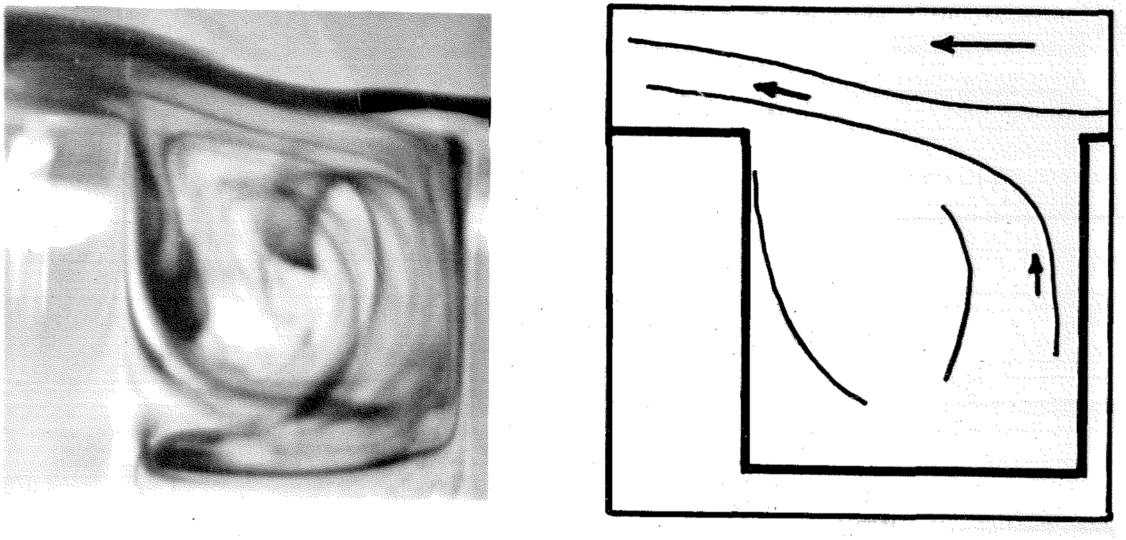

Fig. 36. Photograph and sketch of the "weak exchange" mode of cavity flow.

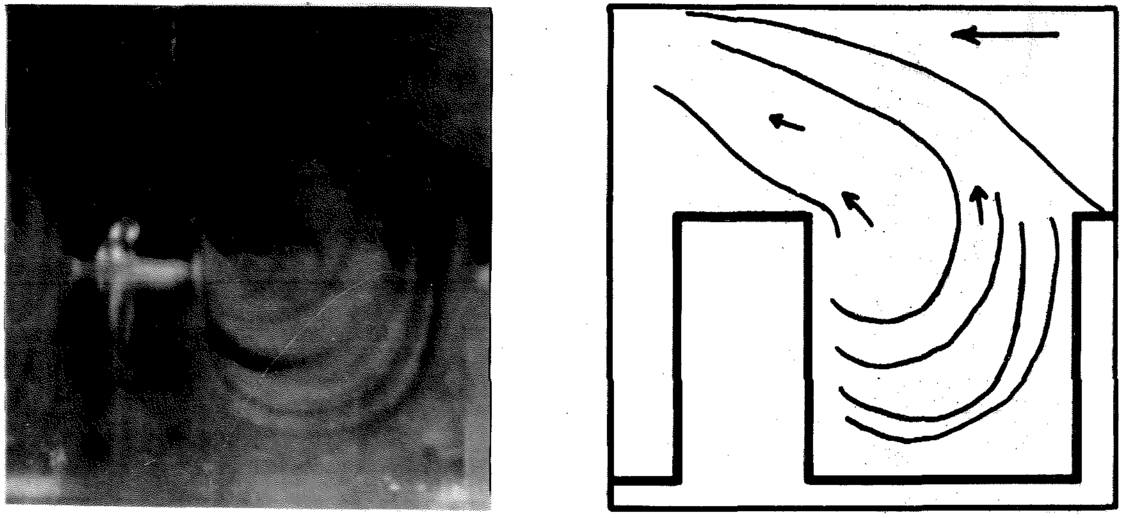

Fig. 37. Photograph and sketch of the "strong exchange" mode of cavity flow.

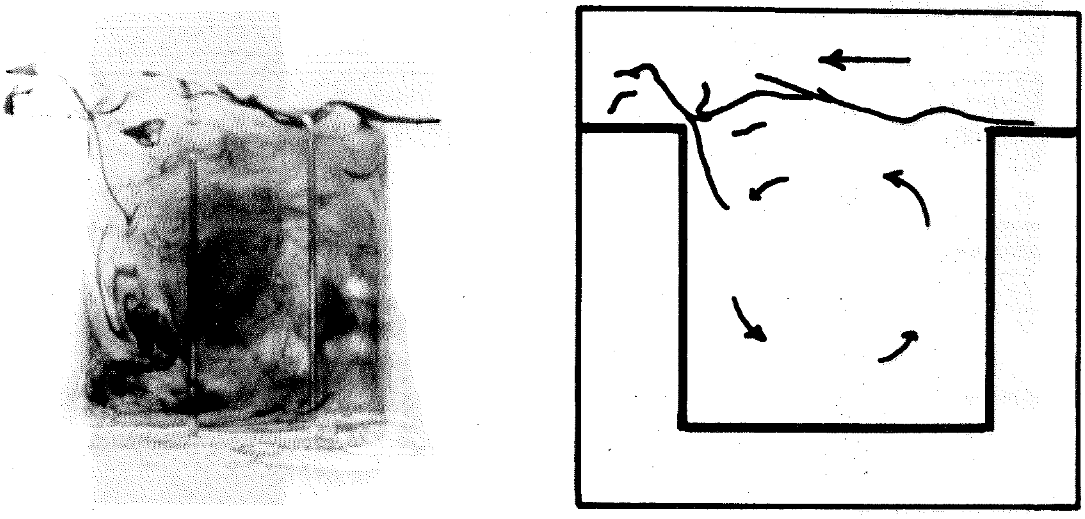

Fig. 38. Photograph and sketch of the "vortex" mode of cavity flow.

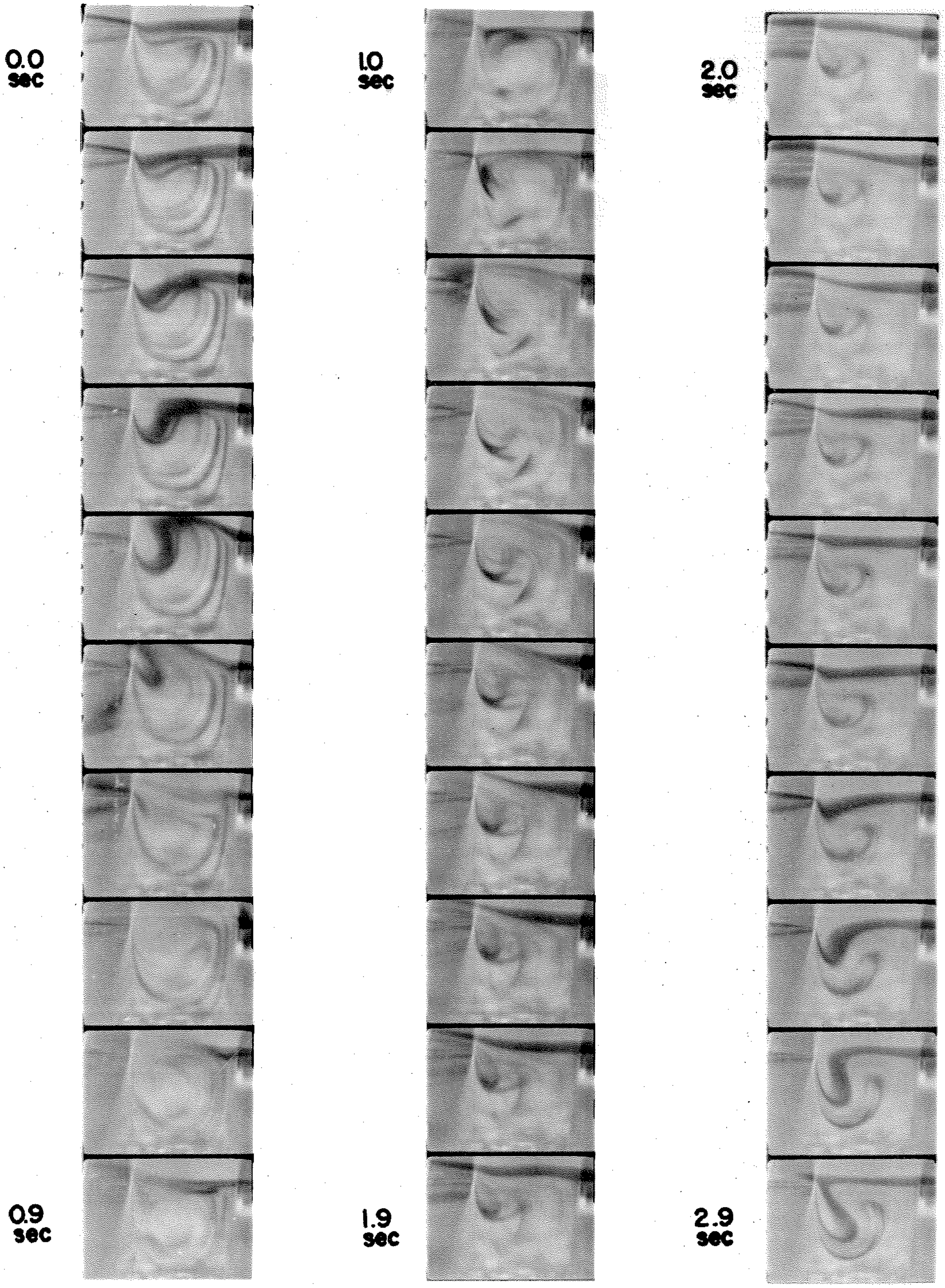

Fig. 39. 16 mm motion picture frames of cavity flow. $\epsilon^* = 24.3$ 1/8 × 1/8 in. cavity, $U_\infty = 0.510$ ft/sec, 10 frames/sec.

Fig. 40. 16 mm motion picture frames of cavity flow. $\epsilon^* = 49.3$, 1/4 × 1/4 in. cavity, $U_\infty = 0.520$ ft/sec. 10 frames/sec.

Fig. 41. 16 mm motion picture frames of cavity flow. $\epsilon^* = 49.3$, $1/4 \times 1/4$ in. cavity, $U_\infty = 0.520$ ft/sec. 10 frames/sec.

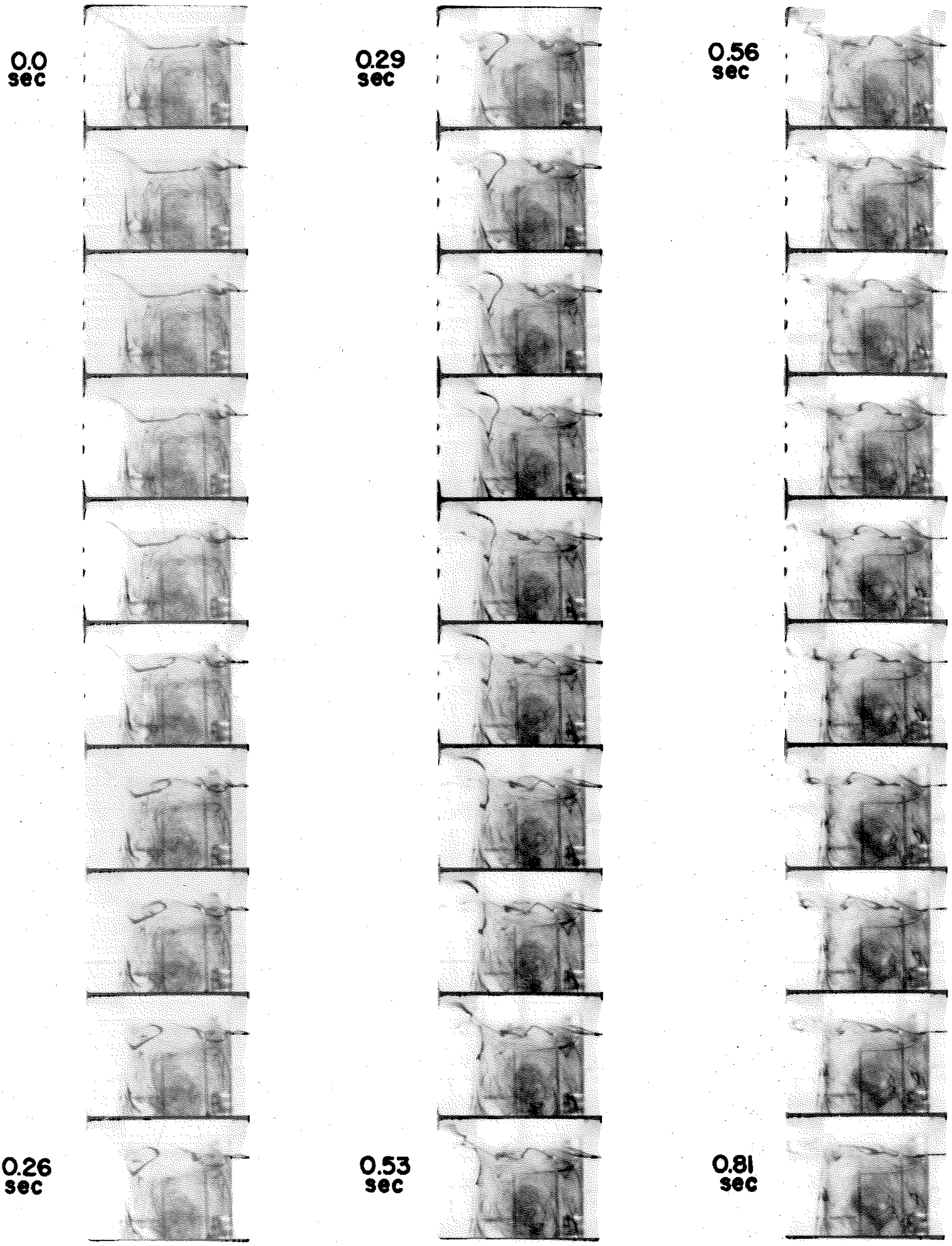

Fig. 42. 16 mm motion picture frames of cavity flow. $\epsilon^* = 201$, 1 × 1 in. cavity, $U_\infty = 0.529$ ft/sec. 35.7 frames/sec.

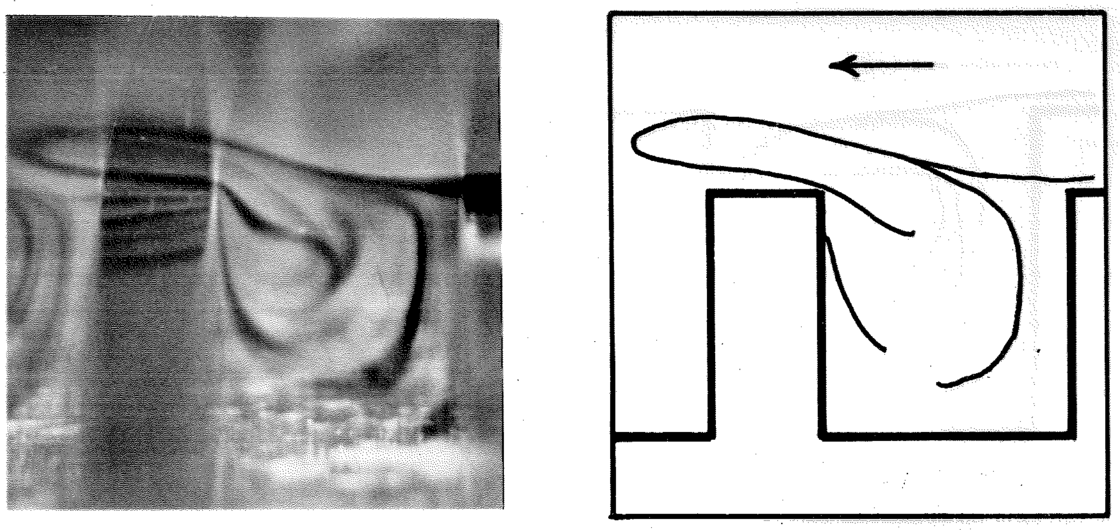

Fig. 43. Cavity weak exchange flow mode at $\epsilon^* = 11.8$, 1/8 × 1/8 in. cavity, $U_\infty = 0.255$ ft/sec.

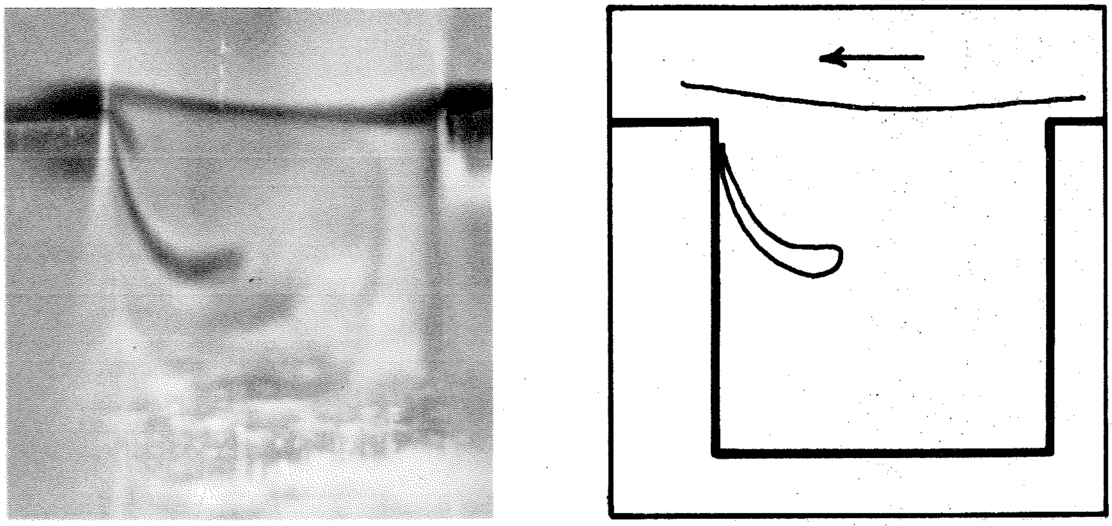

Fig. 44. Cavity divide flow mode at $\epsilon^* = 11.8$, 1/8 × 1/8 in. cavity, $U_\infty = 0.255$ ft/sec.

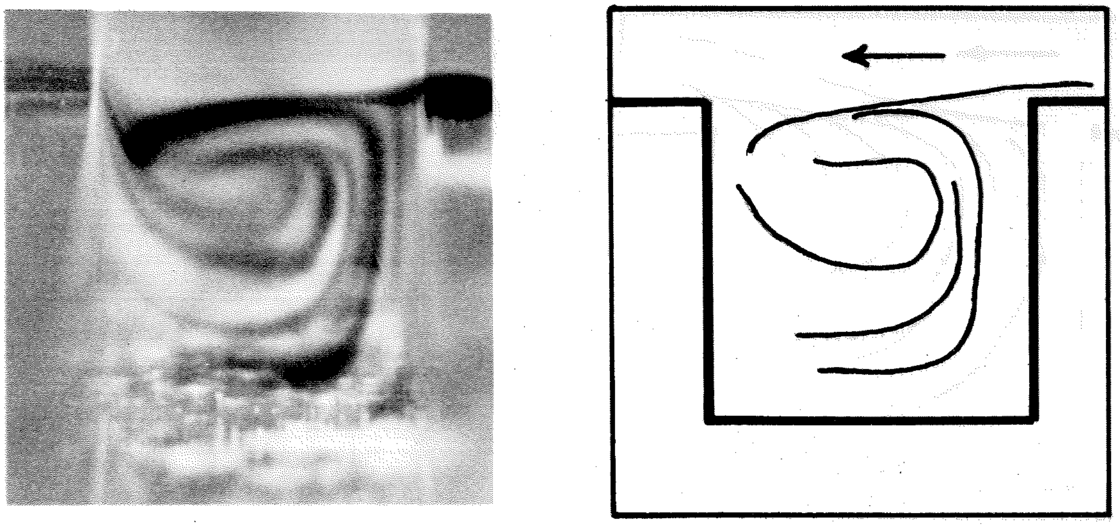

Fig. 45. Cavity inflow flow mode at $\epsilon^* = 11.8$, 1/8 × 1/8 in. cavity, $U_\infty = 0.255$ ft/sec.

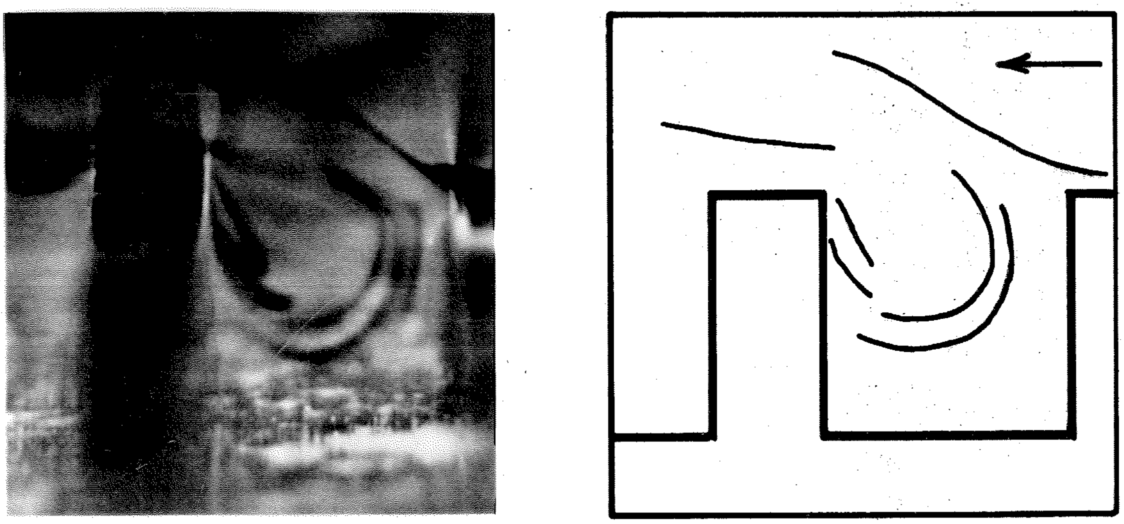

Fig. 46. Cavity strong exchange flow mode at $\epsilon^* = 11.8$, 1/8 × 1/8 in. cavity, $U_\infty = 0.255$ ft/sec.

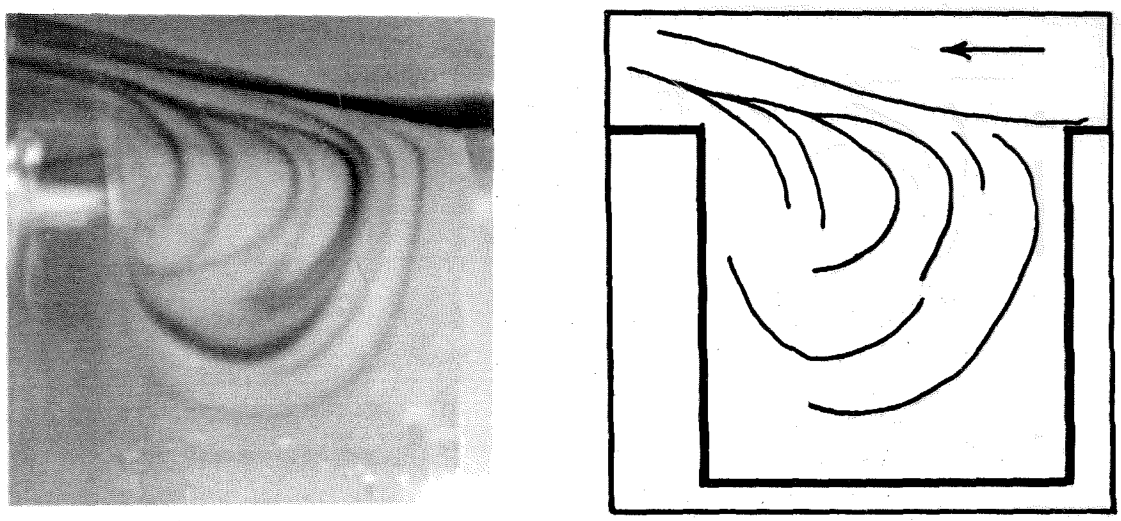

Fig. 47. Cavity weak exchange flow mode at $\epsilon^* = 13.1$, 1/4 × 1/4 in. cavity, $U_\infty = 0.127$ ft/sec.

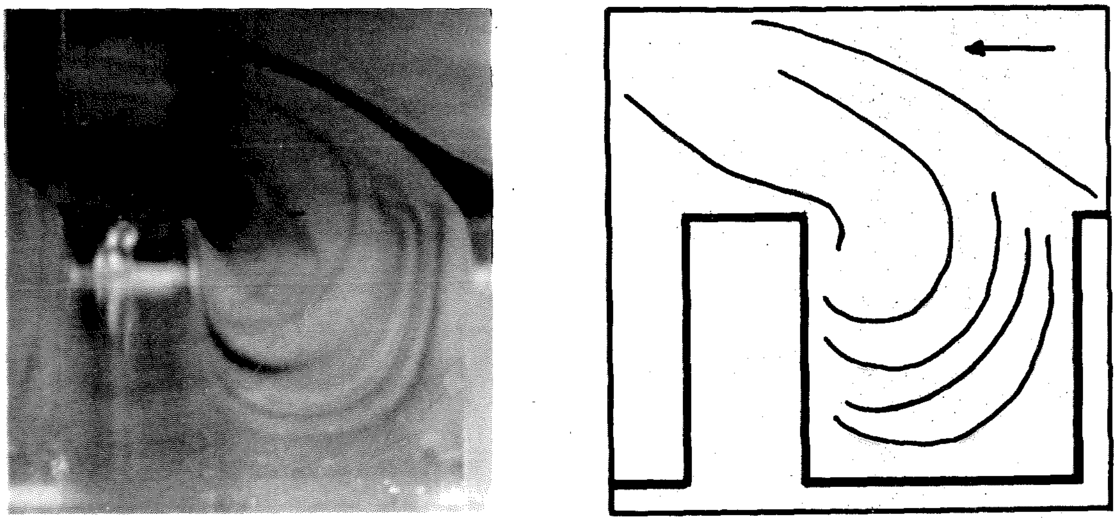

Fig. 48. Cavity strong exchange flow mode at $\epsilon^* = 13.1$, 1/4 × 1/4 in. cavity, $U_\infty = 0.127$ ft/sec.

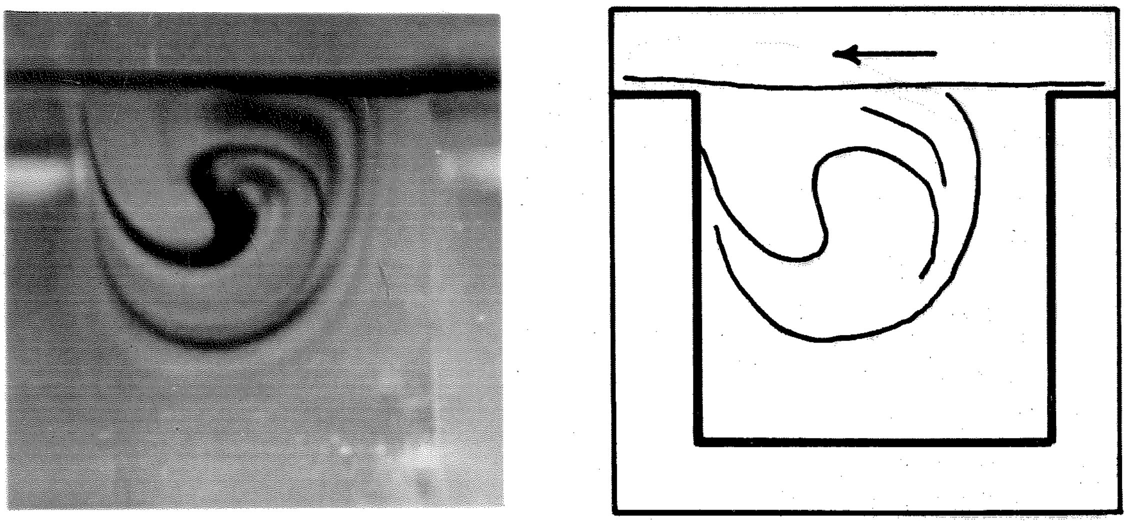

Fig. 49. Cavity divide flow mode at $\epsilon^* = 13.1$, 1/4 × 1/4 in. cavity, $U_\infty = 0.127$ ft/sec.

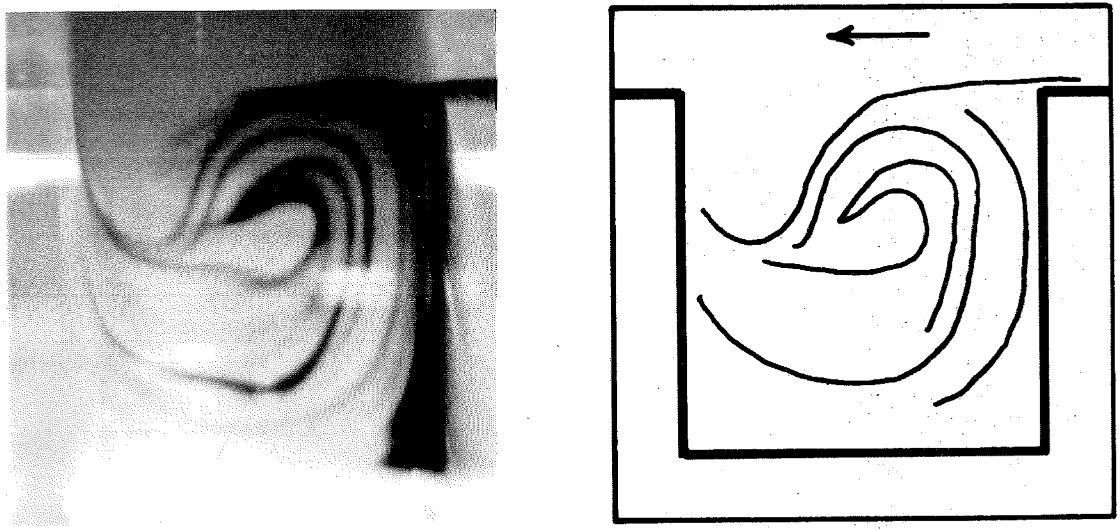

Fig. 50. Cavity inflow flow mode at $\epsilon^* = 22.7$, 1/4 × 1/4 in. cavity, $U_\infty = 0.245$ ft/sec.

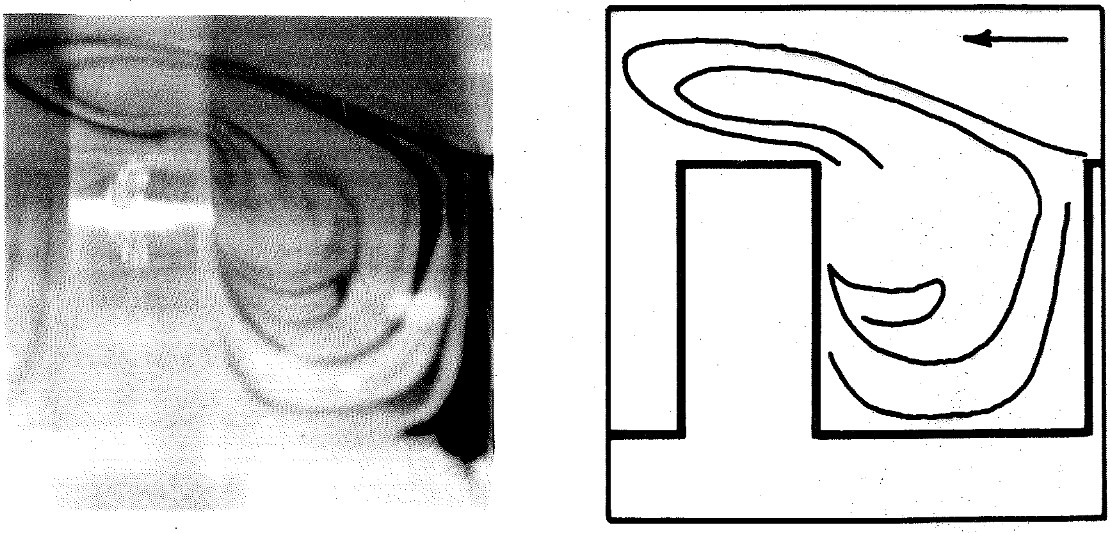

Fig. 51. Cavity flow mode indeterminant between a strong and weak exchange flow mode, $\epsilon^* = 22.7$, 1/4 × 1/4 in. cavity, $U_\infty = 0.245$ ft/sec.

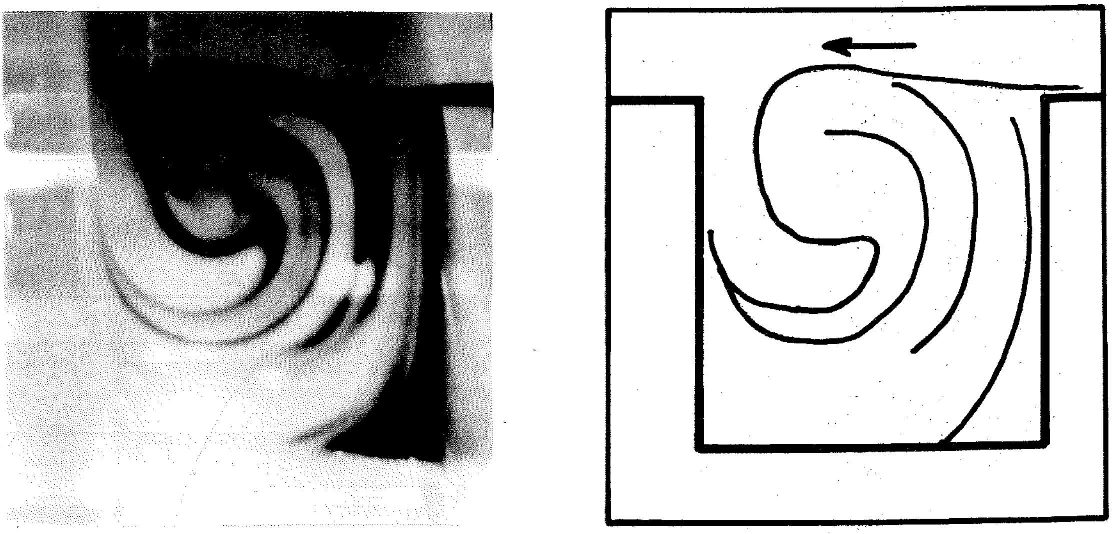

Fig. 52. Cavity inflow flow mode at $\epsilon^* = 22.7$, 1/4 × 1/4 in. cavity, $U_\infty = 0.245$ ft/sec.

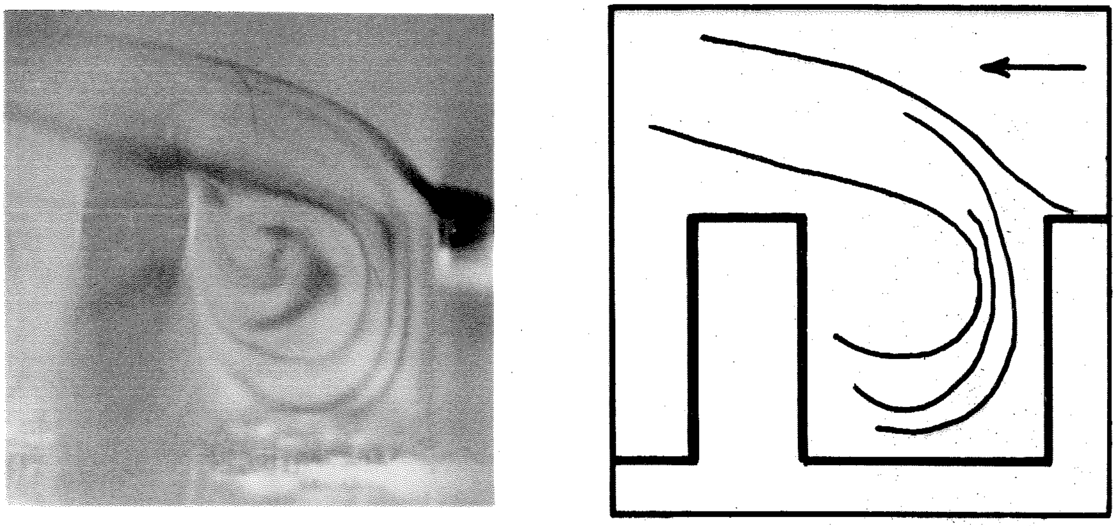

Fig. 53. Cavity strong exchange flow mode at $\epsilon^* = 24.3$, 1/8 × 1/8 in. cavity, $U_\infty = 0.510$.

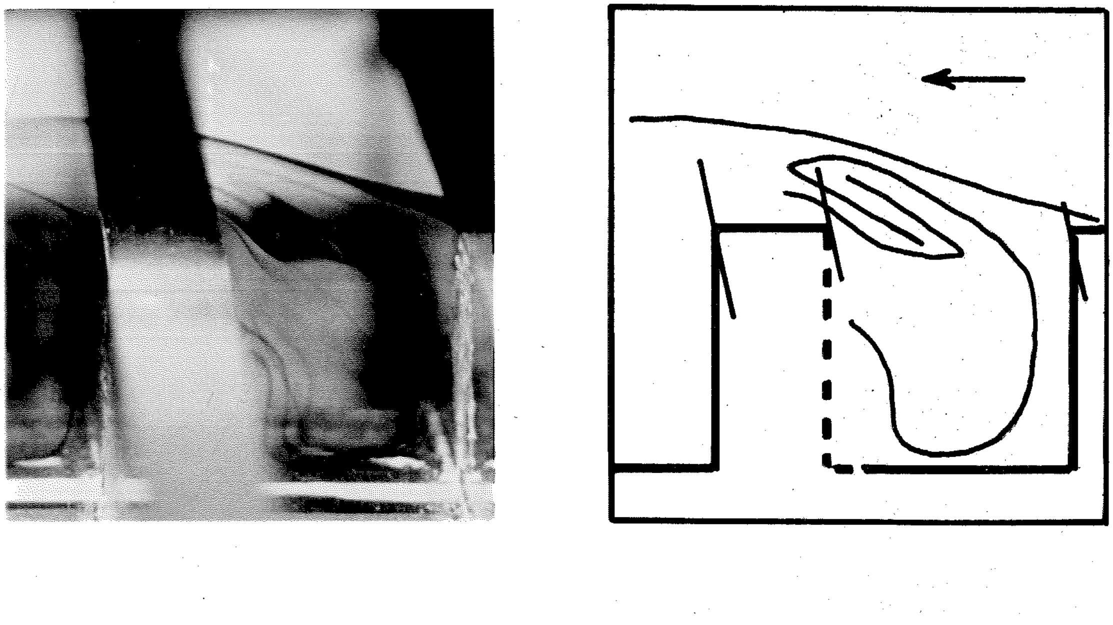

Fig. 54. Cavity weak exchange flow mode at $\epsilon^* = 25.6$, 1/2 × 1/2 in. cavity, $U_\infty = 0.123$ ft/sec.

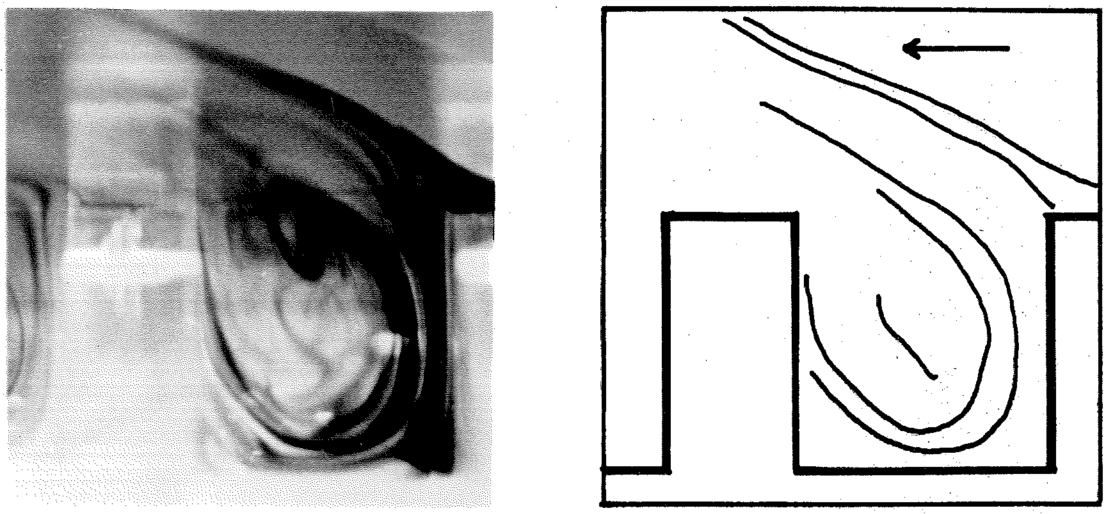

Fig. 55. Cavity strong exchange flow mode at $\epsilon^* = 49.3$, 1/4 × 1/4 in. cavity, $U_\infty = 0.520$ ft/sec.

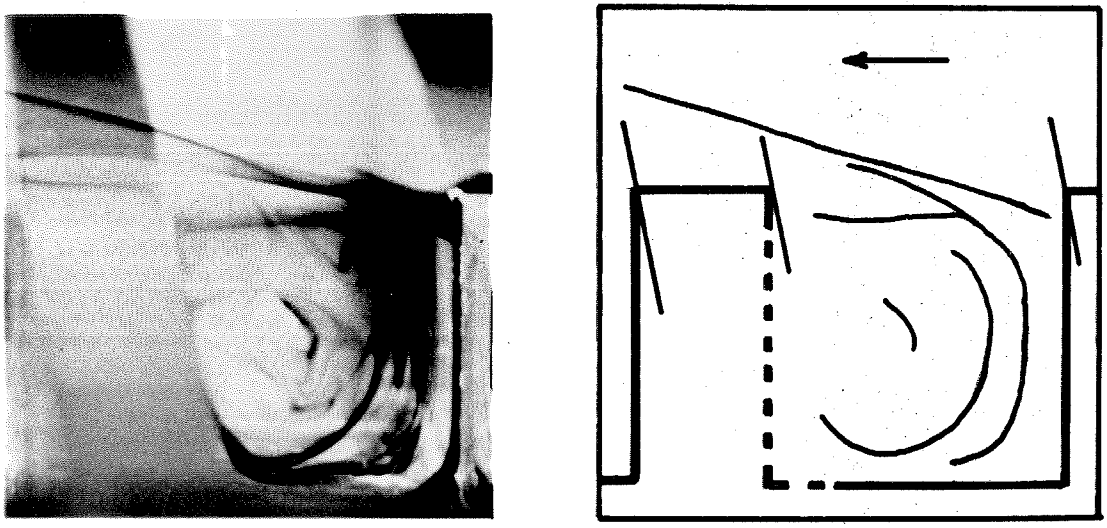

Fig. 56. Cavity weak exchange flow mode at $\epsilon^* = 46.6$, 1/2 × 1/2 in. cavity, $U_\infty = 0.252$ ft/sec.

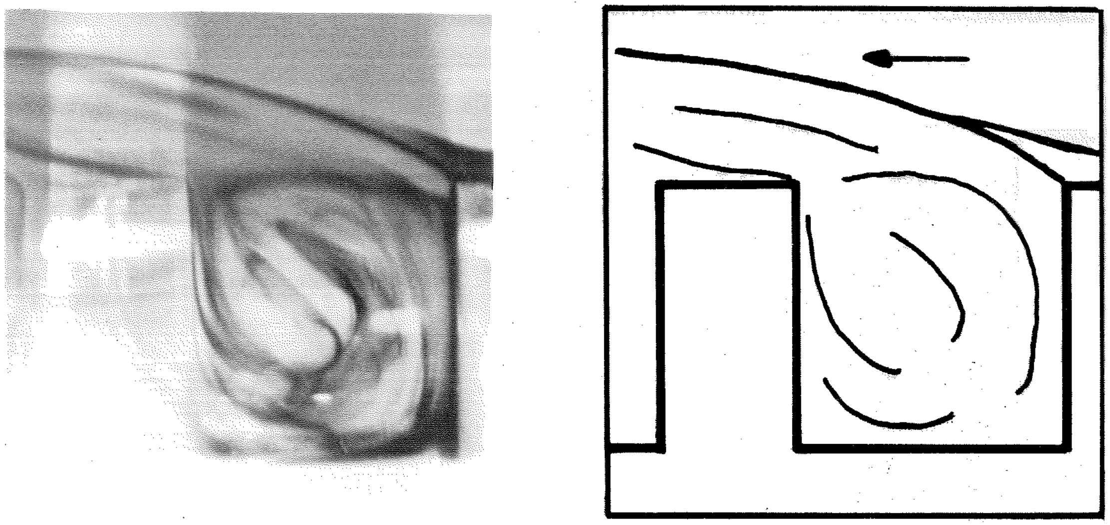

Fig. 57. Cavity weak exchange flow mode at $\epsilon^* = 49.3$, 1/4 × 1/4 In. cavity, $U_\infty = 0.520$ ft/sec.

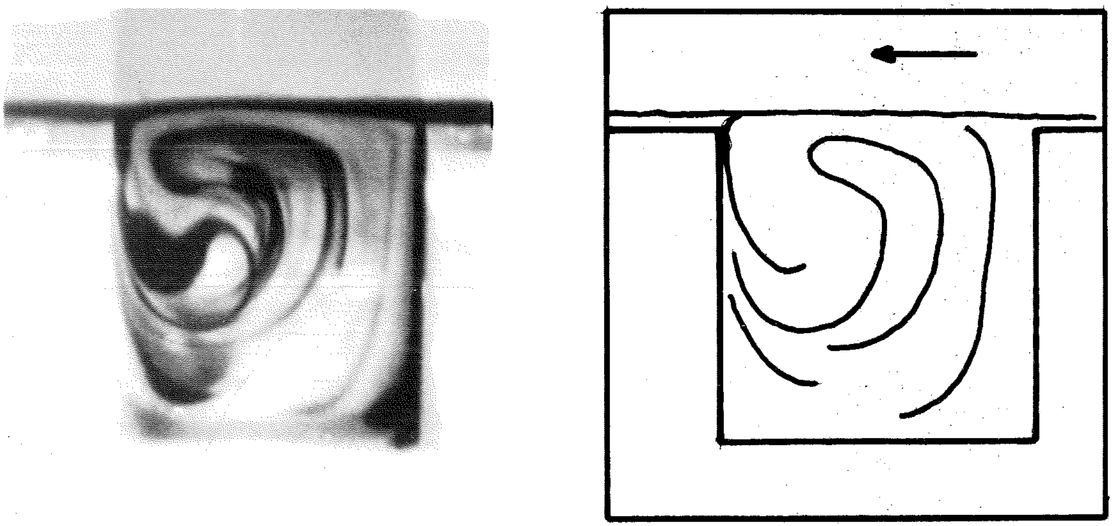

Fig. 58. Cavity divide flow mode at $\epsilon^* = 49.3$, 1/4 × 1/4 in. cavity, $U_\infty = 0.520$ ft/sec.

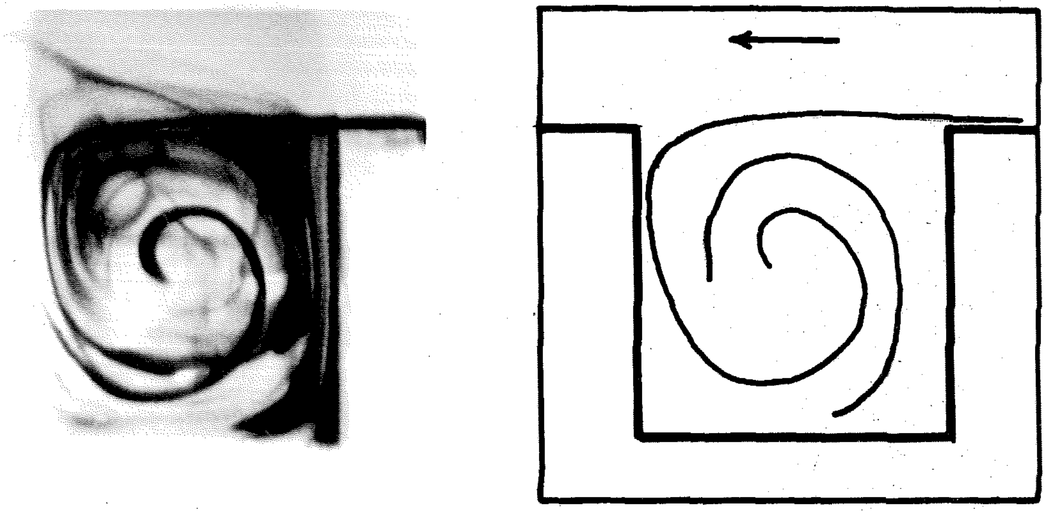

Fig. 59. Cavity inflow flow mode at $\epsilon^* = 49.3$, 1/4 × 1/4 in. cavity, $U_\infty = 0.520$ ft/sec.

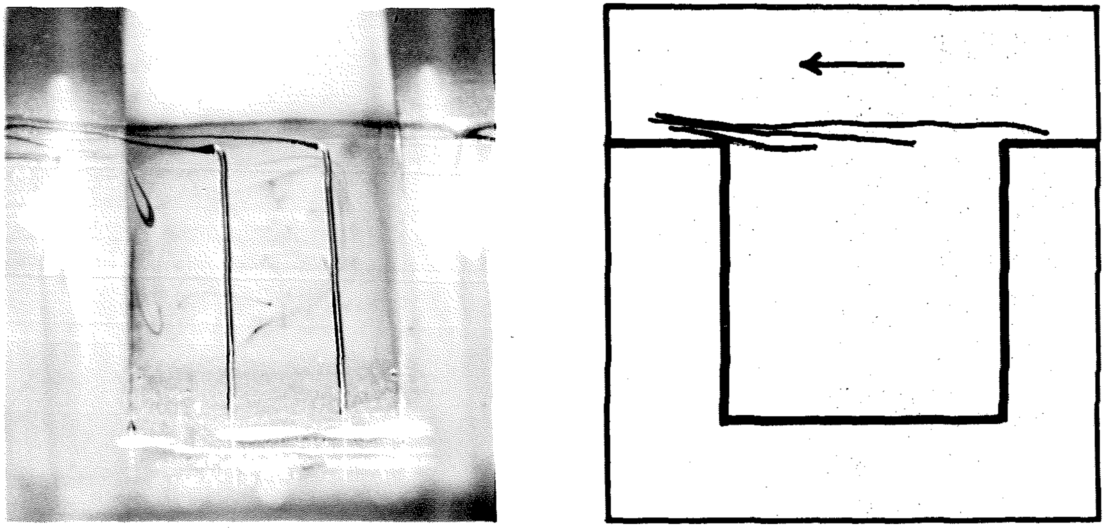

Fig. 60. Cavity divide flow mode at $\epsilon^* = 50.4$, 1 × 1 in. cavity, $U_\infty = 0.121$ ft/sec. Vertical tubes are 0.025 ins. dia. and are for admitting dye.

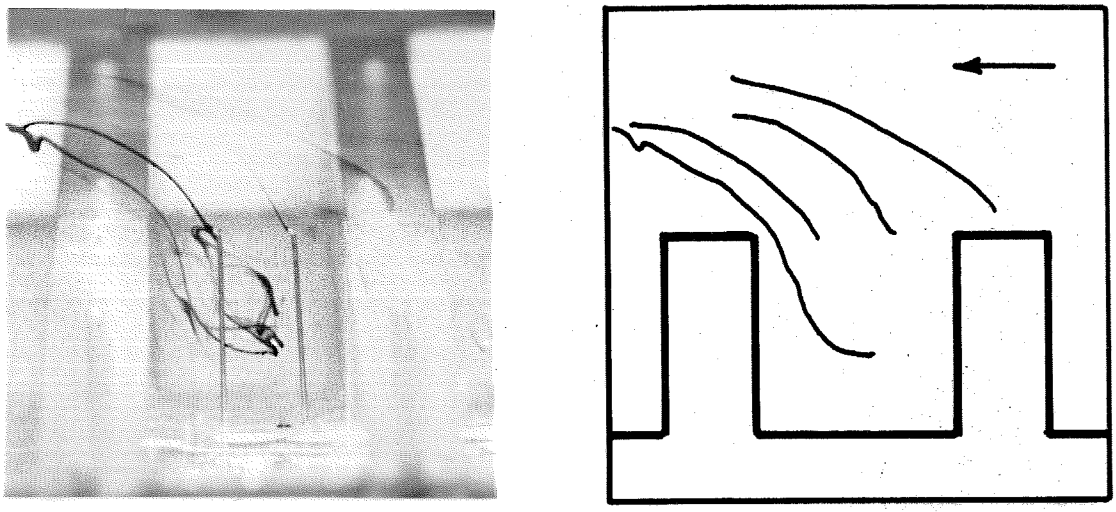

Fig. 61. Cavity strong exchange flow mode at $\epsilon^* = 50.4$, 1 × 1 in. cavity, $U_\infty = 0.121$ ft/sec.

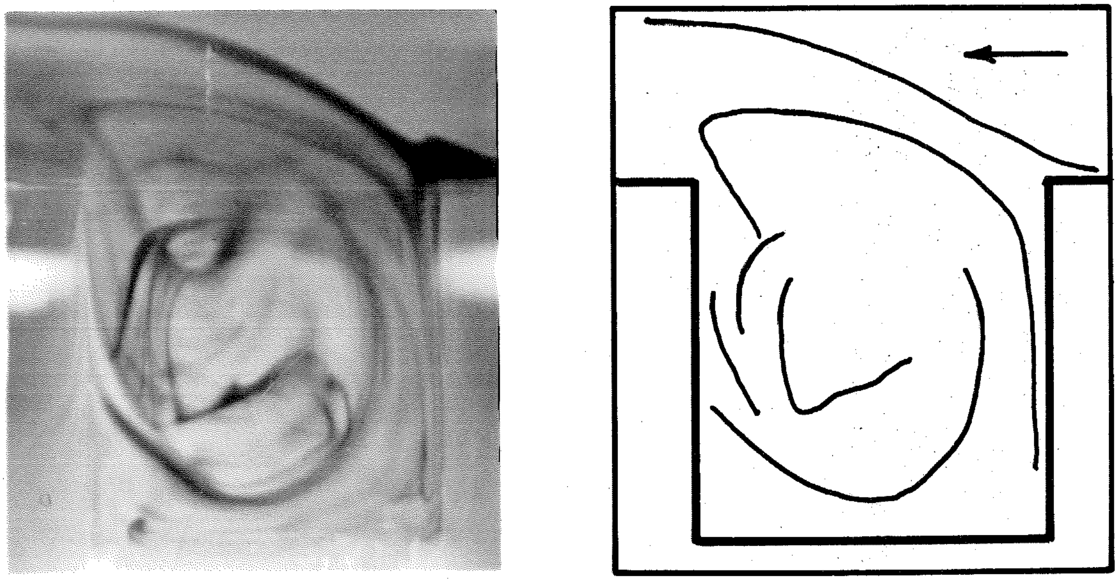

Fig. 62. Cavity strong exchange flow mode at $\epsilon^* = 68.5$, 1/4 × 1/4 in. cavity, $U_\infty = 0.835$ ft/sec.

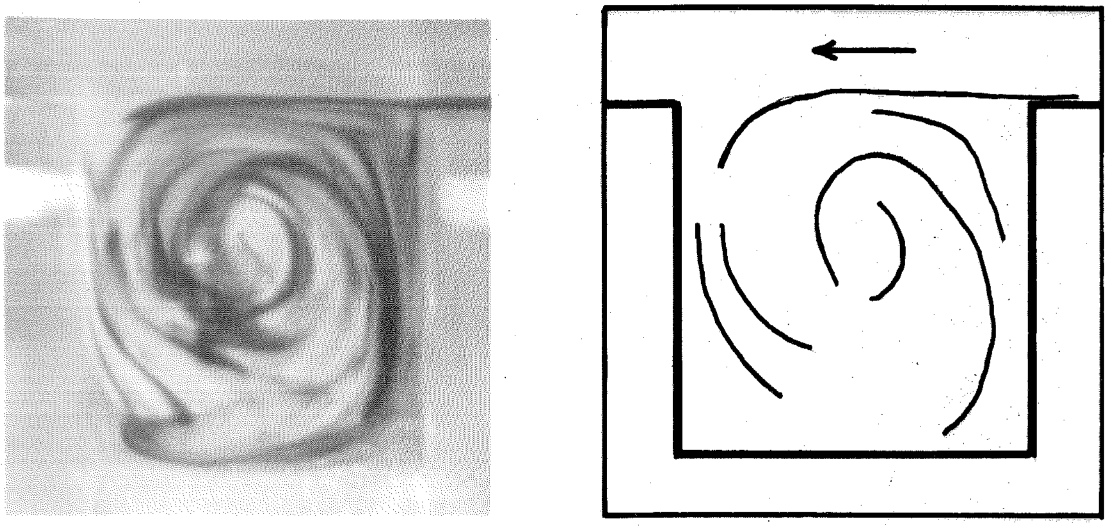

Fig. 63. Cavity inflow flow mode at $\varepsilon^* = 68.5$, 1/4 × 1/4 in. cavity, $U_\infty = 0.835$ ft/sec.

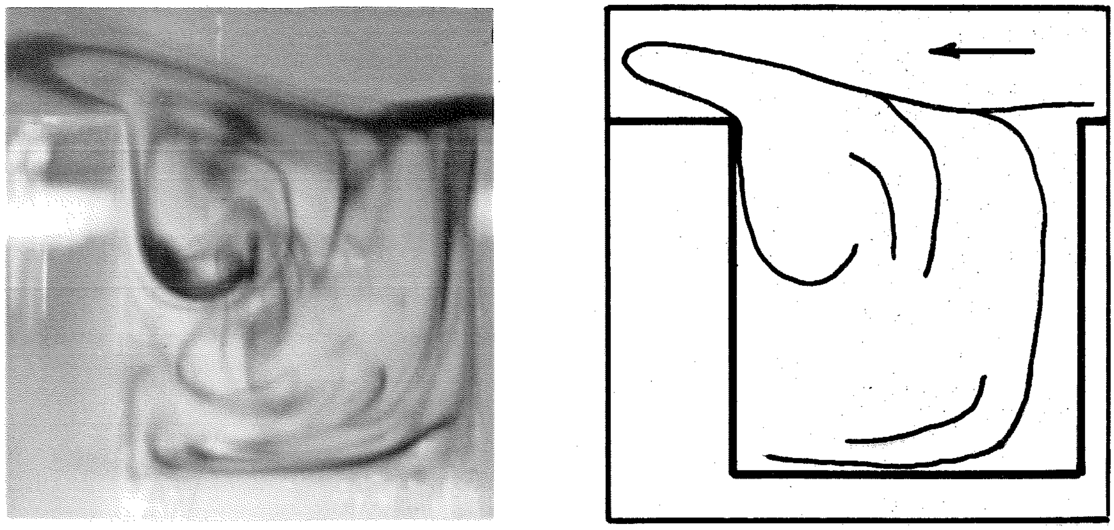

Fig. 64. Cavity weak exchange flow mode at $\varepsilon^* = 68.5$, 1/4 × 1/4 in. cavity, $U_\infty = 0.835$ ft/sec.

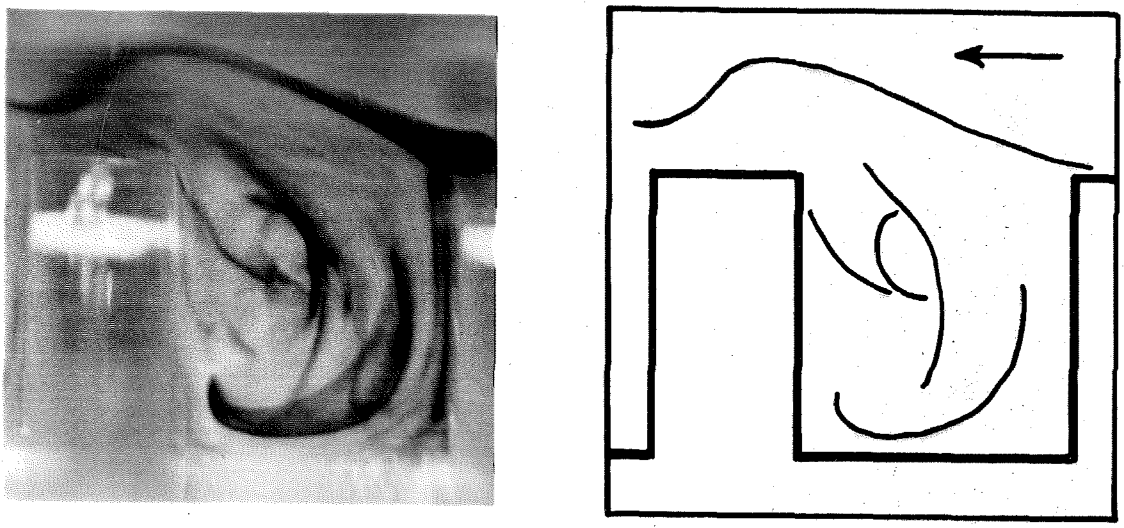

Fig. 65. Cavity flow mode indeterminant between a weak and strong exchange flow mode at $\epsilon^* = 68.5$, 1/4 × 1/4 in. cavity, $U_\infty = 0.835$ ft/sec.

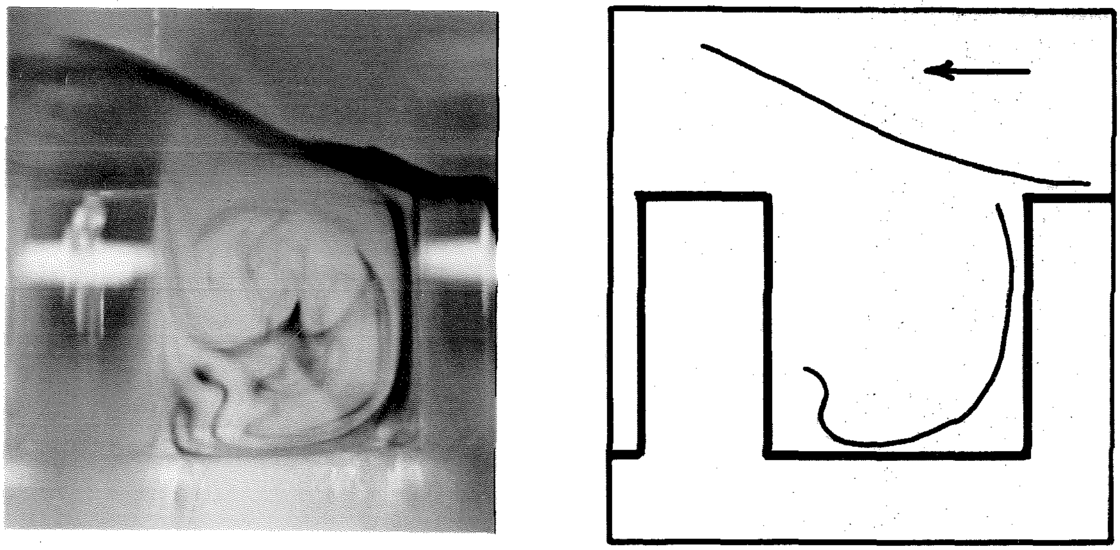

Fig. 66. Cavity flow mode indeterminant between a weak and strong exchange flow mode at $\epsilon^* = 68.5$, 1/4 × 1/4 in. cavity, $U_\infty = 0.835$ ft/sec.

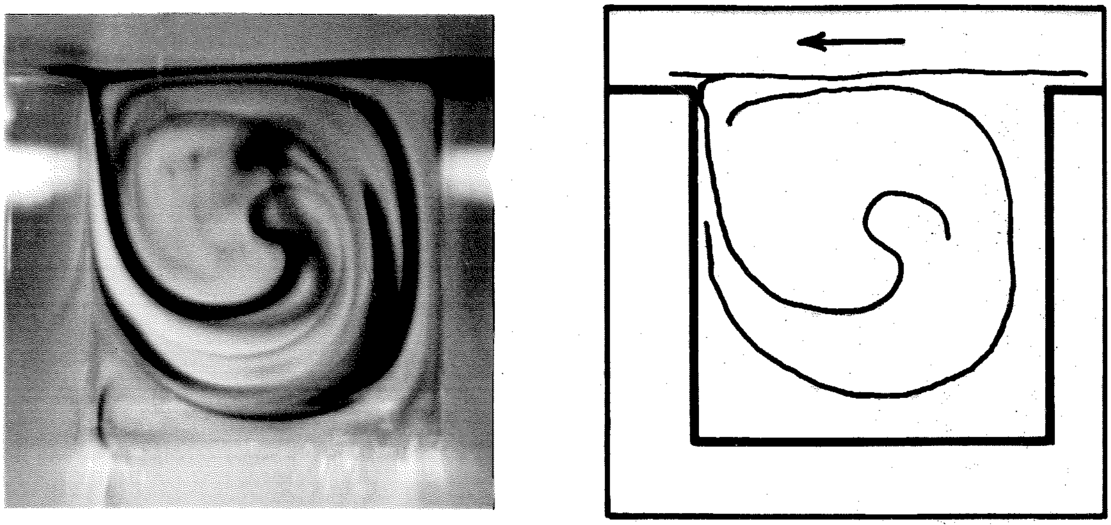

Fig. 67. Cavity divide flow mode at $\epsilon^* = 68.5$, 1/4 × 1/4 in. cavity, $U_\infty = 0.835$ ft/sec.

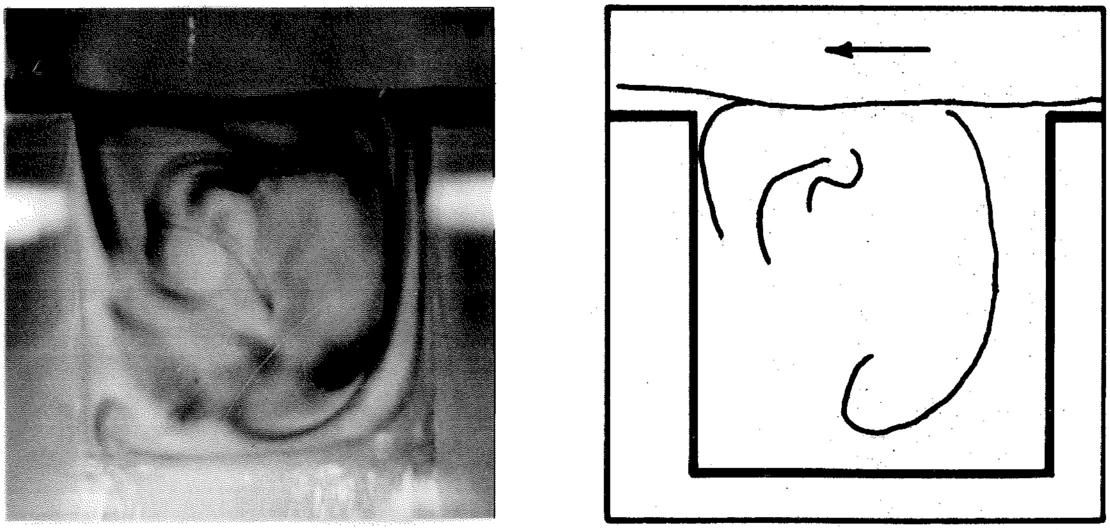

Fig. 68. Cavity divide flow mode at $\epsilon^* = 68.5$, 1/4 × 1/4 in. cavity, $U_\infty = 0.835$ ft/sec.

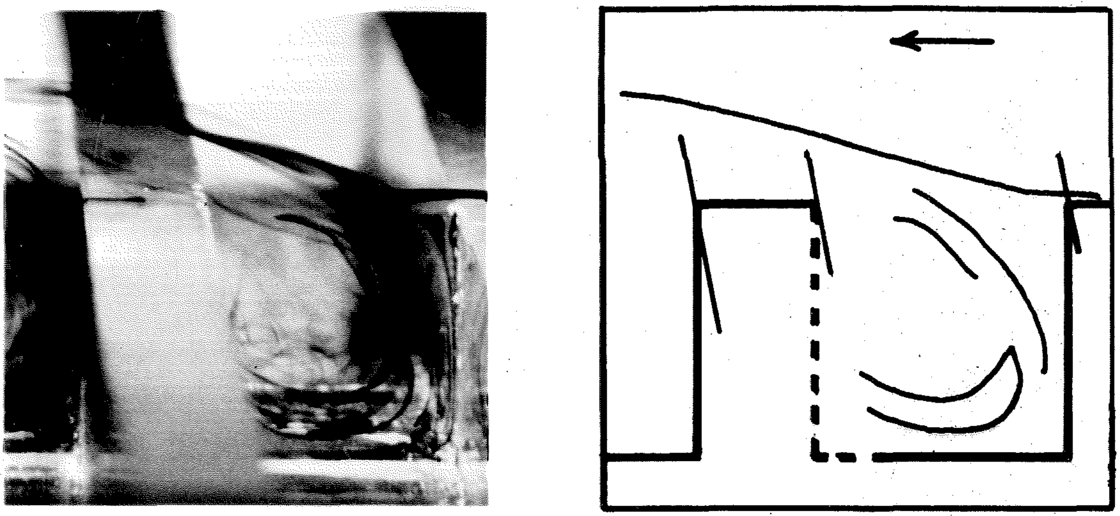

Fig. 69. Cavity weak exchange flow mode at $\varepsilon^* = 96.6$, 1/2 × 1/2 in. cavity, $U_\infty = 0.510$ ft/sec.

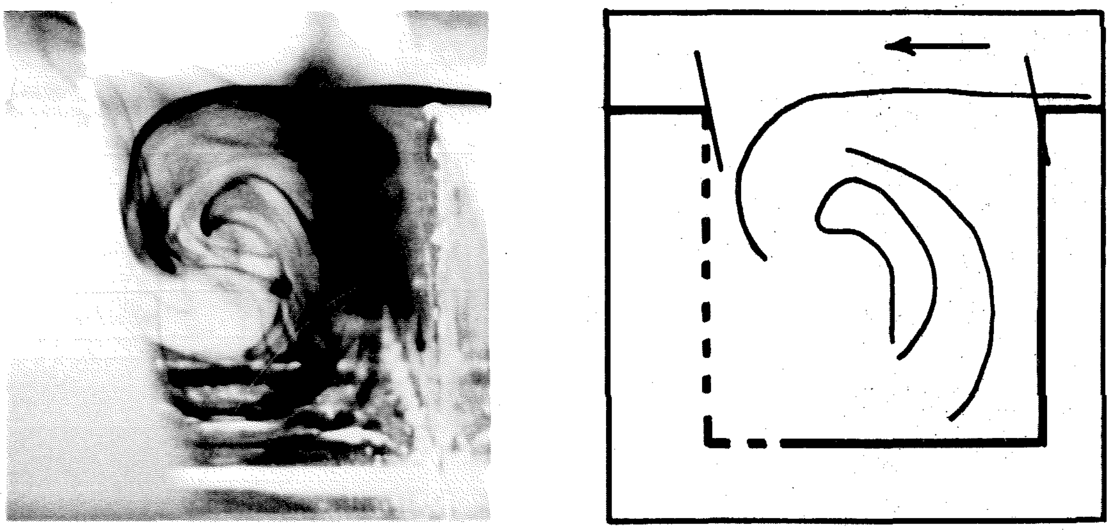

Fig. 70. Cavity inflow flow mode at $\varepsilon^* = 96.6$, 1/2 × 1/2 in. cavity, $U_\infty = 0.510$ ft/sec.

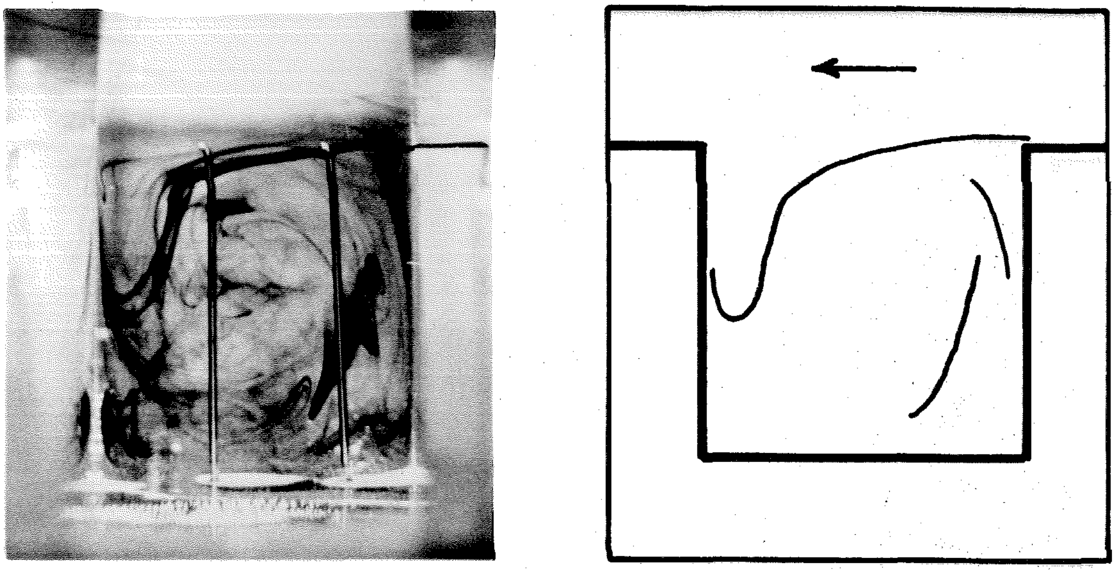

Fig. 71. Cavity inflow flow mode at $\epsilon^* = 95.8$, 1 × 1 in. cavity, $U_\infty = 0.262$ ft/sec. Vertical tubes are 0.025 ins. dia. and are for admitting dye.

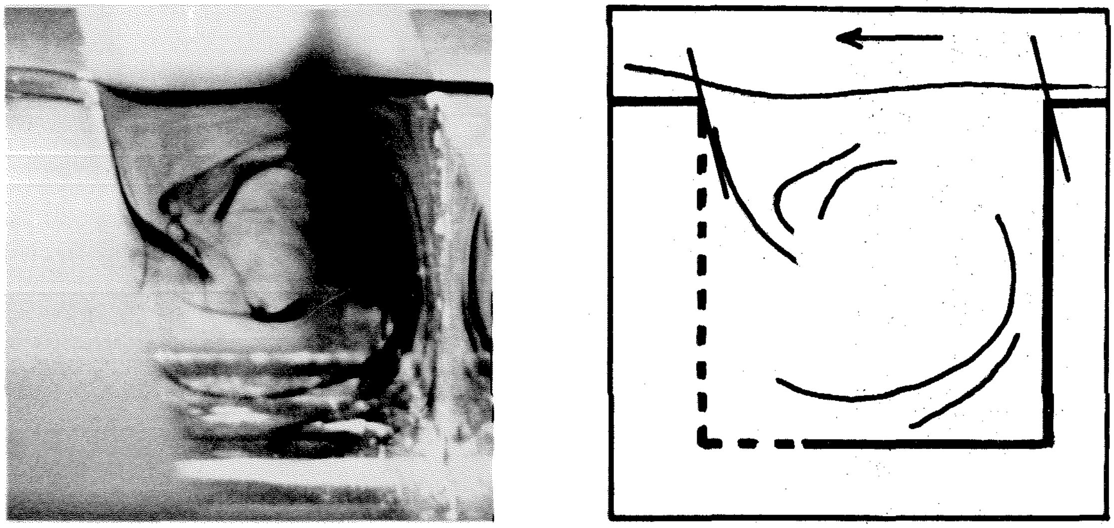

Fig. 72. Cavity divide flow mode of $\epsilon^* = 96.6$, 1/2 × 1/2 in. cavity, $U_\infty = 0.510$ ft/sec.

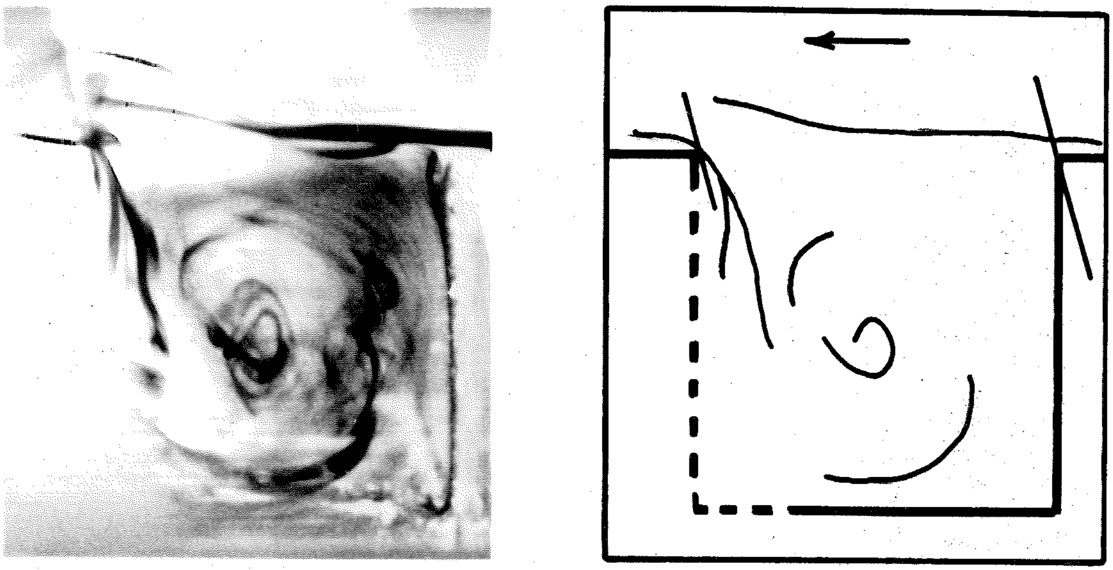

Fig. 73. Cavity weak exchange flow mode at $\epsilon^* = 126$, 1/2 × 1/2 in. cavity, $U_\infty = 0.768$ ft/sec.

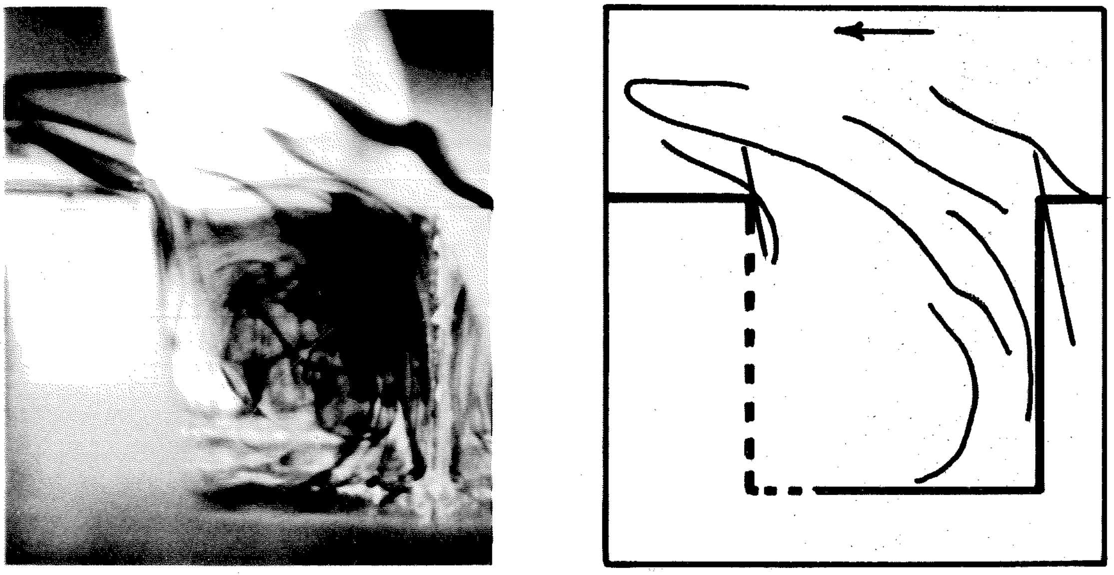

Fig. 74. Cavity strong exchange flow mode at $\epsilon^* = 126$, 1/2 × 1/2 in. cavity, $U_\infty = 0.768$ ft/sec.

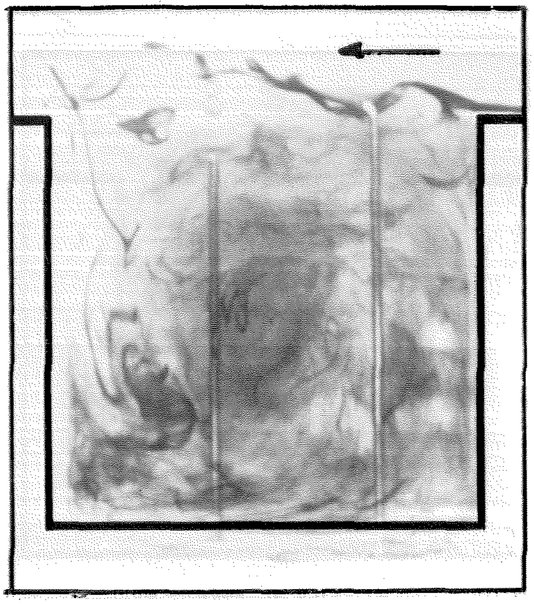

Fig. 75. Cavity vortex flow mode at $\epsilon^* = 201$, 1×1 in. cavity, $U_\infty = 0.529$ ft/sec.

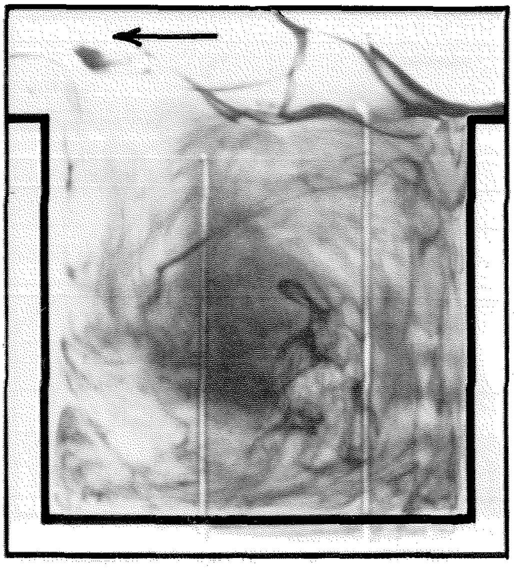

Fig. 76. Cavity vortex flow mode at $\epsilon^* = 201$, 1×1 in. cavity, $U_\infty = 0.259$ ft/sec.

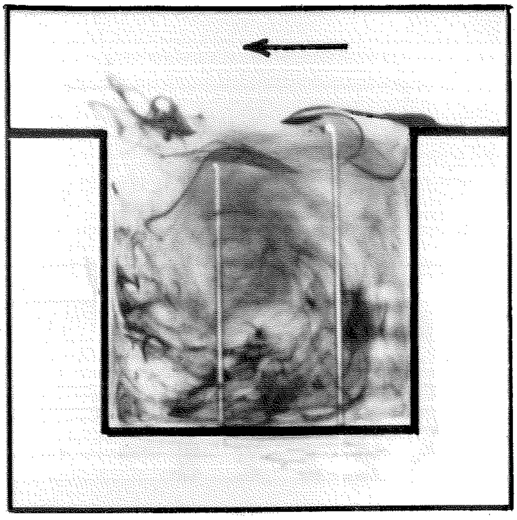

Fig. 77. Cavity vortex flow mode at $\epsilon^* = 259$, 1 × 1 in. cavity, $U_\infty = 0.788$ ft/sec.

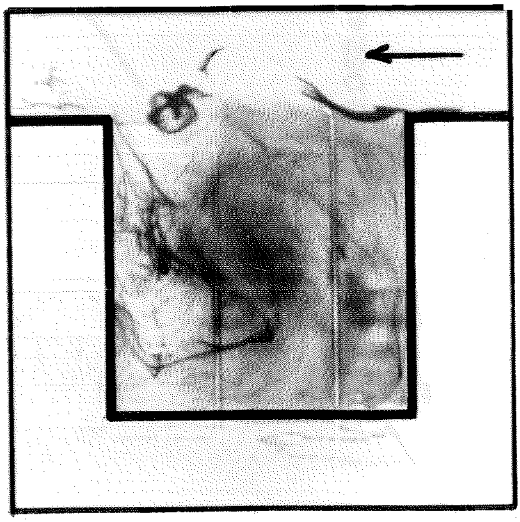

Fig. 78. Cavity vortex flow mode at $\epsilon^* = 259$, 1 × 1 in. cavity, $U_\infty = 0.788$ ft/sec.

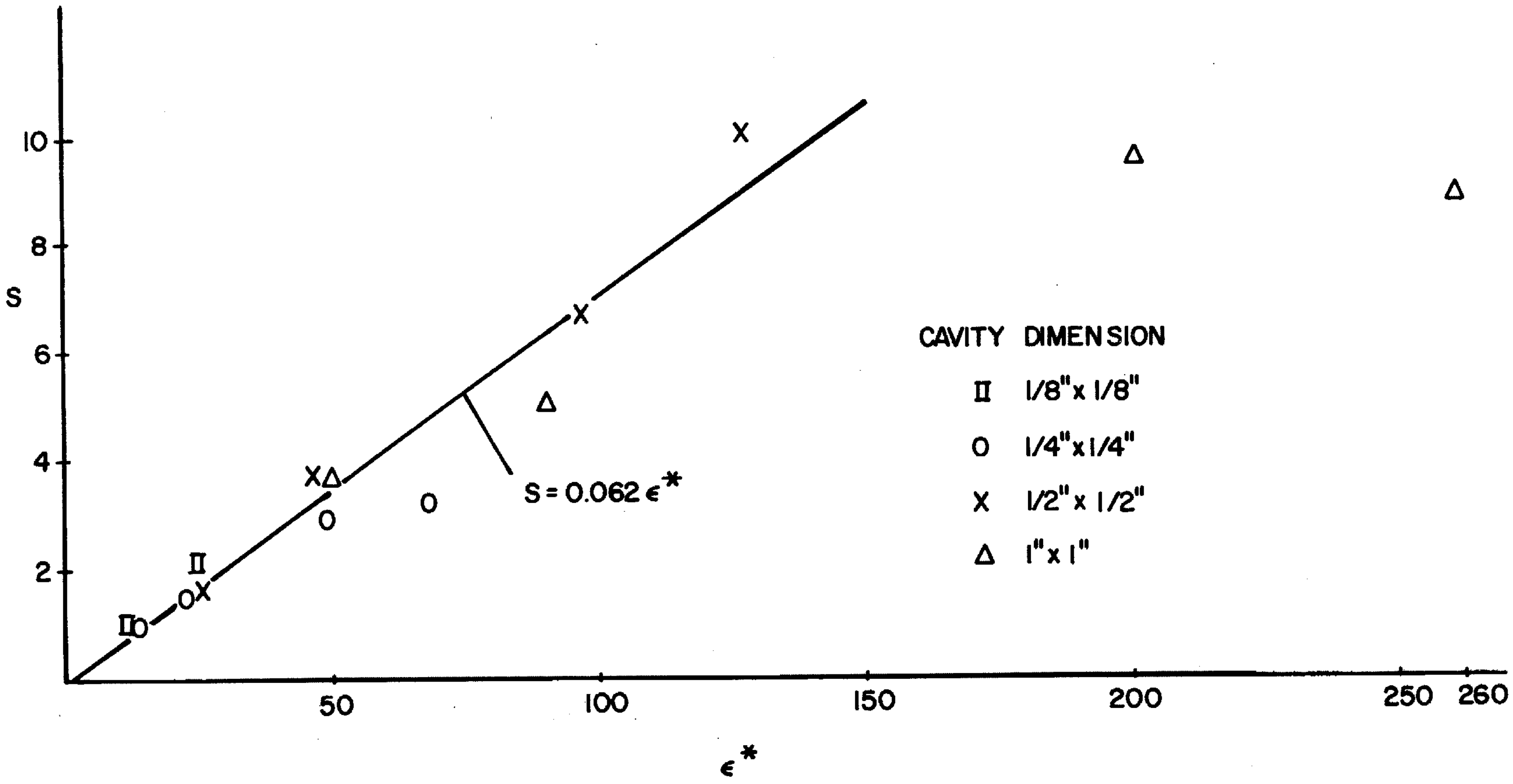

Fig. 79. The cavity Strouhal number, s vs. ϵ^*.

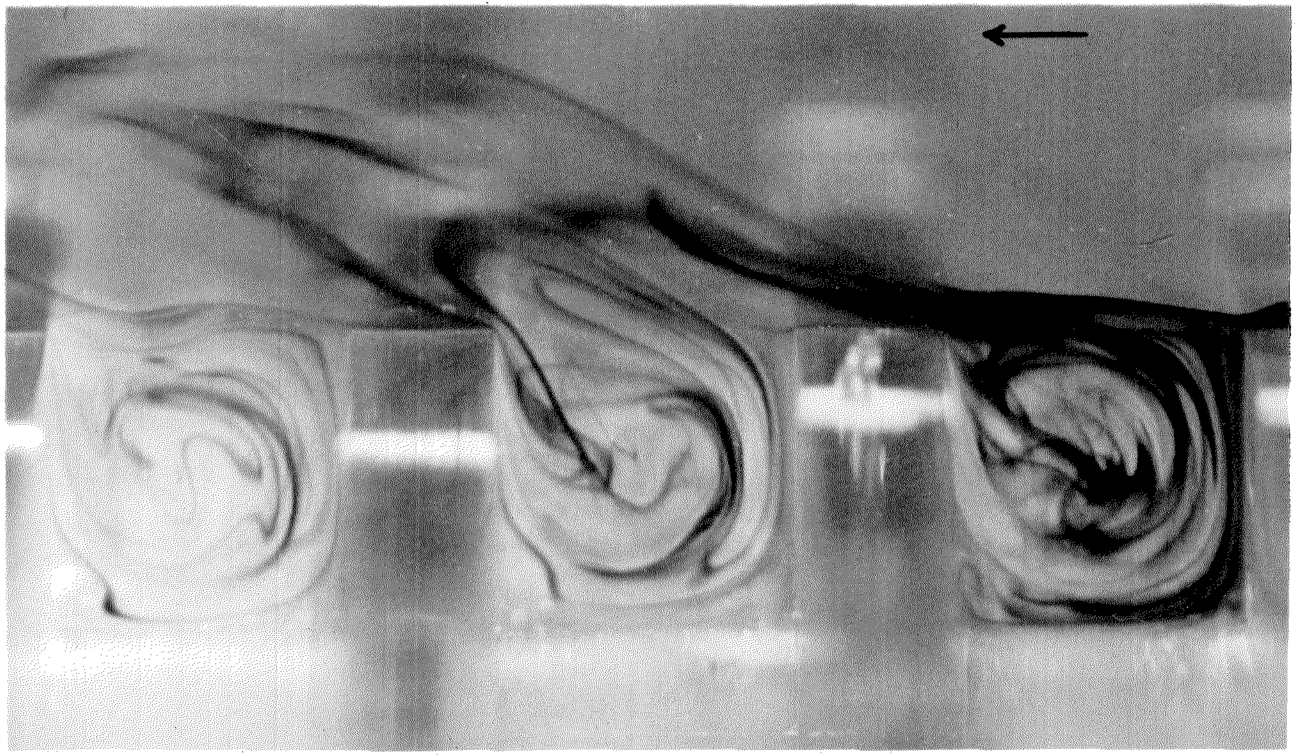

Fig. 80. A strong exchange flow mode shown moving down stream. The 4th, 5th and 6th cavities of a series. 1/4 × 1/4 in. cavities, $\epsilon^* = 68.5$, $U_\infty = 0.835$ ft/sec.